Title
Active Augmentation of Condensation: Focus on Jet Impingement Technique

Author
Alshehri, Ali Mohammad A

Publication Date
2021

Peer reviewed|Thesis/dissertation

UNIVERSITY OF CALIFORNIA

Los Angeles

Active Augmentation of Condensation: Focus on Jet Impingement Technique

A dissertation submitted in partial satisfaction
of the requirements for the degree
Doctor of Philosophy in Mechanical Engineering

by

Ali Mohammad A Alshehri

2021

ABSTRACT OF THE DISSERTATION

Active Augmentation of Condensation: Focus on Jet Impingement Technique

by

Ali Mohammad A Alshehri
Doctor of Philosophy in Mechanical Engineering
University of California, Los Angeles, 2021
Professor Hossein Pirouz Kavehpour, Chair

Condensation is a very complicated subject to fully unveil as it constitutes a complex interplay of momentum, heat and species transport and interfacial physics. Drop-wise condensation (DWC) adds more layers of complexity by introducing droplet dynamics and the two-way interaction with droplets surrounding. DWC has been shown repeatedly for about a century to possess around an order of magnitude improved heat transfer rates. Additionally, it has been shown that DWC is limited by the maximum size of droplets a surface sustains. Since this realization, promoting DWC has been greatly steered towards developing stable hydrophobic coating techniques. However, attempts have not been feasible so far especially due to the extreme conditions encountered in condensation processes. Another concern that has not been resolved adequately is the deterioration of heat and condensation rates due to the presence of non-condensable gases (NCG). This

dissertation aims at understanding the process of condensation especially in the presence of NCG.

First, a numerical model of the process of vapor condensation on surfaces characterized by film-wise condensation with the presence of (NCG) is presented. State variables in both the condensate film and the diffusion layer were solved separately and the condensation interface was used to couple the two solutions. The solution of the condensate film was obtained using well-established solutions of laminar film condensation of pure vapor. In contrast to other models surveyed, this work provides a inexpensive and accurate predictions of heat and mass transfer characteristics. We validated the work against two classical condensation problems. The model was first validated against empirical correlations and experimental work, resulting in a very good agreement. We then assessed the applicability of ignoring the condensate film effect, as performed in previous models, on the condensation processes by observing the thermal resistances of both the condensate film and diffusion layer. Results indicated that for the studied cases of NCG mass fractions above 20%, the condensate thermal resistance was at least an order of magnitude lower than that of the diffusion layer. However, the two thermal resistances seem to approach each other as NCG mass fraction becomes smaller. On another front, we observed that models that ignore the condensate film thermal resistance underestimate the interfacial temperature albeit accurately predicting the overall heat transfer rate. To simulate even lower NCG mass fractions, we validated our model to the classical analytical work of Sparrow and co-workers. Results showed an excellent agreement between the two solutions at different NCG mass

fractions (0.5%-10%) and subcooling degrees (5^oF-40^oF). Finally, we found a good agreement between results of our model and the heat/mass transfer analogy. The heat/mass transfer analogy is a semi-empirical method therefore, is limited to the existing correlations and their uncertainties. On the other hand, our model does not use any empiricism and relies on the available solutions of laminar condensate film of pure vapor in predicting the liquid side heat transfer coefficient.

Moreover, motivated by the improvement in heat transfer by frequently disturbing the thermal boundary layer in nucleate boiling phenomenon, we attempted making the analogy to DWC. We developed an initial theoretical model to predict the transience of the diffusion boundary layer in condensation problems with NCG presence. The problem of suddenly exposing a cooled surface to a humid environment was modeled as two semi-infinite gas and solid domains in contact with the condensate film as a coupling condition. Results showed that the transient behavior of heat and condensation rates start by very high values and then decrease to steady state rates. This suggested that if the diffusion layer is frequently disturbed by droplets of heights similar to the layer's thickness, the condensation rate is expected to improve. To realize this, jet impingement of humidified air was proposed as a means of thinning the diffusion layer as well as to provide better shedding capabilities of condensate droplets.

Finally, Utilizing jet impingement technique as a means for continuous drop-wise condensation (CDC) was investigated. The technique showed an advantage of overcoming the necessity of using highly non-wetting surfaces while yet maintaining micron-sized droplets. By shifting focus from sur-

face treatment to the force required to sweep off a droplet, we were able to utilize stagnation pressure of jet impingement to tune the shed droplet size. To demonstrate the effectiveness of this technique, we performed condensation experiments on a broad range of contact angle and contact angle hysteresis surfaces. The results showed that droplet size being shed can be tuned effectively by tuning the jet parameters namely the jet Reynolds number. Droplets as low as 20 μm in radius on a hydrophilic surface were shed with this technique surpassing the traditional gravity-assisted shedding mechanism by almost 80 folds. In terms of condensation rate improvement, we showed theoretically that CDC improves the condensation rate of pure steam, and hence heat transfer rate, by more than 300% compared to gravity-assisted shedding DWC. Finally, our experimental observations showed that the effect of NCG, such as air in this work, is greatly alleviated by utilizing our technique. An improvement by at least six folds in mass transfer compactness factor compared to state-of-the-art dehumidification technology was possible. We illustrated the physics of droplet departure and mobility due to the stagnation flow condition by microscopically tracing a single droplet.

The dissertation of Ali Mohammad A Alshehri is approved.

Adrienne S. Lavine

Jeffrey D. Eldredge

Timothy S. Fisher

Hossein Pirouz Kavehpour, Committee Chair

University of California, Los Angeles

2021

This thesis is dedicated:

to my parents, who have always supported me in my academic endeavors.

to my sisters and brothers, for their love and moral support.

to my soulmate, Asma, whose encouragement

over the many years have been

invaluable.

to Sara and Yosef

TABLE OF CONTENTS

LIST OF SYMBOLS

a_v	constant associated with the Gaussian distribution of the jet velocity
a_ω	constant associated with the Gaussian distribution of the jet concentration
C_{1-4}	constants that are independent of jet velocity and standoff distance
C_p	Specific heat capacity, J/(kg· K)
D	Tube diameter, m
D_{ij}	Binary diffusion coefficient, m^2/s
E	Total specific energy, J/kg
g	Gravitational acceleration, m/s^2
h	Specific enthalpy, J/kg
H	Standoff distance between tube exit and condensation surface, m
$\overline{h}$	Average convective heat transfer coefficient, $W/(m^2 \cdot K)$
h_{fg}	Latent heat of vaporization J/kg
k	Thermal conductivity, W/(m· K)
L	length, m
M	Molecular weight, kg/mol
$\overline{Nu}$	Average Nusselt number
P	Pressure, Pa
Q	Volumetric flow rate, m^3/s
q''	Heat transfer flux, W/m^2

R_{th}	Thermal resistance defined as $1/\overline{h}$
Re	Reynolds number
RH	Relative humidity
r	Radial direction in polar coordinate system
t	time, s
T	Temperature , ^{o}C
ΔT	Subcooling degree defined as $T_\infty - T_s$, K*
U	Overall heat transfer coefficient defined as q/ΔT, W/(m$^2 \cdot K$)
v	velocity, m/s
$\overrightarrow{v}$	Velocity vector $< v_x, v_y, v_z >$, m/s
x and y	Tangent and normal directions from the condensation surface
z	Axial direction in polar coordinate system

Greek symbols

ν	Kinematic viscosity, m^2/s
μ	Dynamic viscosity, Pa$\cdot s$
ρ	Density, kg/m^3
$\overline{\overline{\tau}}$	Shear stress tensor, Pa
ω	Species mass fraction defined as the ratio between the density of a certain species to the total density at a prescribed state
ϕ	Suction factor
δ	Thickness of the boundary layer in the wall jet region, m

Superscripts and subscripts

a	Property related to air
g	Property related to vapor-gas mixture
l	Property related to the condensate liquid

L	Evaluated at the total length of the condenser wall
N	Evaluated using Nusselt Analysis for pure vapor
o	Evaluated at the condensation interface
ref	A reference value
sat	Evaluated at a saturation state
BF	Related to the diameter of the Breath Figure spot
j	Property related to the jet at the tube exit condition
max	Property related to the maximum value in a velocity concentration distribution, usually located at the center (r=0)
o	Related to the characteristic velocity
r	Property related to the recovery concentration which is defined as the concentration on the wall where no condensation is present
s	Property related to condensation surface condition
v	Property related to the water vapor
∞	Evaluated at the ambient conditions

LIST OF FIGURES

LIST OF TABLES

ACKNOWLEDGMENT

My sincere and deepest gratitude to the following persons without whom this work would not have been completed with success.

Thank you **Professor Pirouz Kavehpour** for your support, guidance and encouragement throughout the duration of my doctoral work. Thank you for allowing me to think freely and sharing your knowledge and directions with me along the way. It has been fun and intriguing to work with you.

Thank you **Professor Jonathan Rothstein** for the numerous zoom meetings and thoughtful discussions. I enjoyed interchanging ideas, criticizing them and decisively rejecting bad ones.

Thank you **Professors Adrienne Lavine, Jeff Eldredge, and Timothy Fisher** for serving on my PhD committee. During my course work, you opened my eyes to the beauty of Heat transfer, Fluid mechanics, Microscopic energy transport, and Phase change physics.

I would like to thank my lab mates **Aysan Rangchian, Elaheh Alizadeh-Birjandi, Ryan McGuan, Sahar Andalib and Shima A Sarabi** for making my work environment a friendly one. You are some of the great minds I met during my stay at UCLA, I wish you a great future ahead. My gratitude extends to my friends for making Los Angeles times fun and a home away from home.

My deepest gratitude and appreciation to my family for their continuous

support. I am grateful to my father, mother, sisters and brothers for always remembering me and supporting me throughout my higher education journey. I am forever indebted to my soulmate, Asma, for being here for me and handling my ups and downs. My little honeybuns Sara and Yosef, this work is dedicated to you.

Lastly, I thank King Fahd University of Petroleum and Minerals for sponsoring my PhD education. The support of NSF (Project number CBET-2032533) and NIH (Project number xxx) are acknowledged.

CURRICULUM VITAE

2009 – 2014	B.S. in Mechanical Engineering, King Fahd University of Petroleum and Minerals (KFUPM), Dhahran, Saudi Arabia.
2015 – 2017	M.S. in Mechanical Engineering, King Fahd University of Petroleum and Minerals (KFUPM), Dhahran, Saudi Arabia.

PUBLICATIONS AND PRESENTATIONS

[1] Alizadeh-Birjandi, E., **Alshehri, A.**, Kavehpour, H. P. (2019). Condensation on Surfaces with Biphilic Topography: Experiment and Modeling. Frontiers in Mechanical Engineering, 5, 38.

[2] Andalib, S., **Alshehri, A.**, Kavehpour, P. (2019). Combined effect of relative humidity and substrate temperature on evaporation of methanol droplet. Journal of Coatings Technology and Research, 16(6), 1691-1698.

[3] **Alshehri, A.**, Andalib, S., Kavehpour, H. P. (2020). Numerical modeling of vapor condensation over a wide range of non-condensable gas concentrations. International Journal of Heat and Mass Transfer, 151, 119405.

[4] **Alshehri, A.** Kavehpour, H. P. (2021). Breath Figure Spot: A Recovery Concentration Manifestation. International Journal of Heat and Mass Transfer, 172, 121166.

[5] **Alshehri, A.**, Rothstein, J. P. Kavehpour, H. P. (2021). A Novel Continuous Drop-Wise Condensation Technology for Improved Heat and Mass Transfer Efficiencies. arXiv:2103.13077v1 [physics.flu-dyn]

[6] **Alshehri, A.** Kavehpour, H. P. (2020) "Low-cost and fast sample collection system for viral load level diagnosis: point-of-care and environmental detection." U.S. Provisional Application No. 63/010,453

[7] **Alshehri, A.** Kavehpour, H. P., Annabi N., Candler R., Rothstein J.P., Ruberti J. (2020) "Non-invasive exhaled breath (EB) collection apparatus" U.S. Provisional Application No. 63/030,767

[8] Andalib, S., **Alshehri A.**, and Kavehpour H. P. (2018). Experimental Study of Substrate Temperature Effect on the Behavior of Droplet Evaporation of Binary Mixtures. APS Division of Fluid Dynamics Meeting

[9] Andalib, S., **Alshehri A.**, and Kavehpour H. P. (2019). Effect of a second component in organic droplet evaporation: initially present versus absorbed during the process. APS Division of Fluid Dynamics Meeting

CHAPTER 1

Introduction

1.1 Background

1.1.1 Condensation: classifications and heat/mass transfer mechanisms

Phase transition, in general, takes place through several processes which can be classified as homogeneous and heterogeneous phase change processes [1]. In the following sections, the different classes of condensation are discussed with more focus to heat and mass transfer mechanisms of each class.

Class I: Homogeneous condensation

Homogeneous condensation is defined as a phase change process from vapor into liquid that takes place away from non-vapor interfaces. Usually, it requires a tremendous amount of subcooling degree [2], which can be achieved by isobarically dropping the environmental temperature below the saturation point. Alternatively, homogeneous condensation can be obtained by isothermally increasing the system pressure. The principle mechanism behind this class of condensation is that as vapor molecules spacing becomes smaller, a cluster of molecules would have an energy sufficient to form a

stable condensate nucleus which attracts more vapor molecules. The cluster has to possess Gibbs free energy of formation, or surpass the energy barrier, in order for a chain reaction to take place. Using the kinetic theory limit for homogeneous nucleation, Eq. 1.1 shows the relation of the pressure difference between a liquid drop (P_l) existing in mechanical equilibrium with a vapor environment (P_v)[1].

$$P_l - P_v = \rho_l R T_v \ln \frac{P_v}{P_{sat}(T_v)} \tag{1.1}$$

Where R, T_v, v_l, and P_{sat} are specific gas constant, thermodynamic equilibrium temperature, liquid specific volume, and saturated pressure at the thermodynamic temperature. A simple calculation using Eq. 1.1 shows that homogeneous condensation of steam is improbable for atmospheric pressure environment because for the previous relation to be valid, the pressure inside the droplet would be greater than the critical pressure. However, for elevated-pressure environments lower subcooling would initiate homogeneous condensation.

This class of condensation is the main working principle of cloud chambers, which are used as a valuable detection system in radiation physics. Additionally, it is faced regularly in petrochemical industry in natural gas pressurized flows [2]. Because this class of condensation occurs away from surfaces, the heat transfer side is often not studied since no heat transfer enhancement could be implemented.

Class II: Heterogeneous condensation

Heterogeneous condensation is a phase-change process that occurs at non-vapor interfaces, i.e. solids or liquids. In contrast with homogeneous condensation, this class requires less subcooling degree because of the abundance of nucleation sites. Depending on the condensation interface, this class can be further classified into film-wise, drop-wise, and volumetric condensation. The first two categories take place on continuous surfaces, while the third category occurs on suspended solid particles or liquid droplets in saturated surroundings.

Film-wise Condensation (FWC) is a process where condensate usually forms a film on a solid surface. The film might be flowing due to applied forces, i.e. gravity or ambient flow, or might build up in the absence of external forces. This process is commonly faced in industry, therefore, it is the most widely studied process in condensation. In this type of condensation, the solid surface is commonly cooled down to temperatures below the saturation point of the surrounding. This, in turn, triggers clusters of vapor to condense near nucleation sites to form droplets which quickly merge to form a film of condensate. Figure 1.1a illustrates the configuration of FWC on an axisymmetric body. In a saturated vapor environment, condensation rate is controlled by the heat transfer through the solid as well as the condensate layer. If the solid is highly conductive, then the local heat transfer coefficient can be derived following the derivation of Nusslet [3] or Dhir and Lienhard [4] as

$$Nu_x = \frac{x}{\delta_l} = \left[\frac{\overline{g}(\rho_l - \rho_v)\rho_l h'_{fg} x^3}{4\mu k \Delta T}\right]^{1/4} \tag{1.2}$$

where the effective gravity is given as

$$\overline{g} = \frac{x(g(x)R(x))^{4/3}}{\int_0^x g(\zeta)^{1/3}R(\zeta)^{4/3}d\zeta} \tag{1.3}$$

The heat transfer coefficient associated with this type of condensation are of moderate magnitudes, usually in the order of 1000-10,000 W/m^2-K [5].

Figure 1.1b presents the case condensation that occurs on a highly wetting surface in the presence of non-condensable gases (NCG). The existence of NCG acts to reduce the heat transfer tremendously as will be discussed in section 1.3. The reason for the reduction in heat transfer is the accumulation of NCG on the liquid-vapor interface, which introduces a thin layer of concentrated NCG mixture, so called *diffusion layer*. At steady state conditions, the condensation rate becomes controlled by the diffusion of vapor through this layer, hence, increasing the resistance to condensation. Heat transfer coefficients associated with such situation reduce to values in the range of 1-1000 W/m^2-K depending on the NCG concentration.

Drop-wise Condensation (DWC) is the process where condensate forms droplets over a solid surface. This process can be summarized by the following sequence of events; initial nucleation of vapor clusters, droplet growth by condensation on the interface, droplet growth by coalescence, droplet fall off, and finally re-nucleation of droplets. Figure 1.2 depicts the sequence of events in both DWC with and without NCG. Droplets grow by direct condensation when the droplet radius is less than the nucleation

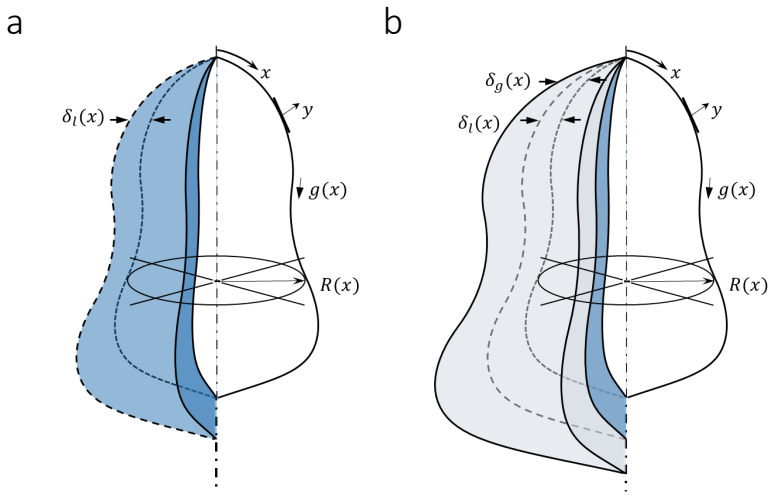

Figure 1.1: Film-wise condensation over axisymmetric bodies; (a) without NCG; (b) with NCG.

sites spacing on a surface. Once two droplets touch, they coalesce to a single droplet which resides on the combined center of mass of the two parent droplets. Once a droplet reaches a certain diameter, its weight or drag forces overcome its surface tension force. Therefore, the droplet falls off sweeping all droplets in its way. In an ideal case, the formed droplets do not initially merge to form a condensate film but persist to expand until they coalesce and fall off the surface, renewing the surface for another condensation event to occur. This type of condensation is encountered in two situations; (1) when the condensation rate is very low such that droplets fall off before merging to form a film of liquid; and (2) at modified surfaces with hydrophobic coatings, patterned hydrophobicity coatings, or nano-structured topology [6, 7].

In case of saturated vapor condensation, heat is first transferred to the liquid droplet by vapor condensation through a very thin layer, so called

Knudsen layer. The thickness of this layer is approximately equivalent to the mean free path of the vapor at the saturation point, therefore, it is prominent for droplet with diameters of a similar length scale. In order for the vapor to condense after passing the Knudsen layer, it needs to overcome the Laplace pressure difference, which takes into account the curvature of droplets. Overcoming the Laplace pressure requires in essence a change in temperature. Then, heat is conducted through the liquid droplet to the wall. Eq. 1.4 is usually used to estimate the heat transfer over a single condensate droplet [8].

$$q_d(r,\theta) = \pi r^2 (T_{sat} - T_s - \frac{2T_{sat}\gamma}{\rho_l h_{fg} r})(\frac{1}{2h_i(1-\cos\theta)} + \frac{r\theta}{4k_l \sin\theta} + \frac{\delta_s}{k_s \sin^2\theta})^{-1} \tag{1.4}$$

Knowing the droplet size distribution over a surface gives excellent estimations of the overall heat transfer rate [9]. This type of condensation is characterized by larger heat transfer rates than FWC, usually in the order of 100,000 W/m^2-K [5]. Because of that, many researchers have focused on fundamentally studying ways to promote this type of condensation and prevent films to form on surfaces.

On the other hand, the presence of NCG introduces another thermal resistance by forming an extra layer that encapsulates the droplet, as shown in Figure 1.2b. This layer, similar to that in FWC, is a mixture that is rich in NCG. The vapor condensation becomes controlled by diffusion through this layer, which could dominate the heat transfer process, if not disrupted by droplets falling off the surface. At the initial stages of condensation, the diffusion layer of each droplet might not overlap. However, as time elapses

the diffusion layer reaches to a steady state. This enables researchers to ignore the behaviour of single droplets and deal with droplets as single layer with an effective thickness. Because the problem becomes a mass diffusion of vapor, Eq. 1.4 is not valid anymore to describe the heat transfer in the problem. Essentially, modelling the heat transfer of FWC and DWC becomes indistinguishable.

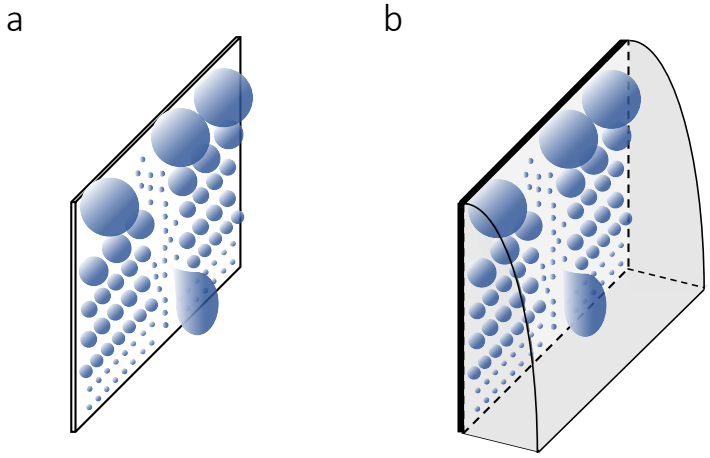

Figure 1.2: Schematic of Drop-wise condensation sequence of events; growth by direct condensation, growth by droplet coalescence, Droplet fall off, and re-nucleation of droplet for the cases of condensation; (a) without NCG; (b) with NCG.

Volumetric Condensation (VC) is a process where condensate forms in bulk over nucleation sites suspended away from surfaces. Cloud formation is an example of this type where saturated vapor forms a cloud or fog when it comes in contact with dust particles or suspended pollutants that are at temperatures below the saturation point [10]. If the nucleation site is made of the condensate, the process is usually called direct-contact condensation

[11]. Even though this type of condensation is naturally selected for the hydrologic cycle, it has not been given its worth of study.

1.1.2 Fundamentals of jet impingement physics

In this section, a background on jet impingement heat transfer augmentation technique is presented. Even though this may seem to disturb the document flow, this background section is important as the technique is utilized in this thesis as a means of improved condensation rate. In Figure 1.3, we show a typical configuration of a jet exiting a nozzle and impinging on a surface in a quiescent ambience. The jet can be called *submerged* or *non-submerged* depending on whether the ambience is of similar density to the jet fluid. From a fluid dynamic viewpoint, the jet can be divided into three regions; (1) *Free jet region*, (2) *stagnation/impingement region*, and (3) *wall jet region*. In the free jet region, flow, thermal, and species fields are not affected by the solid wall downstream. Therefore, the variation of the state variables of this region can be matched with a *free unbounded jet*. The free jet can be divided further into *developing* and *developed* regions, similar to that in pipe flow. The developing region is characterized by a *potential core* that maintains the velocity profile of the nozzle exit. Outside of the potential core, momentum, heat, and mass are exchanged with the surroundings. As a result a smooth transition of the state variable variation is noticed. This region extends to almost five nozzle diameters. In the developed region, the potential core vanishes, and the center line magnitude of state variables start changing. In the stagnation region, the speed of the jet drops to zero at the center of the impingement area and the pressure

builds up to a maximum of $(\rho v^2/2)$. It has been knows so far that heat and mass transfer rates in the stagnation area are significantly high. In the wall jet region, a Blasius-like boundary layer problem could be solved with prior knowledge of the boundary conditions, see Watson for example [12].

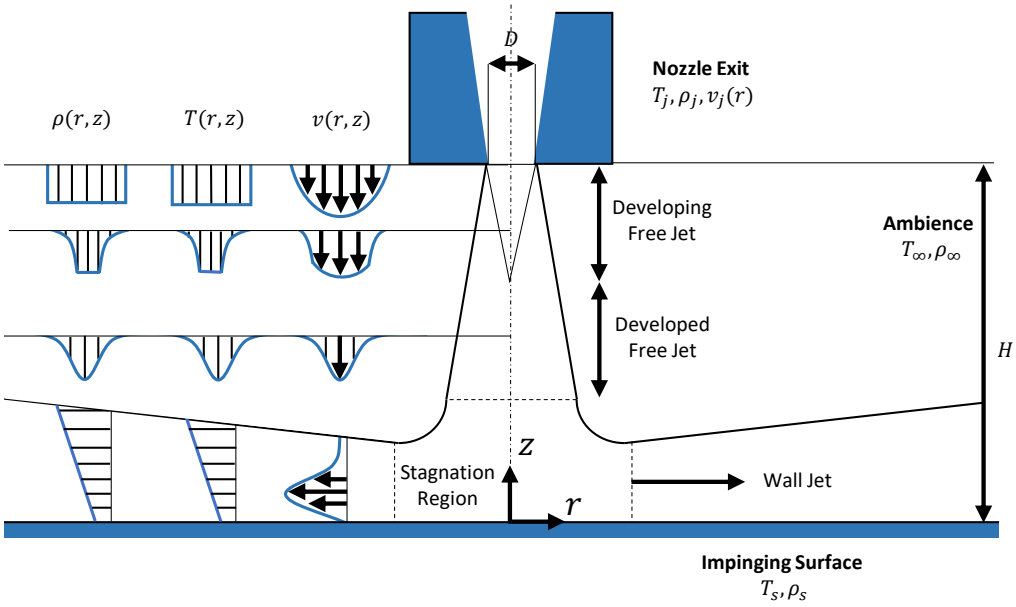

Figure 1.3: General configuration of jet impingement heat/mass transfer along with typical velocity, temperature, and concentration distributions (reconstructed from [5])

Due to the physics complexity, several empirical correlations were obtained under different conditions of single-phase heating or cooling applications. Heat/mass transfer analogy was utilized as well for drying processes. In nucleate boiling, jet impingement has been observed and several models were developed to estimate the boiling curve for such cases. However, no work has been performed to understand the effect of jet impingement during condensation processes. Especially in light of the current improvement of

hydrophobic and superhydrophobic coatings. In the following paragraphs, we visit the literature around jet impingement in different single and multi-phase systems.

Single-phase jet impingement

Most of the studied cases in single-phase jet impingement are for a turbulent nozzle exit, which means a uniform velocity profile at the nozzle exit [5]. Reviews, such as Martin [13], Jambunathan et al. [14] and Viskanta [15], have addressed most of physical phenomena and empirical correlations of gas jet impingement on solid surfaces. Other reviewers, such as Leinhard [16, 17] and Web and Ma [18] focused on liquid jet impingement heat transfer. A major difference between the case of gas and liquid jet impingement is the existence of a hydraulic jump in the latter. Heat transfer by jet impingement is affected by several parameters. We limit our discussion to the effect of nozzle configuration, nozzle diameter, nozzle-to-surface spacing, jet velocity, and the mismatch between jet and ambient temperature and concentration.

The nozzle geometrical configuration has been studied by several researchers [19, 20, 21, 22, 23]. Lee and Lee [20] studied nozzles in the shape of Square-edged orifices, standard-edged orifices and sharp-edged orifices. Gao et al. [22] investigated round nozzles with arrays of triangular tabs. Gulati et al. [21] researched the influence of round, square and rectangular nozzles. In the previous studies, the nozzle configurations seem to be an important factor in enhancing the turbulent mixing of the jet. This in results acts to enhance the heat transfer significantly. Comparison with

fully developed pipe jet impingement showed improvement as high as 55% in stagnation region heat transfer. Additionally, improvements as high as 75% could be achieved by replacing contoured nozzles with orifice nozzles. It has also been noticed that round nozzles produce the least pressure drops compared to square or rectangular nozzles.

It has been practiced almost unanimously that all length scales are normalized by the nozzle diameter (or radius). Even though this could be an obvious choice in the free jet region, it has been generalized to include the stagnation and wall jet regions. The effect of height-to-diameter ratio (H/D) is usually studied in more details [24, 5, 15, 14]. For a uniform nozzle exit velocity, the Nusselt number radial distribution was noticed to behave in two ways. For heights higher than five nozzle diameters, the distribution is characterized by a bell-shaped curve for which Nu monotonically drops from the stagnation point outward. For lower heights, there exists a secondary peak in Nusselt number distribution that may exceed the stagnation point peak. It is interesting to note that a height value of five diameters correspond to the end of the developing free jet and start of a developed one [13].

The effect of jet velocity has been studied theoretically [25, 26] as well as experimentally [27, 19, 14]. Because of the complexity of the problem, the combination of height-to-diameter ratio, radial location and Reynolds number have to be considered. In general a power law of the local Nusselt number was suggested by Jambunathan [14] that takes the form of

$$Nu = kRe^a \tag{1.5}$$

where k and a are constants that depend on height-to-diameter ratio and radial location. Empirical correlations of those constants were obtained from several experimental work. The results were obtained for a turbulent jet with Reynolds number ranging from 5,000 to 124,000. Another correlation that is widely used in literature is that reviewed by Martin [13]. For Jet Reynolds number of 2,000 to 400,000 and height-to-diameter ratio range of 2 to 12, Average Nusselt number in radial locations from 2.5 to 7.9 nozzle diameters are found using

$$\frac{\overline{Nu}}{Pr^{0.42}Re^{0.5}} = \frac{2 - 2.2(D/r)}{(r/D) + 0.1(H/D - 6)}(1 + 0.005Re^{0.55})^{1/2} \tag{1.6}$$

Finally, the problem of mismatch between jet and ambient temperature or concentration was solved by introducing a *recovery* (or an *adiabatic wall*) temperature [28, 29, 30]. Based on those studies, correlations of local heat transfer coefficients should be developed based on the difference between recovery temperature and the surface temperature. Prior to the aforementioned papers, data obtained were scattered since they were based on the difference between jet and surface temperatures. The recovery temperature takes into account the *entrainment* resulting from the diffusive exchange between the jet and the ambience. A derivation of the recovery temperature is reproduced in supplementary material to express admiration of the work of Hollworth and Gero (1985)[28]. By analogy, we derive in Chapter 4 the Breath Figure (BF) spot which we believe is equivalent to a new concept of *recovery concentration*.

Two-phase jet impingement

The term two-phase flow includes but not limited to cases where a phase change takes place. In the area of jet impingement, applications that can be described as two phase flows include drying, spray/mist cooling, nucleate boiling. Here we discuss relevant understanding of such applications.

Drying using jet impingement has been used in food industry [31, 32, 33], textile industry [34, 35] and other applications [36, 37]. For moderate evaporation rate cases, heat and mass transfer analogy is usually sufficient to predict mass transfer rates from heat transfer ones. For example, Martin [13] predicted Nusselt number from Sherwood number using the following analogy equation

$$\frac{\overline{Nu}}{Pr^{0.42}} = \frac{\overline{Sh}}{Sc^{0.42}} \tag{1.7}$$

Now Eq. 1.6 and Eq. 1.7 can be used for both Nusselt and Sherwood numbers interchangeably. This is only valid if the heat and mass transfer are decoupled. Otherwise, such in the case of high evaporation rates or higher density variations, one expect a deviation from the heat and mass transfer analogy.

Another important application where jet impingement is considered is in **flow boiling**. Because in the developing nucleate boiling regime both convective and nucleation heat transfer rates are high, heat transfer rates are significant compared to pool boiling cases. Several studies have been conducted in this field and are categorized to *free* and *submerged* jet impingement boiling [38]. In free jet impingement boiling, a saturated or subcooled liquid jet is impinged on a heated surface in a quiescent gas surrounding.

While a submerged jet is usually characterized by similar jet and surrounding liquids. In case of free jets, several researchers concluded that the jet parameters, such as jet velocity, diameter and subcooling play no significant role in the fully developed nucleate boiling regime [39]. The effects of such parameters is clear in the single-phase region, developing nucleate boiling region, onset of nucleate boiling (ONB), and critical heat flux (CHF). Multiple correlations were developed to estimate the complete boiling curve. As for submerged jet impingement boiling, researchers are still in debate of whether the jet parameters affect the fully developed nucleate boiling region or not [38]. However, the effect of the surrounding subcooling has been shown to influence the entire process. Another crucial factor influencing jet impingement boiling was found to be the surface condition [40, 41, 42]. Even though single-phase region is not influence by the surface wettability, it is a highly controlling parameter in all the other regions. Lower surface wettability, enhances the bubble generation and departure. Therefore, enhances the mixing mechanism that is essential in nucleate boiling. Most of the previous experiments were performed on highly conductive heaters, hence constant surface superheat. In addition, heater dimension was similar to the jet dimension which in turn limits the cases to the stagnation region. However, in other experiments such as those done by Rau and Garimella [43] and Dukle and Hollingsworth [44, 45], the heater area is greater than the jet diameter. For lower conductive heaters or heaters with large areas, the heater are appropriately described in constant heat flux terms. This resulted in a variation of the surface temperature in the radial direction with the lowest temperature being at center of the stagnation area. Interestingly enough,

single phase region, developing and developed nucleate boiling could be observed simultaneously from the center of the stagnation region and radially outward, in the same order. The ONB was formed in a shape of a ring with a stable reproducible size [44]. Researchers have considered numerically studying such behaviour [46, 47, 48, 49, 50, 51]. Numerous numerical models have been developed, such as Eulerian mixture models [46], Eulerian mechanistic model [47, 48, 49], single-phase model [50, 51]. Because of the negligible effect of evaporative heat flux, and the fact that heat transfer is enhanced mainly by the mixing phenomenon caused by bubble departure, the single-phase model seems more appealing. The only modification made to normally solving for state variables is an additional artificial turbulent diffusivity [50, 51].

Jet impingement has been used in **spray or mist cooling technology** [52, 53, 54, 55, 56, 57, 58, 59, 60]. In the case of spray cooling, micro-jets are sprayed directly on a hot surfaces. On the other hand, high temperature steam is expanded abruptly and therefore, condensate droplets are generated and impinged on a hot surface in mist cooling. Evaporative cooling is the main mechanism by which heat is removed from the surface.

Lastly, Jet impingement technique was used to study droplet growth mechanisms on hydrophobic surfaces by different research groups in 1990s [61, 62, 63, 64]. Even though studies were performed to observe the droplet growth by condensation of steam in air environment, less attention was paid to the heat transfer enhancement. In all the experiments, oblique jets were utilized where the jet is not normal to the surface to reduce its shearing effect. In addition, oblique jets were used for better visualization of the

transient droplet growth. In 2019, Ji et al. [65] proposed a quick solution to a sudden NCG leakage in a pure vapor condensation heat exchanger. The solution was to generate a jet of pure steam and impinge the inner tube to break the diffusion layer. They were able to obtain improvements of around two folds compared to the absence of the jet.

1.2 Applications and motivations

Condensation phenomenon is of great importance in numerous natural and artificial processes, yet not fully explored. In nature, condensation is a very important part of the hydrologic cycle, which is considered the main source of fresh water to living species. Many animals and plants rely heavily on condensing atmospheric water to get their share of fresh water. Examples of which are the Darkling beetles [66], and Sequoia Sempervirens [67], to name a few. Additionally, condensation is a pivotal process to huge number of industrial applications ranging from Dip-pen nanolithography [68], to large scale power and distillation plants. In order to promote more efficient applications, improving the condensation process has been the focus of many scientific research. Various condensation heat transfer augmentation techniques have been utilized, these techniques can be classified to; Passive; active; and compound augmentation techniques. In passive augmentation techniques, heat transfer is improved by means of modifying heat transfer surfaces or fluids. Examples of such techniques are; altering wettability of surfaces [6], geometrical modifications of surfaces [69, 70, 71], inserted devices [72, 73], and fluid Additives [74]. Unlike passive augmentation tech-

niques, active techniques require an external force to be applied either on the heat transfer surface or fluid. Unsurprisingly, passive augmentation techniques have caught major attention of the heat transfer community because of their easier implementation in existing heat transfer applications. Contrarily, active techniques require additional equipment to exert the required forces to enhance efficiency of heat transfer applications. This, in turn, means higher capital expenditures (CAPEX) and operating expenses (OPEX). I believe that the first impression of active techniques caused by this disadvantage prevented further research to advance in this front. However, observing the state-of-the-art literature in passive augmentation techniques shows that the most promising technology of them all, i.e. altering surface wettability, still has a long way to go in terms of chemical and physical stability over time especially at elevated temperatures [75, 6, 76]. The stability issue as well as the higher CAPEX and OPEX of current coatings render such technique highly infeasable [77]. From my viewpoint, the most important concern passive augmentation techniques has not resolved is the degradation of heat/mass transfer coefficients caused by the existence of non-condensable gases (NCG).

Condensation in the presence of NCG is termed Breath Figure Condensation (BFC) in this document for referencing simplicity. The name was chosen not to be confused with other condensation types, such as Dropwise or Film-wise condensation which are specific for condensation of pure vapor. The name originates from several papers titled *Breath Figures* by the great scientists Aitken and Rayleigh (1895-1913) [78, 79, 80]. The name is self-explanatory as the phenomenon of breathing against a clean surface

generates droplets that scatter incident light which makes them appear cloudy. Looking microscopically at those figures shows that micron-sized droplets are present on the surface which explains the scattering of light. In the subsequent section, I will lay out the problem of condensation with NCG and how this issue was mitigated humbly in previous research.

1.3 Problem complexity and possible contributions

The presence of minute amounts of NCG in a condensation process has shown to deteriorate the efficiency of the process dramatically. It was first reported experimentally by Othmer in 1929 [81], that an existence of air with mass fraction of 0.005 reduces heat transfer to the condenser surface by about 50% of the pure vapor condensation case. The reason of this reduction is the accumulation of NCG on the liquid-vapor interface, which introduces a film of high NCG-content mixture, so called *diffusion layer*. At steady state conditions, the condensation rate becomes controlled by the diffusion of vapor through this layer, hence, increasing the resistance to condensation. It has been reported by several researchers that this layer's heat transfer resistance is dominant even for very small bulk NCG content thus controlling the heat transfer process. Even though experimental studies have been successful in reducing their effect by means of vacuuming test chambers to environment, it is a highly impractical solution in large scale equipment. NCG can break through equipment via leak points, which is a problem of its own, or as a chemical reaction product of vapor interacting with the equipment material [82].

In efforts to mitigate the negative effect of NCG, other active techniques have been utilized, such as extended surfaces [83, 84, 85]; direct contact between gas and cooling medium [86, 87, 88, 89, 90, 91]; and different NCG carriers [92, 93]. Even though the former two solutions are promising, the latter seems to address the problem at its core, i.e. the effect of vapor diffusion through the diffusion layer which in result affects the heat and mass transfer. However, improvements from those techniques come with great material cost (former two techniques) or industrial impracticality (latter technique). Investigating the problem of NCG further shows that the solution lies within two possibilities; (1) increasing heat/mass transfer contact area (A); (2) increasing heat/mass transfer coefficient (h). The optimal solution should be obtained by maximizing the design parameter (hA/cost). The cost consists of the additional equipment as well as the material volume. A third extreme possibility is to utilize the transient diffusion of vapor. The build up of the diffusion layer is intrinsically transient with a time scale, i.e. total build up time of the diffusion layer, that has a proportionality, discussed in chapter 3, to the NCG content in the bulk mixture. Because mass transfer coefficient is inversely proportional to the thickness of the diffusion layer, vapor diffusion should start by a very high magnitude then drops to its steady state value with time. As a result, most of the previous experimental work on condensation heat transfer required very elongated periods and special techniques to ensure steady state conditions, especially experiments with highly pure vapor [9, 94].

1.4 Research objective and document overview

The discussion above has highlighted a general understanding of the condensation and jet impingement physics. In this thesis, I intend to have a better understanding of the nature of condensation, especially with the existence of NCG. In order to achieve this purpose, in **Chapter 2**, a numerical model of BFC is developed. The effect of pertaining parameters affecting the condensation process are discussed. With this basic understanding, we recognize that further improvement of condensation could be obtained by thinning the diffusion layer. Additionally, the frequent mixing of the diffusion boundary layer acts to further enhance condensation rates. In **Chapter 3**, we simplify the transient growth of the diffusion layer by modeling two semi-infinite media in contact. Both energy and species transport were considered to obtain a general understanding of the problem. Considering our understanding from the previous chapters, jet impingement technique is considered as an excellent means for thinning the diffusion layer as well as shedding droplets which provides frequent mixing of the layer. In **Chapters 4** and **5**, the problem of condensation due to jet impingement of humid air on a cooled surface is considered. The first observation is the existence of a BF spot (fogging spot) once the jet comes in contact with the surface. This observation is further studied and modelled in **Chapter 4**. The droplet shedding capability of stagnation flow is considered in **Chapter 5**. With the outstanding shedding capability due to jet impingement, condensation and heat transfer rates were evaluated. Finally, general conclusions from this research relating to the improved BFC are discussed in **Chapter 6**.

CHAPTER 2

Numerical Modeling of Breath Figure Condensation

In this chapter, a computation model is developed to study the effect of NCG on the condensation process. The following sections discuss the objective of this model, governing relations, methodology, and model validation.

2.1 Chapter objective

The prime objective of this chapter is to develop a computational tool that enables us to better understand BFC and explore several augmentation techniques for improving the condensation rate. Additionally, the tool allows to design better experiments to study the phenomenon.

2.2 Literature review

Modelling the condensation process has been initiated by the theoretical work of Nusselt in 1916 [3]. Since then, researchers have been developing different theoretical as well as numerical models to simulate the condensation process of different geometries and environmental conditions. Huang et

al. [95] classified these models into theoretical and semi-theoretical models. The former class includes the boundary layer, diffusion layer, and mathematical methods. The latter class includes the degradation factor, and heat/mass transfer analogy methods. In the following paragraphs, we focus our literature survey to the state-of-the-art literature on utilizing numerical techniques to simulate the condensation process.

Saraireh et al. [96] used FLUENT software to simulate condensation of water vapor in plain channels with the existence of NCG. Continuity, momentum, energy and species conservation equations were solved to obtain heat transfer coefficients for different boundary conditions. The wall was assumed to be dry and the condensation was limited to the diffusion rate of vapor in the vapor-air layer adjacent to the wall. Results showed a good agreement with experimental work for the high NCG concentrations studied in their work.

Cheng and Junming [97] simulated laminar forced condensation of humid air flowing over a vertical plate using an in-house software. By solving the governing conservation equations in both liquid and gas-vapor regions, they obtained good agreement with empirical correlations. The solution was performed by first assuming a liquid film profile along the flow direction, then iteratively solving the equations to correct for the initial guess. Some discrepancy was encountered during validating this model with experiments due to their laminar flow constrain. Waviness of the liquid film as well as transition to turbulence occurs at fairly low film Reynolds numbers [1].

Jun-De Li [98] included the effect of turbulence to simulate condensation in vertical cylindrical condensers. Among the several assumptions here, it

is noted that the simulations were for steady state and negligible liquid film thicknesses. The latter assumption especially renders this simulation valid only to high NCG concentrations where the effect of the diffusion layer is dominating. In this work the boundary layer conservation equations were solved numerically using FLUENT in the internal and external regions of the condenser pipe as well as the tube wall. Realizable k—ϵ model was adopted with model constants of ($C_{1\epsilon} = 1.44$, $C_2 = 1.9$, $\sigma_k = 1.0$, and $\sigma_e = 1.2$). Sink terms were added to the governing equations at the cells adjacent to the condensation interface, i.e. pipe's wall. The sink terms act to account for the mass, momentum, and energy loss due to condensation in the vapor-gas mixture,

Concurrent to the previous work, Dehbi et al. [99] published a numerical technique utilizing FLUENT as well to simulate steam condensation in the presence of NCG for different geometries as well as broader range of environmental conditions. Different limitations were listed in this work, namely ignoring the liquid film thermal resistance. This, just as the previous work, limits the validity of this technique to very high NCG contents, i.e. >10 wt.%. The researchers also derived an effective mass diffusion coefficient to account for the suction effect on a wide range of operating pressure up to 12 bars and temperatures of 300 K to 500 K. Due to the high computational cost, A. Dehbi (2013) [100] investigated the adequacy of wall functions to predict condensation rate of this model. Due to the fact that most condenser applications are of large volumes, along with the need of accounting for sink terms at the interface-adjacent cells, very fine grids were required. Utilizing wall-function approach (WFA) over resolved boundary

layer approach (RBLA) was investigated on different length scales of the condenser plates. The reduction of computational cost using the WFA was obtained with the expense of losing accuracy and limiting its use to fully developed flows. Further experimental work was done to verify this model for relatively small scale condensers with high NCG contents by different researchers [101, 102, 103, 104, 105].

Fu et al. [106], argued that the suctions effect in the work of Dehbi et al. [99] is an unnecessary step to account for in high NCG concentrations since FLUENT solves the governing equations directly. Therefore, a similar formulation to that of Dehbi et al. [99] except for ignoring the suction effect was adopted to simulate condensation of steam with air and helium in a vertical tube. The wall temperature was obtained from experimental observations and heat transfer rates were matched to validate the model. They showed that the suction effect, represented by the radial velocity component, becomes significant for high NCG mass concentrations while Reynolds number has a marginal effect on it. It is worth noting here that in the work of Dehbi and co-workers [99], the suction effect was included to account for the no-slip boundary condition at the condensation interface. Yoon et al. [107] suggested the use of a slip or shear-free boundary condition and no further correction to the suction effect was required.

Li et al. [108] simulated the case of dehumidifying air using fin-and-tube heat exchangers using similar numerical technique of Dehbi's group except with ignoring the momentum source terms. Results showed a great agreement with the experimental data for relatively high velocity around the circular fins up to 2.5 m/s.

Zhang et al. [109] modeled methane liquefaction with the existence of nitrogen by splitting the domain into liquid and vapor-gas mixture. Solving the general governing equations with specific sink and source terms in both domains and utilizing the volume-of-fluid (VOF) method made it possible to obtain good agreement between experiment and numerical work. A similar iterative solution to that of Cheng and Junming [97] was adopted to track the condensate film thickness.

The work of Yin et al [110] discusses the condensation with and without NCG in minitubes. The VOF method was utilized to trace the liquid-gas interface because of the low NCG volume fractions, i.e. 0.5%-3%. The flow pattern studied was an annular flow resembling the FWC presented in this work. Results have been validated favourably against analytical solutions. Various NCG were simulated to check the effect of thermal as well as mass diffusivities on the condensation process along the tube.

The complexity of interface tracing techniques led researchers to resort to approximate equations to assess heat and mass transfer coefficients of condensation with low NCG fractions. Wu et al. [111] developed an approximate solution combining thermodynamic relations, analytical solution, and empirical correlations to obtain liquid-gas interfatial temperature as well as heat flux on surfaces.

Despite the tremendous amount of empirical and semi-empirical correlations to obtain the overall heat transfer coefficient during vapor condensation with NCG, they are of limited use due to their applicability to certain geometries and environmental conditions. While some numerical models have been developed to overcome this deficiency, computational cost and

complexity are still of major concerns. It is noticed that in the surveyed literature, researchers have adopted two options in modeling the condensation process. They are by either neglecting the condensate film or by physically including it. The former option is a good approximation for NCG fractions above 10%, since the thermal resistance of the diffusion layer becomes dominant. The latter option has been recognized by tracking the interface and modifying it in an iterative procedure. This option is valid without any restriction on the NCG fraction. However, the effect of turbulence and waviness of the interface becomes difficult to capture which results in an underestimation of the condensate film thermal resistance. In addition, it is computationally expensive to apply this model for the entire range of NCG fractions. Therefore, it is imperative to develop a model that is valid over the entire range of NCG fractions, i.e. 0-100%. This model is of importance for prediction of the transient condensation process in cases such as accidental leakage of NCG in industrial condensers that utilizes pure vapor. The prime objective of this work is to simulate the condensation process with the existence of NCG on condensers where FWC is dominant over the entire NCG fraction range.

2.3 Numerical model development

Figure 2.1a presents the configuration of almost all practical condensation surfaces with an illustration of the condensate film as well as the diffusion layer. Figure 2.1b shows the reduction of such three dimensional geometries into a two dimensional domain along with boundary conditions depicted.

Further discussion of the boundary conditions is given later in the document. In order to simulate the condensation process, one recognizes the importance of solving the state variables, i.e. temperature, pressure, velocity, mass fraction, both in the condensate film and the gas-vapor domains. While each domain can be solved separately, the condensation interface acts as a coupling boundary condition. In the following paragraphs the governing equations in the two regions are presented and simplifying assumptions are made to reduce the computational time without compromising the accuracy of the solution.

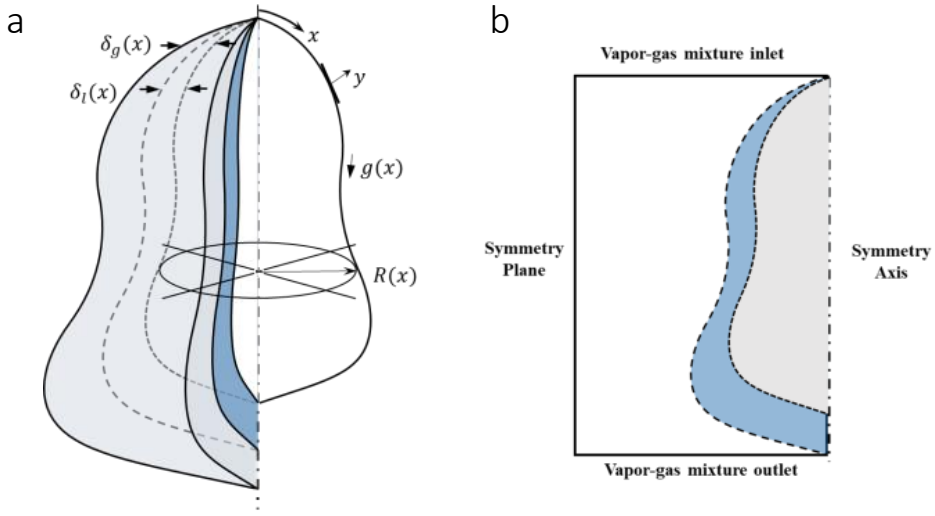

Figure 2.1: (a) A typical configuration of a condensation surface; (b) 2D Axisymmetric reduction of the geometry along with boundary conditions illustrated.

The following simplifying assumptions are made;

1. Air is handled as a single phase, therefore, water vapor and air are

modeled as a binary gas mixture.

2. The gaseous mixture is assumed to follow the ideal gas law restricting the pressure and temperature to those of the ideal gas law conditions.
3. The liquid-gas interface is at thermodynamic equilibrium, i.e. temperature drop due to Knudsen layer is neglected [112].
4. The advective heat transfer mode in the condensate film is accounted for by a modified latent heat as described in numerous sources [5].
5. The velocity of the condensate film is very small compared to the adjacent gas mixture [3], therefore, it is neglected except in the derivation of the local condensate film thickness. That is, the liquid-gas interface is assumed to introduce a no-slip boundary condition in the gas mixture region.

With these assumptions, the governing equations in the two regions are summarized as follows:

Condensate film region: The layout of solving the state variables in this region was first introduced by Nusselt in his famous film theory [3]. Hence, no further details are given to the derivation of the state variables. The only assumption that is relaxed from the derivation of Nusselt is that the liquid-gas interface exists at an intermediate temperature (T_o), that is to be determined following an iterative solution method presented later in this document. The solution of Nusselt was then expanded to include the fact that the liquid-gas interface could be wavy or turbulent by Kutateladze and Labuntsov [5]. The concluded results of Nusselt number at different

film Reynolds number is given in Eq.2.1 for a vertical wall condenser. In case of other geometries, one could refer to existing solutions, such as the work of Dhir and Lienhard [4] for axially symmetric geometries which are summarized in Table 2.1. If the interfacial temperature (T_o) is known, one would easily obtain the average heat transfer coefficient of the condensate film.

$$\overline{Nu}_L = \frac{\overline{h}_L(\nu_l^2/g)^{1/3}}{k_l} = \begin{cases} 0.943P^{-1/4} & P \leq 15.8 \\ \frac{1}{P}(0.68P + 0.89)^{0.82} & 15.8 < P \leq 2530 \\ \frac{1}{P}((0.024P - 53)Pr_l^{1/2} + 89)^{4/3} & P > 2530 \end{cases} \tag{2.1}$$

Where the P-factor is a rearranged Reynolds number given by Eq.2.2

$$P = \frac{k_l L(T_o - T_s)}{\mu_l h'_{fg}(\nu_l^2/g)^{1/3}} \tag{2.2}$$

Gas mixture region: The full continuity, momentum, energy, and species transport equations are solved without any additional source/sink terms, opposite to the previously studied models. The usual governing relations are presented here for the sake of completeness, but further details can be obtained from classical convective heat and mass transfer textbooks. The continuity, momentum, energy, and species transport equations are given in Eq.C.7-C.10, in a respective order.

$$\frac{\partial \rho_g}{\partial t} + \nabla \cdot (\rho_g \overrightarrow{v}) = 0 \tag{2.3}$$

Table 2.1: Average Nusselt number of axisymmetric condensation surfaces, adopted from [4].

Condenser configuration	Average Nusselt number $\overline{Nu}$
Horizontal cylinder	$0.729\left[gD^3/A\right]^{1/4}$
Upper half of a horizontal cylinder	$0.866\left[gD^3/A\right]^{1/4}$
Lowe half of a horizontal cylinder	$0.592\left[gD^3/A\right]^{1/4}$
Stationary cone	$0.874\left[\cos(\alpha/2)gx^3/A\right]^{1/4}$
Stationary sphere	$0.785\left[gD^3/A\right]^{1/4}$
Rotating horizontal disk	$0.9036\left[\nu_l^2/A\right]^{1/4}$
Rotating vertical Plate	$0.760\left[\nu_l^2/A\right]^{1/4}$

D: diameter, Ω: angular velocity, α: cone angle, $A = \nu_l k_l (T_o - T_s)/\rho_l h'_{fg}$

$$\frac{\partial}{\partial t}(\rho_g \overrightarrow{v}) + \nabla \cdot (\rho_g \overrightarrow{v}\,\overrightarrow{v}) = -\nabla P + \nabla \cdot \overline{\overline{\tau}} + \rho_g \overrightarrow{g} \tag{2.4}$$

$$\frac{\partial}{\partial t}(\rho_g E) + \nabla \cdot (\overrightarrow{v}(\rho_g E + P)) = \nabla \cdot (k_g \nabla T - \sum_j h_j \overrightarrow{J_j}) \tag{2.5}$$

$$\frac{\partial \rho_j}{\partial t} + \nabla \cdot (\rho_j \overrightarrow{v}) = -\nabla \cdot \overrightarrow{J_j} \tag{2.6}$$

Where $E \approx h$ neglecting pressure work and kinetic energy. The total enthalpy is a mass weighted average of each species enthalpy. The species enthalpy is given by Eq.C.11.

$$h_j = \int_{T_{ref}}^{T} c_{p,j} dT \tag{2.7}$$

The term $\overrightarrow{J_j}$ in Eq.C.9 and Eq.C.10 refers to the Fickian diffusive mass flux of each species which is given by Eq.C.12

$$\overrightarrow{J_j} = -D_{j,i}\nabla\rho_j \tag{2.8}$$

Closure relation: The coupling between the two regions is through the liquid-gas interface. Because Nusselt film analysis was chosen for this work, we only need to apply an energy balance at the interface. As discussed in many research articles [95], the heat conducted through the liquid layer originates from both the sensible and latent heat from the gas mixture region, therefore, one can easily derive Eq.2.9.

$$T_o = T_s + \frac{1}{\overline{h}_L}(-k_g\frac{\partial T}{\partial y} + \dot{m}_v h_{fg})\Big|_{n=0} \tag{2.9}$$

The value of the condensation mass flux in Eq.2.9 is corrected with a suction effect factor, that is outlined in numerous mass transfer text books, such as [113]. The suction effect factor is given in Eq.D.3.

$$\phi = \frac{1-\omega_{v,o}}{\omega_{v,o}-\omega_{v,\infty}} ln\left(\frac{1-\omega_{v,\infty}}{1-\omega_{v,o}}\right) \tag{2.10}$$

The total condensation flux is then calculated as $\dot{m}_v = \phi J_v$. In the previous equations, all thermophysical properties are taken as state-variable dependent; using the kinetic theory for the gas-vapor domain, and thermodynamic tables for the condensate film domain.

Boundary conditions: The previous equations are not limited by dimensionality, therefore 1D; 2D; and 3D geometries could be simulated. Depending on the flow and temperature conditions of a given problem, velocity or pressure conditions could be specified at the inlet and exit sections. In addition, the mass fraction of both species should also be specified. Because this model assumes the condensate film follows the Nusselt film theory, solution of the film thickness as well as temperature and velocity profiles are known once the interfacial temperature is known. The boundary condition at the condensation interface are the no-slip velocity condition and no-jump temperature condition. At the interface, the vapor mass fraction is the saturation mass fraction at the interfacial temperature which is given in Eq. 2.11.

$$\omega_v = \left[1 + \frac{M_a}{M_v}\left(\frac{P}{P_{sat}} - 1\right)\right]^{-1} \tag{2.11}$$

where the saturation pressure is obtained from thermodynamic tables at a given interfacial temperature. Semi-empirical correlations, such as Antoine equation could be used to encode the saturation pressure. Finally, the region far away from the condensing surface is assumed to be a symmetry plane, i.e. no gradient in any of the state variables.

2.4 Numerical methodology

A commonly used Finite Volume Method (FVM) is utilized to solve the governing equations in the vapor-gas mixture domain while Engineering Equation Solver (EES) is linked to perform the iterative solution outlined in Figure 2.2. The iterative solution starts by assuming an interfacial temperature

that is between that of the ambience and the condenser wall. Thermophysical properties of the vapor-gas mixture, i.e. density, thermal conductivity, specific heat, viscosity, and mass diffusion coefficient, are evaluated using the well-documented kinetic theory of gases. The thermophysical properties of the liquid are obtained using EES at an effective condensate film temperature. This allows studying variable properties during the condensation process. For any specific problem, initial and boundary conditions are applied as discussed in section 2.3. Using equation 2.11, the vapor mass fraction at the assumed interfacial temperature is found as an initial guess. Next step is to solve the governing equations and obtain the total heat transfer and condensation rates to the condenser wall. The interfacial temperature is then corrected using equation 2.9 and the process is then repeated until the correction of the interfacial temperature is minimal. It is worth mentioning that starting with an initial interfacial temperature of $T_o = (T_s + T_\infty)/2$, results in a fast and systematic convergence of the iterative solution. There was no change of result based upon the initial choice given that we are in the mentioned range. Normally, two to three iterations will result in sufficient convergence. The average computational time of our model was 10 minutes on a computer with a processor of Intel(R) Core(TM) i5-7300U CPU @ 2.60GHz 8.00GB(RAM).

2.5 Numerical validation

We validate the current model against two published research work; (1) classical experimental work of Uchida [114] and Tagami [115]. (2) analytical

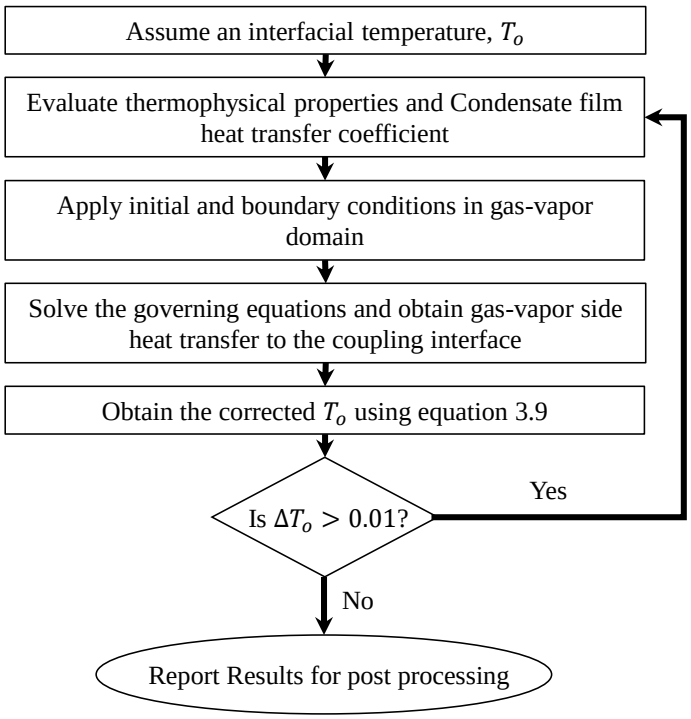

Figure 2.2: Flow chart of the numerical solution of the condensation problem.

solution of Sparrow and co-workers [116, 117]. In the first validation case, a comparison between this model and that of Dhebi's group is presented and the improvement this model provides is elucidated. For both validation cases, we compare our model with heat/mass transfer analogy to show the similarities between the two solutions.

2.5.1 Case 1: Comparison with experimental data

The classical correlations of Uchida and Tagami (1965) have been extensively used in nuclear industry. Even though their experimental work have

been performed on vertical plates, the correlation has been generalized to give a rough estimate of the heat transfer coefficient at different air mass fractions. In their work, vertical plates of certain heights (0.3 and 0.9 m) were placed in a large environmental chamber. The chamber was supplied with known concentration ratios of vapor-gas mixture and steady state was assured. The vapor mass concentrations were (9 to 77 %) and (20 to 60 %) for Uchida and Tagami, respectively. Because there was no direct measurement of the velocity of vapor-gas mixture near the condenser plate, many researchers have assumed natural convection dominates the condensation process. The overall heat transfer coefficients provided from their experimental work are given in Eq.2.12 and Eq.2.13.

$$U_{Uchida} = 380\Big(\frac{\omega_v}{1-\omega_v}\Big)^{0.7} \tag{2.12}$$

$$U_{Tagami} = 11.4 + 284\Big(\frac{\omega_v}{1-\omega_v}\Big) \tag{2.13}$$

In order to refrain from repetition, the objective of this simulation case is to validate the model as well as compare it to that of Dehbi's work [99]. Hence, similar model conditions were applied, a summary of which is in Table C.1. The geometry is similar to that shown in Figure 2.1b with a vertical condenser wall, i.e. constant radius in axisymmetric terms. Because no information was given about the inlet velocity, we assumed a very small velocity, i.e. 0.1 m/s, to maintain natural convection at the isothermal wall. The outlet condition was set to a pressure outlet, where all back-flow conditions, if any, were set to that of the inlet conditions. The opposite

Table 2.2: Environmental conditions of Uchida and Tagami, Numerical error calculated as $\varepsilon = (U_{model} - U)/U$

Run	$\omega_{v,\infty}$ (%)	P_∞ (bar)	T_∞ (K)	U_{model} (W/m^2K)	ε_{Uchida} (%)	ε_{Tagami} (%)
1	80	11.8	454	919.3	8.33	19.8
2	70	7.10	428	609.3	11.4	9.6
3	65	5.85	420	523.8	10.6	2.8
4	60	4.88	410	437.1	13.4	0.1
5	50	3.60	396	287.8	24.3	2.57
6	40	2.77	382	232	18.9	15.6
7	30	2.18	369	172	18.1	29.2
8	10	1.37	334	85	4.14	97.9

surface to the condenser wall was set to a symmetry boundary condition and was placed far away from the boundary layer, i.e. 30 cm away. The height of the condenser wall was set to 1 m as suggested by Dehbi's model.

Turbulent simulations were performed with the aid of wall function approach (WFA) in a similar procedure that was followed by the previous work [100]. Grid independent solution was reached after 30,000 cells with Y-plus value less than 2.76. Figure 2.3 shows the result of the simulated case at different conditions along with a re-simulated Dehbi's work for the current two-dimensional geometry. In order to consolidate the results obtained by both simulations, the empirical correlation of A. Dhebi [118], as well as heat/mass transfer analogy solutions were plotted (details are in Supplementary Material). The Dehbi's model and the current model seem to match each other to a great extent with minor deviations that could be attributed to minor numerical errors. The heat/mass transfer analogy gave a good prediction of the overall heat transfer coefficient and was close to the simulated results. The empirical correlation seem to have the highest deviation due to its wide applicability as suggested by the author [118].

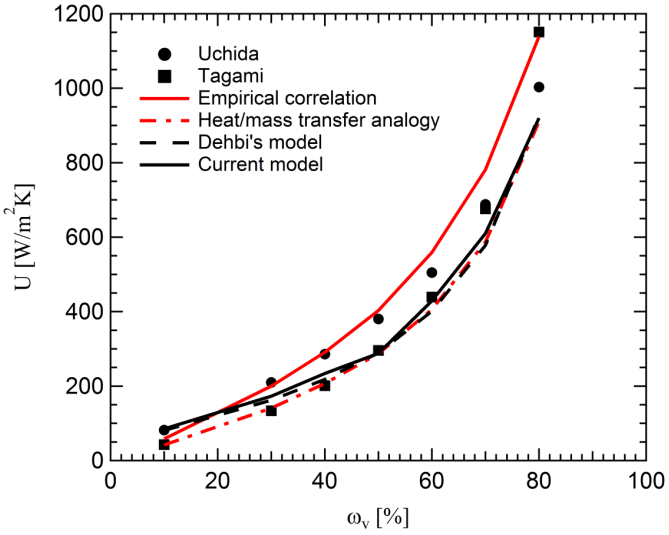

Figure 2.3: Overall heat transfer coefficient at different vapor mass fractions.

The limitation of Dehbi's model is that the condensate film thermal resistance is negligible compared to that of the diffusion layer. The current model, as discussed earlier, relaxes this assumption and solves for both domains. Figure 2.4 shows the thermal resistances obtained from the current model of both the condensate film and the diffusion layer. We notice that for very low vapor mass fraction, the thermal resistance are almost two order of magnitude different. However, the difference is reduced as the vapor mass fraction increases. Even for a value of 80% vapor mass fraction, we note the applicability of Dehbi's model in which ignoring the condensate film is plausible in predicting the overall heat transfer coefficient.

Figure 2.5 compares the interfacial temperature predicted by the current model with that assumed by Dehbi and other correlations. It is clear that after a vapor mass fraction of 50%, Dehbi's model underestimates the

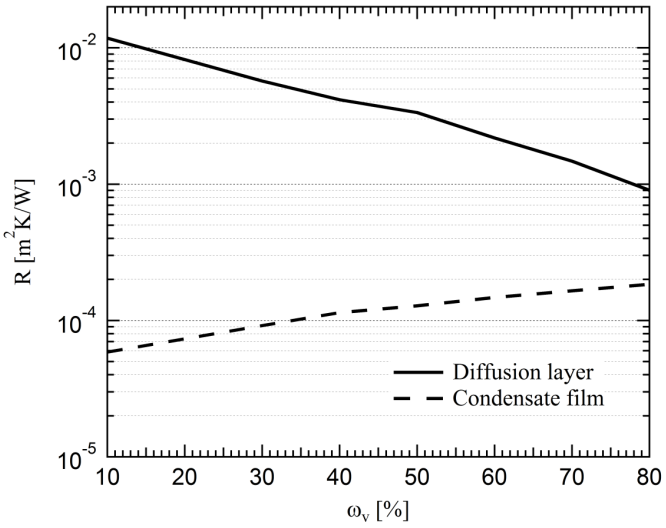

Figure 2.4: Thermal resistances of the condensate film and the diffusion layer at different vapor mass fractions.

interfacial temperature. At vapor mass fraction of 80%, neglecting the condensate film thermal resistance underestimates the interfacial temperature by about 20 K. One would expect even higher deviations when the NCG mass fraction becomes smaller, i.e. approaching the subcooling degree for pure vapor. The current model shows a good agreement with the semi-empirical model obtained by heat/mass transfer analogy. Underestimating the interfacial temperature may not be of importance in calculating the overall heat transfer coefficient for the simulated cases, but is crucial in optimizing condensation heat exchangers.

2.5.2 Case 2: Comparison with analytical solution

Sparrow and co-workers [116, 117] studied analytically the condensation heat transfer over vertical and horizontal plates with laminar natural and

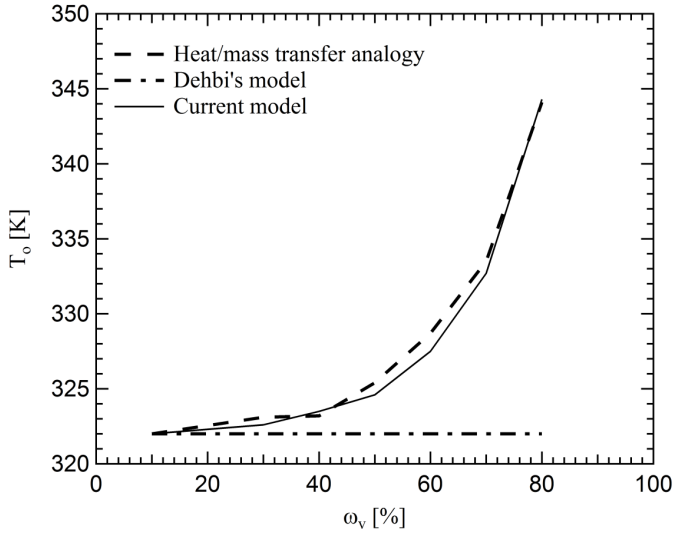

Figure 2.5: Temperature at the condensation interface as predicted by the current model and others.

forced convection. In this section, we validate our model against their analytical solution. The objective of this case is to show the applicability of the current model to simulate condensation of vapor with high vapor mass fractions, i.e. higher than 90%. The studied cases are summarized in Table 2.3. A total of 32 cases were simulated for a fixed ambient temperature with varying wall subcooling degree and vapor mass fraction.

Figure 2.6 shows the results obtained by the current model along with the analytical and heat/mass transfer analogy solutions. Plots show the ratio between the heat transfer rate predicted and that of pure vapor condensation obtained from Nusselt analysis. The semi-empirical solution underestimate the heat transfer rates for all cases due to the experimental uncertainty in the used correlations. The current model on the other hand shows a striking agreement with both the analytical and semi-empirical

Table 2.3: Environmental conditions of Sparrow and co-workers

vapor mass fraction ω_v (%)	Absolute pressure P (bar)	Ambient temperature T_∞ (F)	Wall subcooling degree $\Delta T(F)$
90-99.5	1.08-1.01	212	5-40

solution at most of the given cases. Figure 2.6a-c shows almost a perfect match between the two solution with a maximum deviation of less than 10% which occurred at the higher subcooling degree of the case of vapor mass fraction of 98%. Figure 2.6d shows higher numerical uncertainty because of the minute amount of NCG concentration, i.e. 0.5%. At this point, we expect the thermal resistance of the condensate film to be of high magnitude compared to that of the diffusion film. Consequently, the condensation rate is higher and the effect of the diffusion layer starts to diminish. Because the current model takes into account the importance of the condensate film, this could not explain the high deviation between the analytical and model solutions. In all the previous cases, the inlet velocity was set to be very low, i.e. 0.1 m/s, to conserve continuity of the vapor-gas mixture because of the drainage occurring at the surface due to natural convection. However, for the last case, we notice that natural convection is very high and the preset inlet velocity is limiting the value of heat transfer rate. Hence, another set of simulations were performed with a higher inlet velocity, i.e. 1 m/s, while ensuring that natural convection is still dominating. Figure 2.6d shows that the analytical solution lies in between the two simulated solutions. It is observed that at low subcooling degree, a low inlet velocity is a reasonable approach, however, for a higher subcooling degree, i.e. higher natural convection driving force, a higher inlet velocity is required.

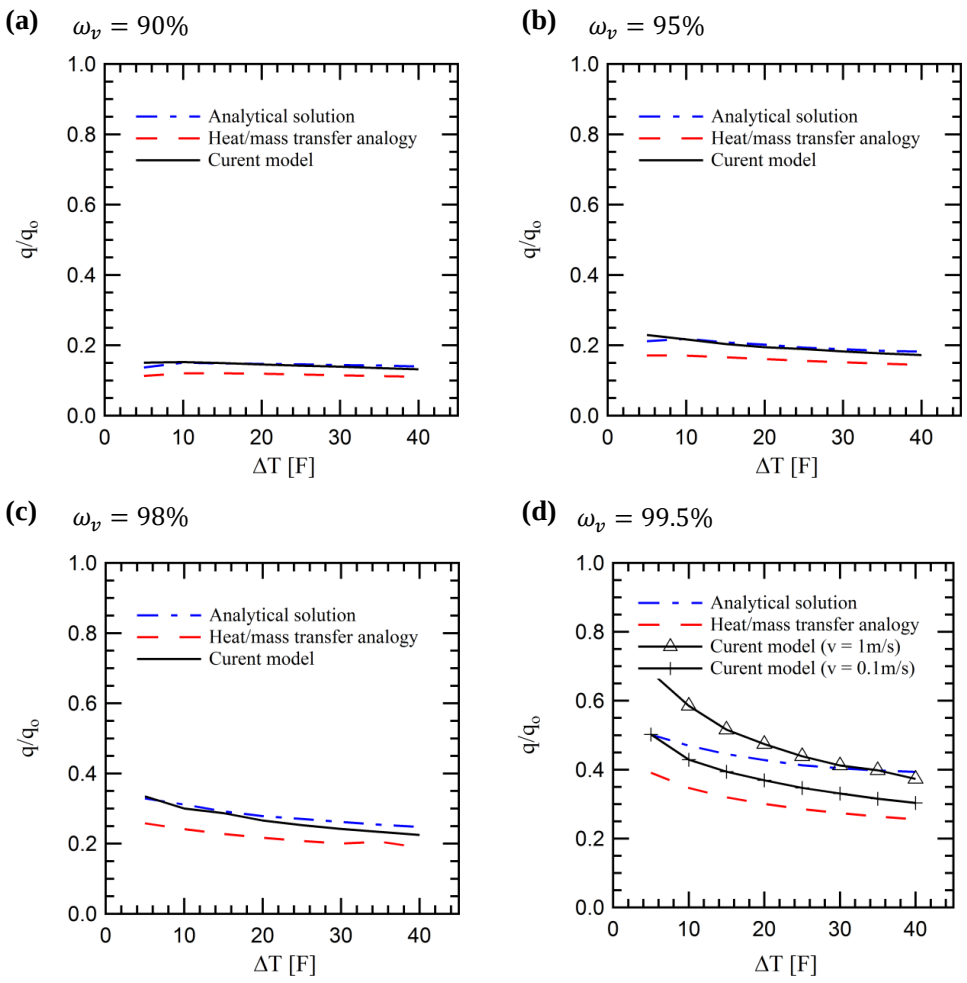

Figure 2.6: Heat transfer rates at different vapor mass fractions and subcooling degrees as predicted by different models.

2.6 Summary and concluding remarks

A numerical model was developed to study the process of vapor-NCG condensation on surfaces characterized by film-wise condensation. Both the condensate film and the diffusion layer were modelled separately and the condensation interface was utilized as a coupling boundary condition. In our literature survey, we noticed that previous simulations adopted two methods for modeling the condensation process;(1) ignoring the condensate film or (2) interface tracing. The former proves to be valid for high NCG fractions, usually in above 10%. The latter adds an additional cost to the computation especially when used to simulate condensation with high NCG fractions. Unlike other models, this work proves to be computationally non-expensive and uses physical intuition to obtain reasonably accurate heat and mass transfer characteristics. The main concluding remarks can be summarized as follows.

1. The current model was first validated against the classical work of Uchida and Tagami, resulting in a good agreement within the experimental uncertainty. In order to contrast our model with the state-of-the-art simulation, we compared our results to Dehbi et al. [99]. Results showed a great agreement between the two models indicating that our model works quite well with NCG fractions above 10%.

2. In order to study the applicability of ignoring the condensate film effect on the condensation processes, thermal resistances of both the condensate film and diffusion layer were assessed. Results indicated that for the cases studied of NCG above 20%, the condensate thermal

resistance was an order of magnitude lower than that of the diffusion layer. This indicates models that ignore the condensate film are valid to predict the overall heat transfer rates. However, as the mass fraction of NCG becomes smaller, the two thermal resistances become comparable in magnitude and both should be considered.

3. Despite the valid prediction of overall heat transfer rates, the models that ignore the condensate film thermal resistance under-estimate the interfacial temperature. This, in turn, might result in inaccurate heat exchanger designs or unpredictable chemical interactions that may depend on temperature near the surface.

4. To validate the current model against condensation processes with low NCG fractions, we simulated the classical work of Sparrow et al. [116, 117]. Results showed a great agreement between the two solutions at different NCG mass fractions (0.5-10%) and subcooling degrees (5^oF-40^oF). With this simulation, the current model prove to work quite well with the entire range of NCG mass fraction, i.e. 0-100%.

5. We also compare this work to the heat/mass transfer analogy because of the similarity of our model to it. Results showed an excellent match between the two models with better accuracy to our current model, especially at low NCG fractions. The heat/mass transfer analogy is a semi-empirical method, therefore is limited to the existing correlations and their uncertainties. Our model does not use any empiricism and relies on the available solutions of laminar condensate film of pure vapor in predicting the liquid side heat transfer coefficient.

CHAPTER 3

Transient Vapor Diffusion

In this chapter, the transient buildup of the diffusion layer is considered. It is worth noting that the idea of species diffusion transience originated from nucleate boiling in which thermal diffusion transience plays an important role in the heat transfer improvement. By a way of analogy, one could think of species diffusion transience to have a similar effect in BFC.

3.1 Chapter objective

The objective of this chapter is to test the hypothesis that BFG transience starts with a high heat/mass transfer rate and then drops to a steady state value. It is also intended to know if sweeping the surface with high frequencies would have an improvement effect on the condensation process. This chapter motivates but is not the base to measuring the success of the next chapters.

3.2 Literature review

In 1959, Sparrow and Siegel [119] initiated the interest in theoretically deriving the transience of pure vapor condensation (Replicated in supplementary

material due to lack of online version of the resource). In their analysis, the integral form of the energy equation was solved by assuming the velocity and temperature profiles in the condensate film to be similar to the steady state case with the exception that the film thickness varies both with position and time. This simple analysis resulted in an expression of the film thickness, or heat transfer coefficient, as a function of position and time as

$$h(t) = h_{steady}(\frac{t_{steady}}{t})^{1/2} \tag{3.1a}$$

$$h_{steady} = \left[\frac{k_l^3(\rho_l - \rho_v)gh'_{fg}}{4\nu_l(T_o - T_w)x}\right]^{1/4} \tag{3.1b}$$

The time at which steady state heat transfer coefficient is reached was also inferred from the analysis as in Eq.3.2. Later, Chung (1963) [120] utilized the perturbation analysis resulting in a more generalized solution to Sparrow and Siegel's work.

$$t_{steady} = \left[\frac{h'_{fg}\rho_l\mu_l}{k_l g(T_o - T_w)(\rho_l - \rho_v)}x\right]^{1/2}\left(1 + \frac{1}{8}\frac{C_{p,l}(T_o - T_w)}{h'_{fg}}\right) \tag{3.2}$$

Due to the short duration to reach steady state, i.e. in the order of 1 second for most steam applications, the quasi-steady assumption was valid in the transient experimental work of Dhir (1975) [121]. Later in 1987, Reed et al. [122] compared the full solution of the boundary layer equations with the quasi-steady assumption for a sudden step in interfacial shear stress or wall temperature. Results showed that the quasi-steady assumption predicts well the full solution as far as the ratio of Jacob to Prandtl number is less than unity. As the ratio approaches unity, i.e. sensible heat becomes

significant, the quasi-steady assumption fails to predict the heat and mass transfer.

In 1976, Wilson [123] extended the work of Sparrow and Siegel to solve for the transient heat transfer coefficient of condensation surface with curvilinear coordinate. Heat transfer coefficients of flat plates, inclined cylinders, cones were obtained as a function of time and position. The problem of transient condensation in porous media was solved by other researchers [124, 125, 126]. A generalized analytical solution of the condensation transience over vertical plates was considered by Flik and Tien (1989) [127]. The model included the effect of transience of wall temperature, interfacial shear stress, as well as body force both in porous and non-porous media. The quasi-steady assumption was relaxed to encompass the effect of sensible heat effect. In most of the research work studying condensation transience, the method of characteristics is utilized to obtain the analytical solution of transient film thickness growth. Flik and Tien seem to be the first to relate this solution to a propagation of a kinematic wave from the boundary layer edge downstream. This is clear from the fact that the condensate film grows independent of position before reaching the steady state value, see Eq.3.1a. This suggests that the condensate film grows in a similar manner that a diffusion boundary grows in a semi-infinite medium.

Transient condensation on other geometrical configurations was studied, such as condensation on elliptical surfaces [128] and upward-facing horizontal surfaces [129]. Most of problems studying condensation in general and transience in specific, assume that the wall is isothermal. This assumption was relaxed by Trevino and Mendez [130]. In their work, they showed

using scaling analysis as well as numerical simulations that the thermal inertia of the wall is the controlling factor in most practical applications with transient condensation.

Recently, Balasubramaniam and Hasan (2015) [131] performed scaling analysis to predict the convection heat transfer coefficient for both transient and steady-state flat plate condensation. This work builds on all the previous work by showing first that the time to reach steady state is only a function of the steady state condensate film thickness. Then, they argue that by scaling analysis one could obtain an expression of the steady-state thickness to infer the transient film thickness. Their work agrees very well with other steady state analytical and numerical solutions.

The transience of condensation in the presence of NCG (BFC) has not been studied except in the work of Garimella and Christensen (1990)[132]. In their work, sudden injection of steam into an environmental chamber filled with air-vapor mixture was studied. Transient condensation on an Aluminum block was monitored visually as well as using thermocouples. Heat transfer was noticed to increase upon initial injection to values close to pure vapor condensation. Then, heat transfer drops to low values corresponding to those of the diffusion layer. No theoretical derivation of this phenomenon was proposed so far in the literature.

Observation of the transient growth of single droplets during BFC has been the course of several researchers [133, 134, 135, 136, 137, 138, 139, 140, 141, 142, 143, 144, 145]. In all the studied cases, the diffusion layer was at its steady state development. Figure 3.1 shows the concluded droplet growth regimes, based on all previous studies. First, droplets that nucleate

sufficiently far from each other, follow the famous $V \sim t^{3/2}$ rule. That is to say, the $t^{3/2}$ rule applies when the diffusion length of vapor through air is sufficiently smaller than the spacing between droplets. Second, as droplets grow, their individual diffusion layers overlap and the behaviour becomes similar to that of one-dimensional diffusion to a condensate layer of an effective thickness. Droplets in this regime follow a linear volume-time power law. Lastly, as droplets touch each other, they start coalescing and the volume growth behaves similar to the previous regime. However, in the coalescence regime the apparent mean diameter change linearly [133]. Because most of the previous cases monitored the mean diameter of droplets on surfaces, diameter change as $t^{1/2}$, $t^{1/3}$, and t^1 for the first, second and third regimes, respectively.

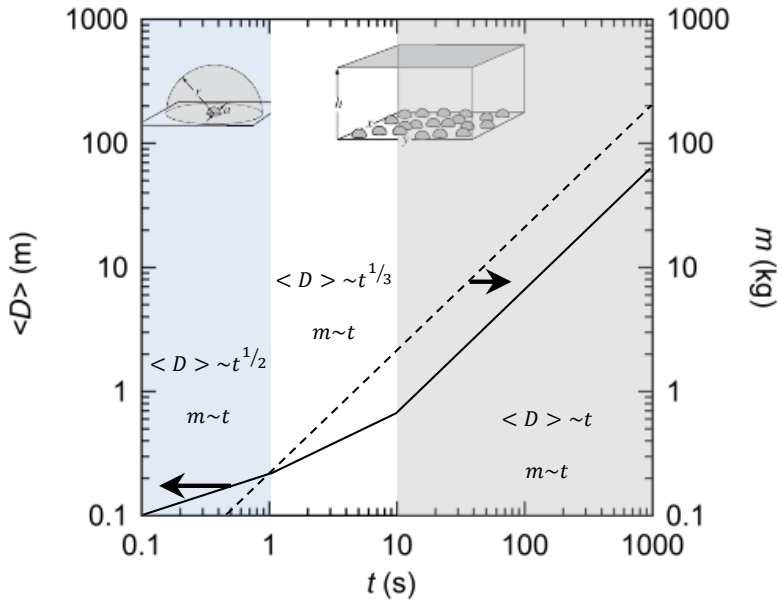

Figure 3.1: Regimes of droplet growth with time under steady state BFC; mean diameter and total mass change with time

However, despite the previous understanding of droplet growth regimes, the transience of the diffusion layer development has not been looked at. Further, as droplets of similar length scale to that of the thermal/species boundary layer thickness moves. An act of mixing or resetting the temperature or vapor concentration near the surface would take place. The boundary layer is expected to grow in a transient manner.

3.3 Theoretical model development

An approximate solution to the BFC transience is presented. The major simplifying assumption is that the condensation process is controlled by the diffusion of vapor through the diffusion layer. Therefore, limiting the solution to the NCG fractions that satisfy this assumption. With the above limit, we try to simplify the problem of suddenly exposing a surface to vapor-NCG mixture. The vapor-NCG mixture is initially at a temperature T_∞, vapor mass fraction ω_∞, and total system pressure P. The surface is suddenly cooled down to a temperature T_w that is below the saturation point (dew point) of the bulk vapor-NCG. As the condensation process starts, the condensate film thickness $\delta(t)$ has a zero value and is allowed to grow with time. Figure 3.2 shows the configuration of transient BFC on a solid surface.

We start by analyzing the temperature field in the solid side, given by the energy equation.

$$\frac{\partial T}{\partial t} = \alpha_s \frac{\partial^2 T}{\partial y'^2} \tag{3.3}$$

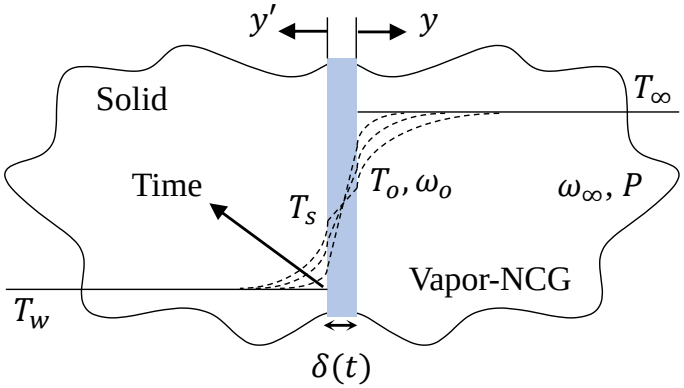

Figure 3.2: Configuration of the simplified model of the transient BFC.

with the following initial and boundary conditions.

$$T(y', 0) = T_w \tag{3.4a}$$

$$T(0, t) = T_s(t) \tag{3.4b}$$

$$T(\infty, t) = T_w \tag{3.4c}$$

If we relax the time dependency of the surface temperature, we obtain the well-known heat diffusion into a semi-infinite medium. The temperature distribution becomes

$$\frac{T(y', t) - T_s}{T_w - T_s} = erf(\frac{y'}{2\sqrt{\alpha_s t}}) \tag{3.5}$$

and the heat flux at the surface ($y' = 0$) can be expressed as

$$q = \frac{k_s}{\sqrt{\pi \alpha_s t}}(T_s - T_w) \tag{3.6}$$

We now turn to the vapor-NCG side by solving the species transport equation.

$$\frac{\partial \rho_v}{\partial t} = -\frac{dN_v}{dy} \tag{3.7}$$

The total mass flux of vapor can be written as

$$N_v = -D\frac{\partial \rho_v}{\partial y} + x_v(N_v + N_{NCG}) \tag{3.8}$$

Note that for the moment, we neglect the advective component and we compensate for it later using a suction effect factor ϕ, which becomes important for high condensation rates. We also note that the NCG total mass flux is neglected by assuming the advective flux towards the interface is balance by the outward diffusive flux due to the no-penetration condition. The species transport equation becomes

$$\frac{\partial \omega_v}{\partial t} = D\frac{\partial^2 \omega_v}{\partial y^2} \tag{3.9}$$

The initial and boundary conditions can be written as

$$\omega_v(y, 0) = \omega_\infty \tag{3.10a}$$

$$\omega_v(0, t) = \omega_o \tag{3.10b}$$

$$\omega_v(\infty, t) = \omega_\infty \tag{3.10c}$$

We again neglected the time dependence of the interfacial mass fraction. This is only permissible for (1) low interfacial temperature ($\omega_o << \omega_\infty$); or (2) time-invariant interfacial temperature. The solution of the vapor

fraction is therefore written as

$$\frac{\omega_v(y,t)-\omega_o}{\omega_\infty-\omega_o}=erf(\frac{y}{2\sqrt{Dt}}) \tag{3.11}$$

the total mass flux that follows is

$$\dot{m}''=-\phi\bar{\rho}D\frac{\omega_\infty-\omega_o}{\sqrt{\pi Dt}} \tag{3.12}$$

where the suction factor is

$$\phi=\frac{1-\omega_o}{\omega_o-\omega_\infty}ln(\frac{1-\omega_\infty}{1-\omega_o}) \tag{3.13}$$

Consequently, the total heat flux can be written as, assuming the thermal boundary layer is equivalent to the diffusion layer thickness ($Pr\sim Sc$)

$$q=\frac{1}{\sqrt{\pi Dt}}[\phi\bar{\rho}Dh_{fg}(\omega_\infty-\omega_o)+k_g(T_\infty-T_o)] \tag{3.14}$$

It is noted here that this equation looks analogous to the quenching and evaporative heat flux for nucleate boiling. Now we turn to the condensate film, in which heat conduction dominates the heat transfer. The film thickness can be derived by a simple mass balance at the condensation interface as

$$\frac{d\delta}{dt}=\frac{\phi\bar{\rho}}{\rho_l}\sqrt{\frac{D}{\pi t}}(\omega_\infty-\omega_o) \tag{3.15}$$

We assume that the thickness of the condensate film remains in such

a way that its thermal resistance is small, not necessarily negligible, compared to the solid or the diffusion layer thermal resistances. we can then integrate the above relation by ignoring the time dependency of interfacial mass fraction. The transient growth of the condensate film is written as

$$\delta(t) = 2\frac{\phi\bar{\rho}}{\rho_l}\sqrt{\frac{Dt}{\pi}}(\omega_\infty - \omega_o) \tag{3.16}$$

The heat flux through the condensate film is consequently written as

$$q = \frac{k_l\rho_l}{2\phi\bar{\rho}}\sqrt{\frac{\pi}{Dt}}\frac{T_o - T_s}{\omega_\infty - \omega_o} \tag{3.17}$$

Upon equating Eq.3.6, Eq.3.14, and Eq.3.17, we notice that the time term drops and an apparent interfacial temperature and mass fraction is obtained. This conclusion is in line with the famous interfacial temperature of two semi-infinite bodies in contact. The following equations can be easily derived

$$T_s = T_w + \sqrt{\frac{\alpha_s}{D}}\big[\frac{\phi\bar{\rho}Dh_{fg}}{k_s}(\omega_\infty - \omega_o) + \frac{k_g}{k_s}(T_\infty - T_o)\big] \tag{3.18a}$$

$$T_o = T_s + (T_s - T_w)(\omega_\infty - \omega_o)\frac{2k_s\phi\bar{\rho}}{\pi k_l\rho_l}\sqrt{\frac{D}{\alpha_s}} \tag{3.18b}$$

The mass fraction can be related to the temperature by the following relation

$$\omega_j = \left[1 + \frac{M_a}{M_v}\big(\frac{P}{P_{v,j}} - 1\big)\right]^{-1} \tag{3.19}$$

where the vapor pressure at a given temperature can be found from thermodynamic tables. Eq.3.18a and Eq. 3.18b are solved using EES to obtain the interfacial temperatures as well as the corresponding heat/mass transfer coefficients evolution with time. Following the equations above, the over-all heat/mass transfer coefficients can be defined as

$$U_H = \frac{q}{T_\infty - T_w} = U_o t^{-1/2} \tag{3.20}$$

$$U_M = \frac{\dot{m}''}{\bar{\rho}(\omega_\infty - \omega_o)} = \sqrt{\frac{D}{\pi}} t^{-1/2} \tag{3.21}$$

In this work, we look at both parameters in parallel. Eq. 3.21 suggests that the transient mass transfer coefficient can be obtained without prior knowledge of interfatial temperatures. In the next section, graphical results are presented for special cases to show the effect of different parameters on both transfer coefficients.

3.4 Results and Discussion

Figure 3.3 presents a typical transient behaviour of the over-all heat transfer coefficient for the case of saturated humid air at $T_\infty = 25^o$C, $T_w = 20^o$C, and $P = 1$atm. The figure shows that heat/mass transfer coefficients start by very high magnitudes which then drops to a steady state value within a specific time scale. The simple approximation performed in this section, is expected to work quite well within the very beginning of the transience, i.e. in the blue shaded area. The transition between the diffusion-limited

condensation to the steady state is controlled by both diffusion as well as advective forces, therefore, this model does not predict its behaviour. However, the time to reach steady state can be estimated, within reasonable uncertainty, by equating the resulting heat transfer coefficient with the steady-state expected value. As a rough estimation, the steady state heat transfer coefficient was obtained by A. Dehbi's correlation [118], discussed in supplementary material. The steady-state time scale is then calculated as

$$t_{steady} = \left(\frac{U_o}{U_{steady}}\right)^2 \tag{3.22}$$

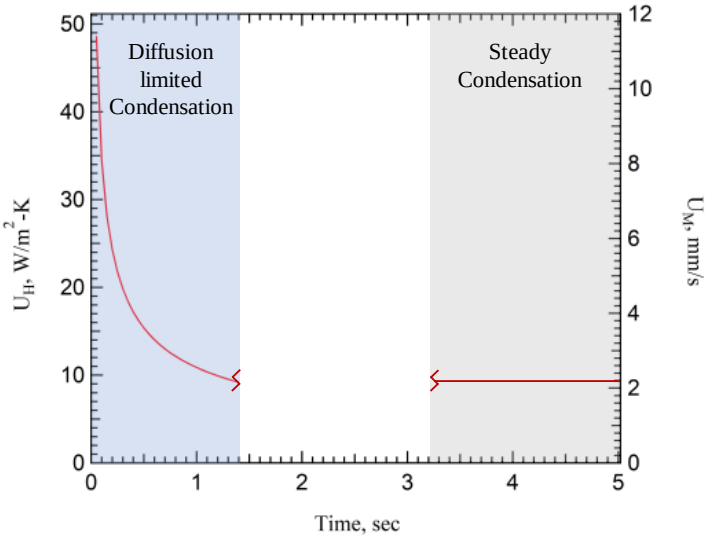

Figure 3.3: Typical transient behaviour of the over-all heat transfer coefficient for the case of saturated humid air at $T_\infty = 25^oC$, $T_W = 20^oC$, and $P = 1atm$.

Figure 3.4 shows the effect of the solid properties on the steady-state

time. As in the case of two semi-infinite bodies in contact, thermal effusivity/responsivity ($\varepsilon = \sqrt{\rho_s k_s C_{p,s}}$) is a lumping measure of the solid properties. Hence, we plot the steady-state time as a function of the solid's effusivity for the most practical materials, i.e. Copper, Aluminum, Brass, Stainless Steel, and Pyrex glass. No noticeable difference was found even with an order of magnitude difference in effusivity values. This suggests that the thermal resistance of the solid is very negligible compared to other resistances. This is an appreciated conclusion that is valid for such low vapor concentrations in this case. Other vapor concentrations can be solved using the developed model, however, this suffices for the purpose of this thesis.

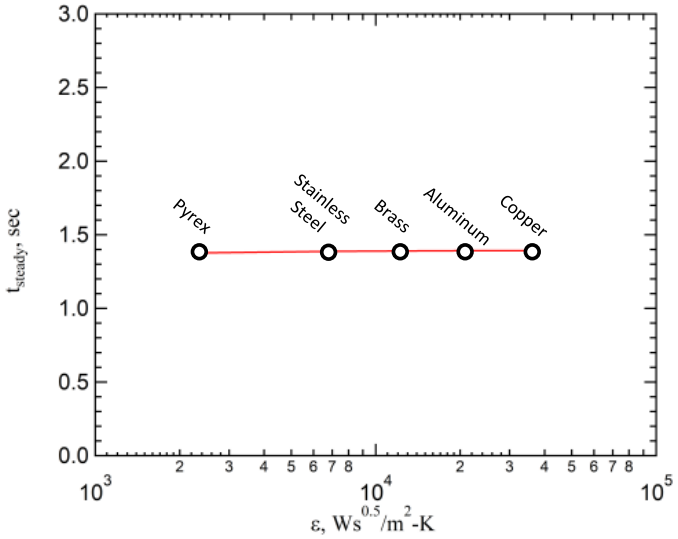

Figure 3.4: Effect of the solid properties on the steady-state time.

Figure 3.4 illustrates the effect of vapor mass fraction on the steady-state time at different ambient temperatures with a subcooling degree of 5 K. It

is very clear that as the vapor mass fraction increases, the duration of the transience becomes less. We also notice that the higher the ambient temperature, the less the duration of condensation transience. It is also clear that for highly pure vapor, the time scale for steady condensation becomes indistinguishable, i.e. the effect of ambient temperature is negligible. The shaded area in Figure 3.5 is for the sub-saturated air conditions (humid air). We note that for relatively low relative humidities, one expects high steady-state times, therefore, the possibility of increasing the heat/mass transfer by intermittently sweeping off the surface at frequencies lower than that of the steadiness frequencies ($1/t_{steady}$).

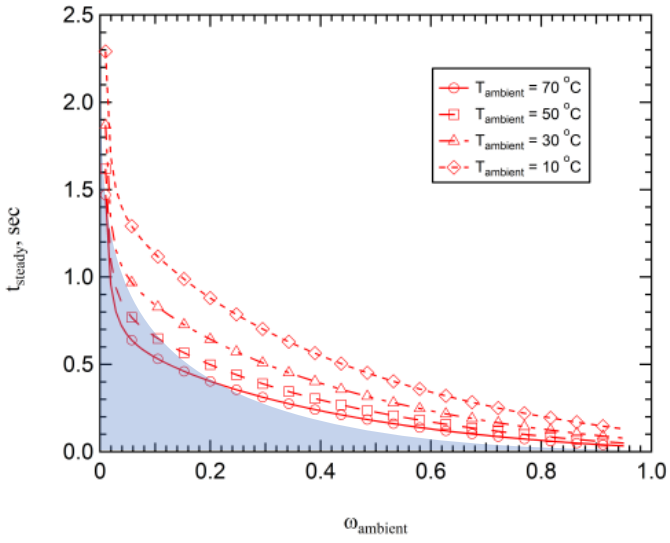

Figure 3.5: Effect of vapor mass fraction on the steady-state time at different ambient temperatures with a subcooling degree of 5 K (Shaded area is for humid air).

Figure 3.6 shows the effect of the subcooling degree at different ambient temperatures on the steady-state time for relative humidity of 100%. It is

clearly seen that the lower the subcooling levels, the higher the duration of transience. Frequency of sweeping the surface is in a manageable scale of 1 HZ which can be imposed by regular wipers or by small falling drops.

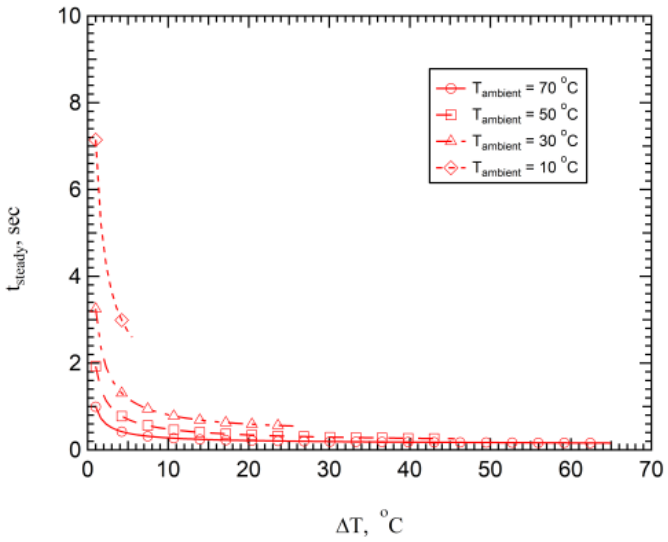

Figure 3.6: Effect of the subcooling degree at different ambient temperatures on the steady-state time for relative humidity of 100%.

Figure 3.7 shows the effect of subcooling level on the steady-state time at different ambient temperatures for pure vapor condensation. The figure was made using the work of Sparrow and Siegel [119] which was replicated in supplementary material. It is clear that the lower the subcooling of the condensation surface, the higher the duration of transience. This is similar to the case of BFC transience developed in our work. In contrast to BFC, pure vapor condensation is characterised by higher time scales. This, in turn, suggests that condensation can be improved with even lower sweeping frequencies compared to those of BFC.

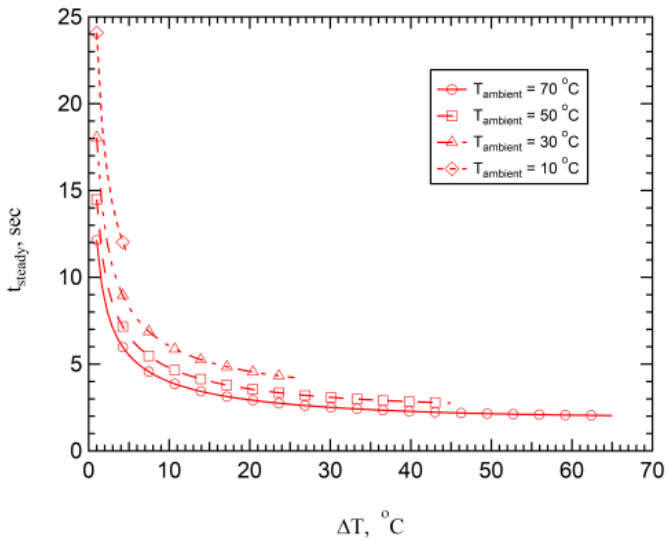

Figure 3.7: Effect of the subcooling degree at different ambient temperatures on the steady-state time for pure vapor condensation.

3.5 Summary and concluding remarks

In conclusion, we have developed an approximate model of BFC transience. We drew our model from analogy to nucleate boiling transience in which bubble departure acts as a mixing mechanism that improves heat transfer. Even though this model presents a rough approximation to the condensation transience, we expect similar qualitative behaviour with the studied parameters.To further study the condensation transience, we think that an experimental work is needed to validate such theory.

The direct analogy between the mixing mechanism of nucleate boiling and BFC can be deceiving. In nucleate boiling usually bubbles depart the surface and penetrate the thermal boundary layer. However, in most BFC processes, drops slide off vertical surfaces with a diameter in the order of ($\sim$ 1 mm), whereas diffusion layers are in the order of a few centimeters [144]. Therefore, no significant effect could be noticed by droplets sweeping off the surface in heat transfer. However, by thinning the diffusion layer to similar droplets length scales, one can gain some good mixing. Therefore, we propose in the next chapter to utilize jet impingement method as means of thinning the diffusion layer and making use of its shearing effects to improve droplets departing frequencies.

CHAPTER 4

Jet impingement condensation: Part I (Breath Figure Spot formation)

Based on the understanding of previous chapters, the diffusion boundary layer controls the condensation process in the existence of NCG. Actively thinning of the the diffusion layer should in principle improve the condensation rate significantly. We also noticed that by frequently disturbing the diffusion layer, the improved mixing should in theory increase the condensation rate. The active method introduced in the following chapters is utilizing jet impingement of humidified air onto a cooled surface. The jet impingement technique should in principle satisfy the two improvement mechanisms. In this chapter, we discuss the first observation noticed when a jet of humidified air comes in contact with the cooled surface. That is, the appearance of a Breath figure spot (or fogging spot).

4.1 Chapter objective

The objective of this chapter is to quantify experimentally the controlling parameters on the size of the BF spot. This is an important first step because the BF spot defines the area over which effective condensation

takes place. After experimentally studying the problem, we theoretically derive the governing relations.

4.2 Literature review

Condensation is a prevalent phenomenon in nature and industry, yet not fully explored. In nature, most living species rely evidently on condensed atmospheric vapor. Moreover, some plants and animals get their share of fresh water by evolutionary modified surfaces that enhance the condensation process, such as the Darkling beetles [66], and Sequoia Sempervirens [67]. Utilizing the phenomenon in numerous applications has been a course of scientific curiosity for a very long time, dating back to Aristotle (300 BC). In modern era, utilizing condensation has gone beyond large scale desalination plants to micro- and nano-scale lithography techniques [68]. In daily experience, people observe that upon breathing against a glass surface, white traces of condensate are generated. Upon a closer look under the microscope, such traces are composed of sessile droplets of a micron size [133]. External lighting scatters in all directions from dewed surfaces, therefore, they appear cloudy. However, old observations by Aitken [78] and Lord Rayleigh [146] discussed that flame-exposed glass does not show such cloudiness. In their discussion, they termed such behaviour as *breath figures* (BF) for obvious reasons. It is with our present understanding of surface energy effect that we are aware of wettability importance. Today, the phenomenon has been utilized in self assembly processes to produce honeycomb polymer patterns [147].

The presence of untraceable amounts of Non-condensable gases (NCG), such as air, in condensation processes has shown to dramatically reduce the condenser efficiency [95, 148]. The reason of this reduction is the accumulation of NCG on the liquid-vapor interface introducing a layer that is NCG-rich. The condensation rate becomes solely limited by the diffusion of vapor through this layer. Researchers have shown that heat transfer is thus limited by this layer's thermal resistance. Even though experimental studies have been successful in reducing NCG effect by means of vacuuming test chambers to environment [9], it is a highly impractical solution in large scale equipment. NCG can break through equipment via leak points, which is a problem of its own, or as a chemical reaction product of vapor interacting with the equipment material [82].

In efforts to mitigate the negative effect of NCG, other active techniques have been utilized, such as extended surfaces [84, 149]; direct contact between gas and cooling medium [88, 90, 150]; and different NCG carriers [92, 93]. Even though the former two solutions are promising, the latter seems to address the problem at its core, i.e. the effect of vapor diffusion through the diffusion layer which in result affects the heat and mass transfer. However, improvements from those techniques come with great material cost (former two techniques) or industrial impracticality (latter technique). Investigating the problem of NCG further shows that the solution lies within two possibilities; (1) increasing heat/mass transfer contact area (A); (2) increasing heat/mass transfer coefficient (h). The optimal solution should be obtained by maximizing the design parameter (hA) while minimizing the required cost.

Jet impingement of heat transfer fluids has shown a great potential in increasing the heat transfer coefficient for single phase [13, 14, 15, 16, 17, 18] as well as multi-phase applications [31, 32, 33, 34, 35, 36, 37]. Utilization of jet impingement to improve condensation heat transfer has not been tackled in literature thoroughly. Recently, on-demand impingement of pure steam jet has shown to alleviate the effect of NCG in accidental leakage [65, 151]. It has been shown that impinging a horizontal tube with pure steam increases the heat transfer by up to 77% compared to the case where NCG is present.

Impinging a cooled surface with air-vapor mixture has not been tackled in the literature, to the authors knowledge, especially in terms of improved condensation rates. Therefore, we present in this paper a first look at the problem. Initially, we pondered upon a sentence Lord Rayleigh wrote in 1911 about the generation of BF. '[as] the breath [was] led through a tube[, the] first deposit occurs very suddenly.'[80] Upon performing a simple experiment of breathing through a paper straw against a mirror, we noticed the sudden appearance of a condensate spot. The spot had a shape similar to the straw exit, a circle of defined boundaries. However, to our surprise, the condensate spot was weakly influenced by the strength (speed) of our breath and the distance between the mirror and the straw exit. This led us to build a simple experimental setup to control the mentioned variables. We show here that condensate spots are manifestations of a recovery concentration concept. The recovery concentration concept is analogous to the recovery or adiabatic-wall temperature investigated by Hollworth and Wilson [28, 29]. In their work, they showed that consistent results were obtained

upon basing Nusselt number correlations on the recovery temperature difference rather than the apparent temperature difference. In this work, we show that the recovery concentration manifests itself as a condensate spot which we call Breath Figure (BF) spot. This spot defines the effective area over which condensation of the jet's vapor takes place. Hence, we believe that quantifying this parameter is an essential step towards understanding condensation improvement by jet impingement.

4.3 Experimental method

In Figure 4.1, we show the experimental setup which consists of a humidifier, a flow system, and a condensation surface. Dry air was first directed into a humidifier tank which was filled with DI water at room temperature. The air entered from the bottom of the tank through several spargers to produce a humid air jet with the desired relative humidity. Because the water pool is at room temperature, the resulting humid air jet is at the same temperature, $T_\infty = T_j = 22\ ^oC$. The flow rate of the air was controlled by a flow-adjustment valve and was measured using a rotameter (Walfront, model no. LZQ-7). Flow rate ranging from 16.67 cm^3/s to 166.67 cm^3/s were used in our experiments. The jet of humidified air exited a tube of diameter, $D = 3$ mm, and a length, $L = 60$ mm, that was located at a varying standoff distance, $H = 1$ cm to 4.5 cm normal to the condensation surface. The jet impinged normally on the surface in an ambient relative humidity of $RH_\infty = 20$ %. The jet exited the tube in a highly humid condition, $RH_j = 95$ %. This was achieved by placing three spargers (manufactured

by Ferroday) to generate around 0.5 m air bubbles in the humidifier tank, only one sparger is shown in Figure 4.1 for illustration. The condensation surface was an aluminum substrate that was placed on the cold side of a Peltier plate with a thermally conductive paste. The Peltier plate was supplied with an environmental chamber and a PID temperature controller (KR$\ddot{U}$SS, DSA100). A range of substrate temperature, T_s = 22 ^{o}C to 5 ^{o}C, was tested to observe the BF spot incipience and size variation. The temperature of the cold side of the Peltier plate was recorded using an RTD element that was supplied with the PID temperature controller (KR$\ddot{U}$SS). An Infra-red (IR) camera (FLIR, A6753sc), and a flush-mounted k-type thermocouple (OMEGA, EXPP-K-20S-1000) were used to observe the condensation substrate temperature as well as the condensate droplets. The substrate temperatures measured by the three methods were in agreement within 1 ^{o}C. This rules out any possible heat transfer impedance of condensation due to surface thermal resistance. Systematic experiments were performed by first adjusting the flow to the desired jet Reynolds number $Re_j = 4Q/\pi\nu D$, where ν is the kinematic viscosity of humid air. At the desired standoff-to-diameter ratio (H/D), the jet exiting the tube was allowed to impinge on the surface without lowering surface temperature initially. The surface temperature was then lowered in steps of 0.5 ^{o}C from room temperature. At a certain surface temperature, we denote as the BF spot incipient temperature, BF spot starts to appear. As we lowered the surface temperature further, the expansion of the BF spot diameter was observed and recorded. The experimental parameters are summarized in Table 1 along with the colour/shape code of each data point. It is worth noting

Table 4.1: Colour/shape code of the experimental conditions for a total of 35 combinations of H/D and Re_j. Under each combination point, the temperature of the surface was varied from 22 ^{o}C to 5 ^{o}C and BF spot diameter was observed.

	$H/D = 3.33$	5	6.67	8.33	10	11.67	15
$Re_j = 500$							
1340	□	■	□	■	□	■	■
2230	△	▲	△	▲	△	▲	▲
3130	◊	♦	◊	♦	◊	♦	♦
4130	✧	✦	✧	✦	✧	✦	✦

that a regular camera (Teledyne Photometrics, CoolSnap HQ2) was used to observe the BF spots. The camera was inclined with a maximum of 10^o from the horizontal to obtain better visualization of the process. In Figure 4.2, we show a typical BF spot observation from a selected experiment. The image on the left shows a macroscopic view of the BF spot while the right image shows a microscopic view (3X). Due to light scattering from the condensate micro-droplets, a white trace was observed upon looking at the condensate deposit. Under the microscope, the BF spot boundary becomes very distinct as it separate between a wet inside and a dry outside regions. Within the BF spot drop-wise condensation is observed as seen in Figure 4.2 (right) and Video 1. In Video 1 (supplementary material), we show a time lapse of the growth of sessile droplets near the BF spot boundary. The sensor calibration and uncertainty analysis can be found in Appendix E.

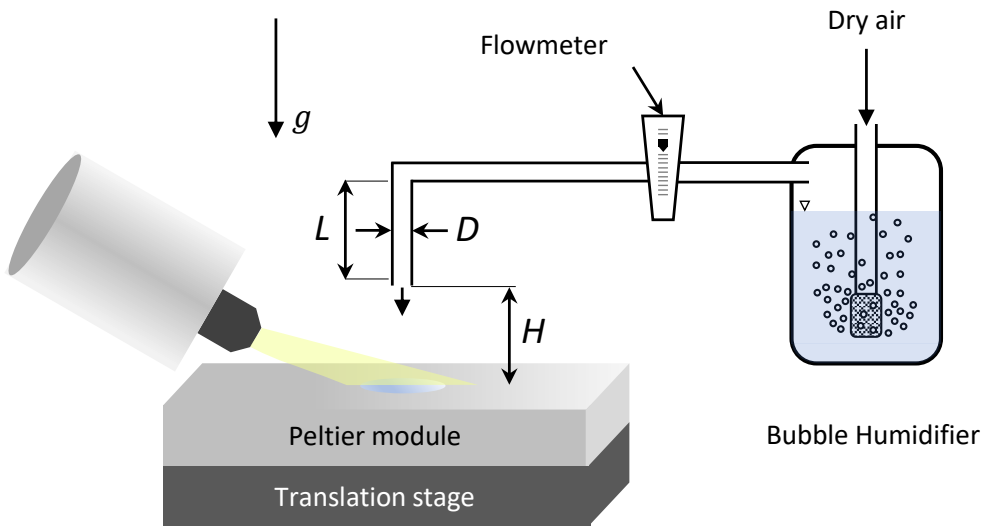

Figure 4.1: Schematics of a table-top set-up for observing the BF spots from a jet of humid air under varying parameters namely jet-surface temperature difference ($T_j - T_s$), jet exit Reynolds number ($Re_j = v_j D/\nu$), and standoff-to-diameter ratio (H/D).

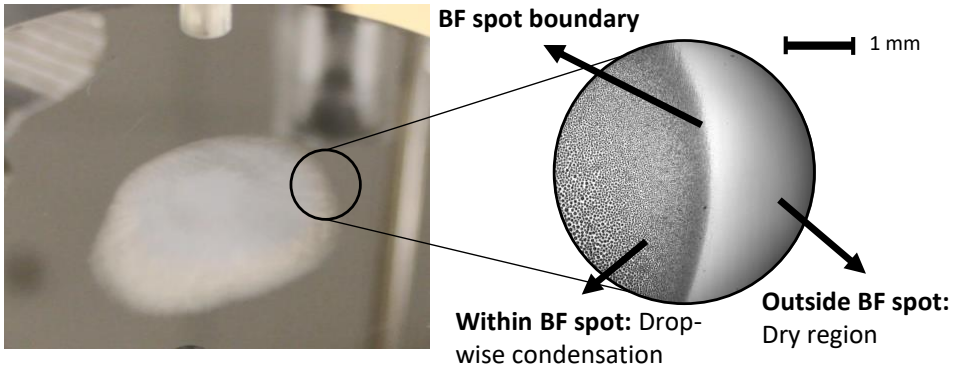

Figure 4.2: Typical BF spot formation taken by a regular camera (left image) and a low magnification microscope (right image).

4.4 Results and Discussion

Selected pictures at various experimental conditions are shown in Figure 4.3(a-c). In Figure 4.3(a), for fixed $T_j - T_s = 18$ ^{o}C and $H/D = 10$, the effect of the Reynolds number is shown. We observed that at the lowest Reynolds number, $Re_j = 500$, any obliqueness of the tube from the normal to the surface is characterized by a "tailed" BF spot. The tail is directed opposite to the angle of obliqueness. Adjusting the impingement angle to eliminate the tail served as an indication of a 90^o-angle impingement in our experiments. It should be noted that the tail is absent for higher Reynolds numbers for small inclination of the tube. It is worth mentioning that for $1000 < Re_j < 3000$ jets are in a transition regime whereas jets become fully turbulent for $Re_j > 3000$ [15]. Therefore, The existence of a tailed BF spot might be due to the laminar behaviour of the jet. Additionally, the circularity of the BF spot is clear for high Reynolds number. The effect of standoff-to-diameter ratio for $T_j - T_s = 18$ ^{o}C and $Re_j = 3130$ is depicted in Figure 4.3(b). We observed that BF spot size is invariant with H/D at least for the tested range of 3.33 to 15. In Figure 4.3(c), we present the effect of jet-surface temperature difference for $Re_j = 3130$ and $H/D = 8.33$. As the temperature of the surface falls below the dew point of the jet center, the BF spot appears. The point of BF spot inception occurs at lower surface temperature as H/D increases. Also, further decrease in the surface temperature corresponds to an increase in the BF spot diameter. The BF spot diameter keeps increasing with decreasing the surface temperature to the point at which atmospheric vapor start condensing. Below the atmospheric dew point, BF spot becomes indistinguishable from sessile

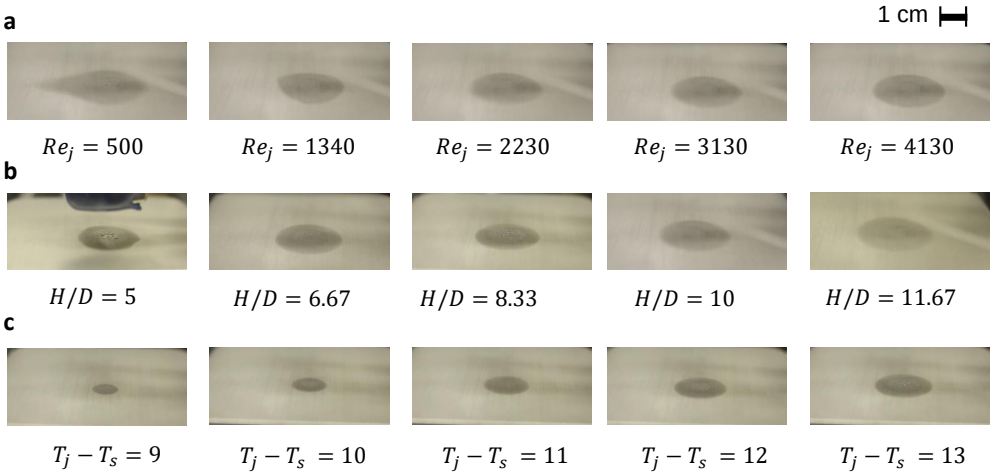

Figure 4.3: Selected pictures of the BF spots at various conditions. **a.** BF spots at varying jet Reynolds number. The selected pictures are for the case of $T_j - T_s = 18\ ^o$C and $H/D = 10$. **b.** BF spots at different standoff-to-diameter ratios. The selected pictures are for the case of $T_j - T_s = 18\ ^o$C and $Re_j = 3130$. **c.** BF spots at different jet-surface temperature differences. The selected pictures are for the case of $H/D = 8.33$ and $Re_j = 3130$.

droplets that appear on the entire surface.

To quantify that behaviour, vapor concentration distribution is inferred from the temperature measurements and BF spot size. At any experimental run, the vapor mass fraction at the boundaries of the BF spot was obtained as [152]

$$\frac{1}{\omega_s} = 1 + \frac{M_a}{M_v}\left(\frac{P_\infty}{P_v} - 1\right) \tag{4.1}$$

where M_a, M_v, P_∞, and P_v, are molecular weight of air, molecular weight of water, ambient pressure, and water vapor pressure at the surface temperature, respectively. In Figure 4.4, we show the distribution of dimensionless vapor mass fraction $(\omega_j - \omega_\infty)/(\omega_{max} - \omega_\infty)$ as a function of

normalized BF spot diameter D_{BF}/D at different experimental conditions. The maximum mass fraction is obtained at the inception of BF spot. It should be noted that only results of turbulent jets ($Re_j > 1000$) are shown in Figure 4.4 (The full range of Reynolds number is plotted in Figure S.1). First, It is clear that at any H/D, the mass fraction distribution is weakly influenced by Reynolds number. The lowest H/D value shows a steeper drop of vapor mass fraction while increasing H/D has a flattening effect. Further, for $H/D > 5$, we observe that even standoff distance has a weak influence on the distribution of vapor mass fraction. It is worth noting that for $H/D < 5$, the free jet is still in the developing region [5]. Therefore, the behaviour becomes similar to a confined jet [153]. In Figure 4.5, we plot the maximum vapor mass fraction as a function of both H/D and Re_j. The vapor mass fraction is normalized with the jet excess mass fraction ($\omega_j - \omega_\infty$). We recognize that the laminar jet has a constant maximum vapor concentration for $H/D < 11.67$, which suggests that laminar jets lose less vapor content into the ambience compared to their turbulent counterparts. This is probably due to the improved mixing of the latter which helps in dissipating vapor to ambience. However, for turbulent jets, the maximum mass fractions seem to decrease monotonically with H/D value.

The BF spot formation can be described using the following simple thought experiment. Consider a surface that is in thermal equilibrium with the jet and the ambience with the jet containing a higher vapor concentration than the ambience. After the humid jet exits the tube, vapor diffuses into the ambience before impinging on the surface. The concentration profile of the jet is therefore changed from being uniform to having a Gaussian

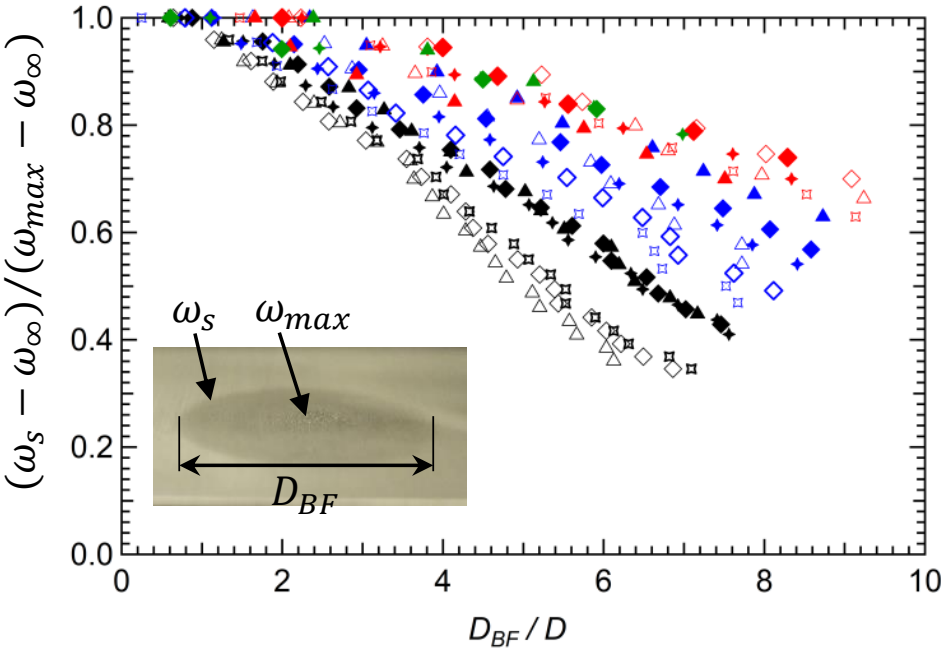

Figure 4.4: Dimensionless concentration distribution on the surface as a function of dimensionless radial distance (or BF spot diameter to tube diameter ratio) (D_{BF}/D). Colour/shape code correspond to Table I.

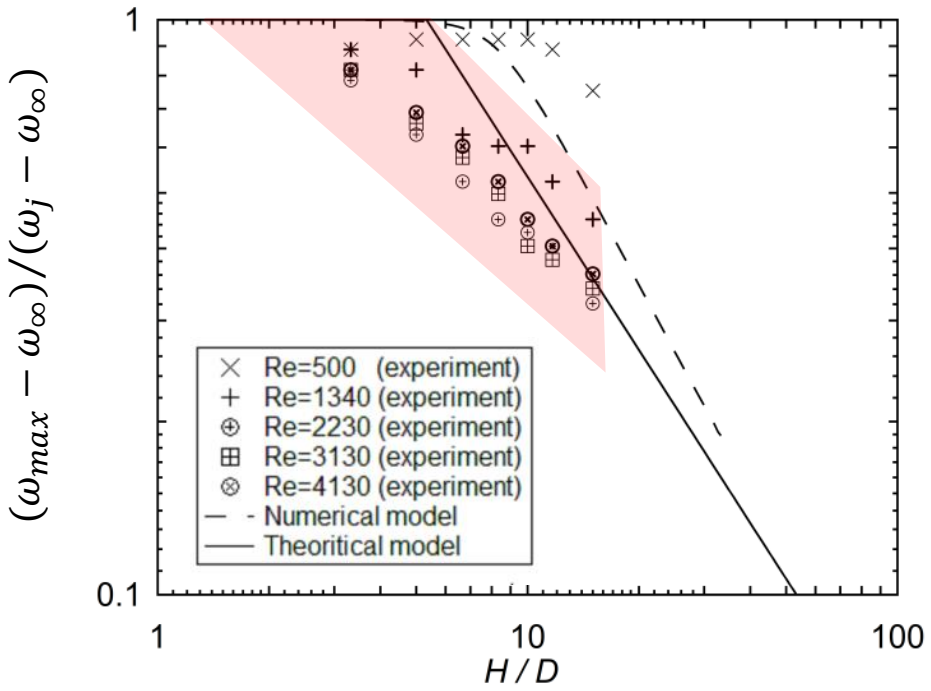

Figure 4.5: Dimensionless maximum concentration as a function of H/D and Re_j. The maximum concentration is obtained at the inception of BF spot point as depicted in Figure 4.4 and Eq. (4.1). The red-shaded region correspond to the experimental uncertainty in measurements.

distribution as shown in several analytical solutions [154, 155]. The value of the maximum concentration and width of the diffusing jet depends on the distance travelled by the jet as well as ambient thermal and flow conditions. Upon jet impingement, a significant mixing occurs that allows dissipation of the high vapor concentration near the surface. Without reducing the surface temperature, the vapor concentration at the wall has a decaying distribution from a maximum value at the center of the impingement area to a minimum value equivalent to that of the ambience further away. Due to the variation of the vapor mass fraction at the surface, there is an equivalent saturation temperature (dew point) variation with radial direction. For a constant surface temperature (T_s), When T_s falls below the dew point at a given radial location, condensation will take place from the center up to that radial circumference, hence, a BF spot forms.

In Supplementary material, we present a numerical model that employs our understanding of recovery concentration. The jet impingement on a wall is reduced to a two-dimensional axisymmetric problem. The jet issuing from the tube has fully developed velocity profile and uniform temperature, and concentration profiles. The continuity, momentum, energy and species equations are solved over the jet vicinity region. Because of the importance of accounting for turbulence in jet dynamics, standard $k-\omega$ formulation is usually preferred [156, 157]. A finite volume solver was utilized to obtain the solution of the governing equations in the desired domain. Solutions of the Re_j and H/D combinations were obtained both for free jet and wall obstructed cases. Further details and insights could be found in Supplementary material.

We first model theoretically the vapor concentration in the impingement region ($D_{BF}/D < 5$). Most importantly, we focus on the maximum concentration value which seems to be influenced significantly by the standoff distance rather than Reynolds number according to Figure 4.5. To obtain a scaling analysis of such behaviour, we resort to the visual observations obtained from our numerical simulations in Figure S.3 and Figure S.4. The maximum concentration of a jet impinging on wall corresponds to its counterpart in a free unbounded jet at the same standoff-to-diameter ratio. In other words, the maximum vapor concentration is not affected by the impingement action. Therefore, we derive the theoretical curve in Figure 4.5 by using a free unbounded jet solution. Using a control volume at the tube exit to an arbitrary axial location in a free unbounded jet, momentum conservation can be written as

$$\rho v_j^2 \frac{\pi D^2}{4} = 2\pi\rho \int_0^\infty v^2 r dr \tag{4.2}$$

where ρ is the overall mixture density and v_j is the mean velocity of the jet. By assuming that the overall mixture density does not vary greatly, which is valid for such low vapor concentrations. According to previous studies, in the developed region ($H/D > 5$), the velocity profile has a Gaussian distribution form. Reichart gave the following relation at any given axial location (H) [158, 159]

$$v = v_{max} \exp[-a_v \left(\frac{r}{H}\right)^2] \tag{4.3}$$

where a_v is an empirical constant that depends on the tube exit geome-

try. Substituting Eq. (4.3) into Eq. (4.2), we get the maximum velocity as $v_{max}/v_j = \sqrt{a_v/2}(D/H)$. If we apply vapor species conservation over the same control volume, we have

$$\rho v_j(\omega_j - \omega_\infty)\frac{\pi D^2}{4} = 2\pi\rho\int_0^\infty v(\omega - \omega_\infty)rdr \tag{4.4}$$

where ω_i is the vapor mass fraction evaluated at the surface temperature and saturated conditions, and ω_∞ is the vapor mass fraction evaluated at the ambient temperature and relative humidity. In general, the concentration profile of the jet has a Gaussian distribution as well. Therefore, one can write the concentration profile as

$$(\omega - \omega_\infty) = (\omega_{max} - \omega_\infty)\exp[-a_\omega\left(\frac{r}{H}\right)^2] \tag{4.5}$$

where a_ω is an empirical constant different from that associated with the velocity profile. Substituting Eq. (4.3) and Eq. (4.5) into Eq. (4.4) and combining the constants yield

$$\frac{\omega_{max} - \omega_\infty}{\omega_j - \omega_\infty} = \frac{a_v + a_\omega}{\sqrt{2a_v}}\frac{D}{H} \tag{4.6}$$

where the leading constant $(a_v + a_\omega)/\sqrt{2a_v}$ is an empirical value that depends on the tube-exit type and experimental conditions. In table S.1, we present the experimental values of the leading constant for the different cases studied. Data of over 105 experiments show to be well represented by $(a_v + a_\omega)/\sqrt{2a_v} = 5.3 \pm 2$. Eq. (4.6) is depicted in Figure 4.5 along with the numerical model result. The theoretical model seem to capture maximum

concentration behaviour within the experimental uncertainty. On the other hand, a small deviation is observed for the numerical simulation. Even though, the overall behaviour is captured by both methods, we believe that both methods have their limitations. The theoretical model assumes velocity and concentration to possess Gaussian distributions, however, several other profiles, such as a polynomial [160] could be used. The numerical simulation utilized the standard $k-\omega$ model which is highly sensitive to the inlet and boundary conditions. However, given the simplistic approach of predicting the general behaviour, both methods offer excellent predictive tools.

Next, we use an analytical approach for ($D_{BF}/D > 5$) to analyse the BF spot boundary in the wall-jet region. Because of the sudden deposition, we can assume that BF spots are analogous to the concept of adiabatic wall or recovery temperature. Recovery temperature has been discussed in the context of heat transfer of impinging jets [28, 29, 30] as well as high Mach number flows [161, 162]. The importance of such parameter emerged from the mismatch between surface, jet and ambient temperatures which necessitates *entrainment*. By the same token, we think BF spots are manifestations of a *recovery concentration* concept that has not been discussed in literature as to the author's knowledge. Here we present a theoretical model of the recovery concentration.

In Figure 4.6, we present a schematic of an imaginary conduit starting from the tube exit and covering the impinged surface at an arbitrary radial location (r). At the bounding surfaces of the conduit, there is negligible mass transfer or negligible vapor mass concentration gradient. Applying a

species mass conservation between the tube exit and the radial location on the surface gives

$$\rho\frac{\pi D^2}{4}v(\omega_j-\omega_\infty)=\rho\int_0^\delta v(\omega-\omega_\infty)(2\pi r)dz \tag{4.7}$$

where δ is the total thickness of the boundary layer. It has been recognized by several researchers that upon normalizing the velocity profile with its local maximum value, all velocity profiles in the wall jet region simplifies to $v/v_o \sim f(z/\delta)$ [28]. Whereas normalizing the excess local vapor mass fraction with the excess recovery concentration should result in a self-similar solution. Here we assume that, in the wall jet region, the non-dimensional vapor mass fraction is $\sim f(z/\delta)$. Upon performing the normalization, we obtain

$$r\delta(\omega_r-\omega_\infty)v_o\int_0^1\left(\frac{v}{v_o}\right)\left(\frac{\omega-\omega_\infty}{\omega_r-\omega_\infty}\right)\frac{dz}{\delta}=\frac{D^2v_j}{8}(\omega_j-\omega_\infty) \tag{4.8}$$

For self-similar velocity and concentration profiles, the entire integral is assume to be a constant (C_1). Simplifying the previous relation gives

$$\frac{\omega_r-\omega_\infty}{\omega_j-\omega_\infty}=\frac{1}{8C_1}\left(\frac{v_j}{v_o}\right)\left(\frac{D}{r}\right)\left(\frac{D}{\delta}\right) \tag{4.9}$$

According to the several studies of turbulent jets [163, 164, 28], the normalization thickness and velocity in the wall jet region can be correlated as

$$\frac{v_o}{v_j}=C_2\left(\frac{H}{D}\right)^{0.1}\left(\frac{r}{D}\right)^{-1.1} \tag{4.10}$$

$$\frac{\delta}{D} = C_3\left(\frac{r}{D}\right) \tag{4.11}$$

Substituting Eq. (4.10) and Eq. (4.11) into Eq. (4.9) and combining the constants result in the following conclusion

$$\frac{\omega_r - \omega_\infty}{\omega_j - \omega_\infty} = C_4\left(\frac{H}{D}\right)^{-0.1}\left(\frac{r}{D}\right)^{-0.9} \tag{4.12}$$

where $C_4 = 1/(8C_1C_2C_3)$ is a constant that depends on the tube-exit type and experimental conditions. Eq. 4.12 shows a weak effect of standoff-to-diameter ratio with a power law of -0.1. Acceptable results within the experimental uncertainty could also be obtained if the effect of H/D is absorbed into the leading constant. Figure 4.7 shows all the experimental data along with the theoretical curve given by Eq. (4.12). The recovery concentration is independent of the jet Reynolds number at any given standoff-to-diameter ratio. Furthermore, there is no clear effect of standoff-to-diameter ratio in the wall-jet region. This is clear as all data points collapse on a universal curve in that region. The effect of standoff distance is noticed from Eq. (4.12) to be very minimal which is in accord to our observation in Figure 4.3 and Figure 4.4. Table S.1 presents the curve fitting constant obtained for the experimental data points. Data of over 1890 experiments show to be well represented by a leading constant ($C_4 = 1.12 \pm 0.14$) in Eq. (4.12). We also showed mathematically that the jet velocity has no effect on the value of maximum vapor concentration. Eq. (4.6) is depicted in Figure 4.7 where the effect of H/D is pronounced at the center of the impingement region. The BF spot dimension between the center of the

impingement region to the wall jet region varies smoothly in a transition region.

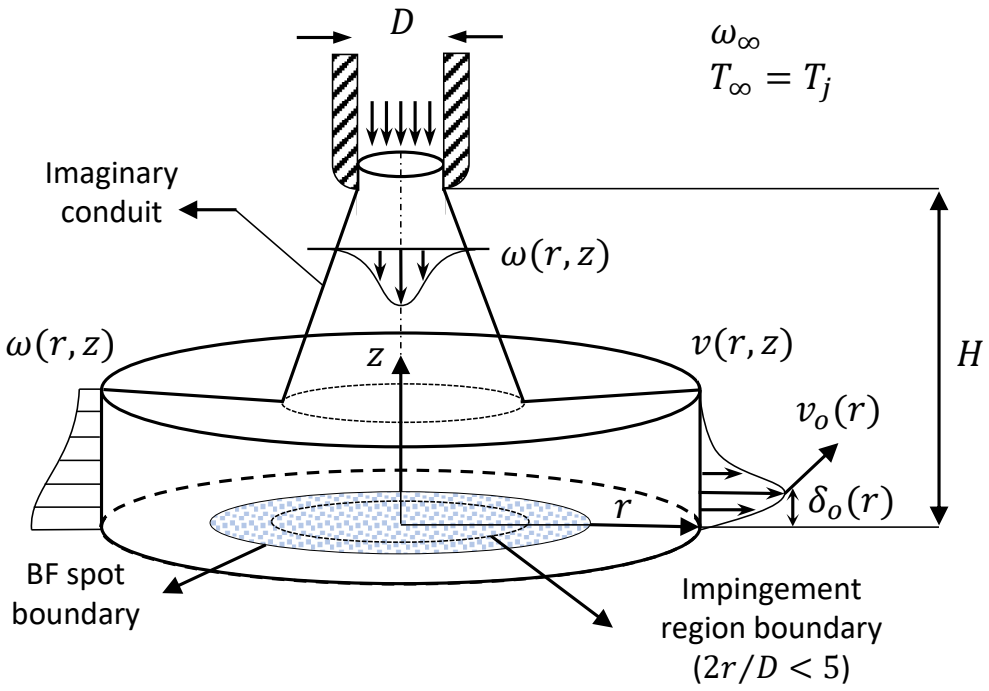

Figure 4.6: Control volume approach for analysing humid air jet impingement. Schematic of the imaginary conduit over which vapor mass is conserved. Derivations of Eq. (4.6) and Eq. (4.12) depend on the understanding of this schematic. As the humid air exits the tube, vapor starts to diffuse into the ambience. However, the imaginary conduit boundary is located at a radial location where the gradient of vapor concentration is nearly zero, i.e. negligible diffusion is present. As the stream of vapor-air impinges on the surface, flow changes direction from y-direction to r-direction. The velocity and vapor concentration profiles at an arbitrary radial location away from the impingement region are depicted.

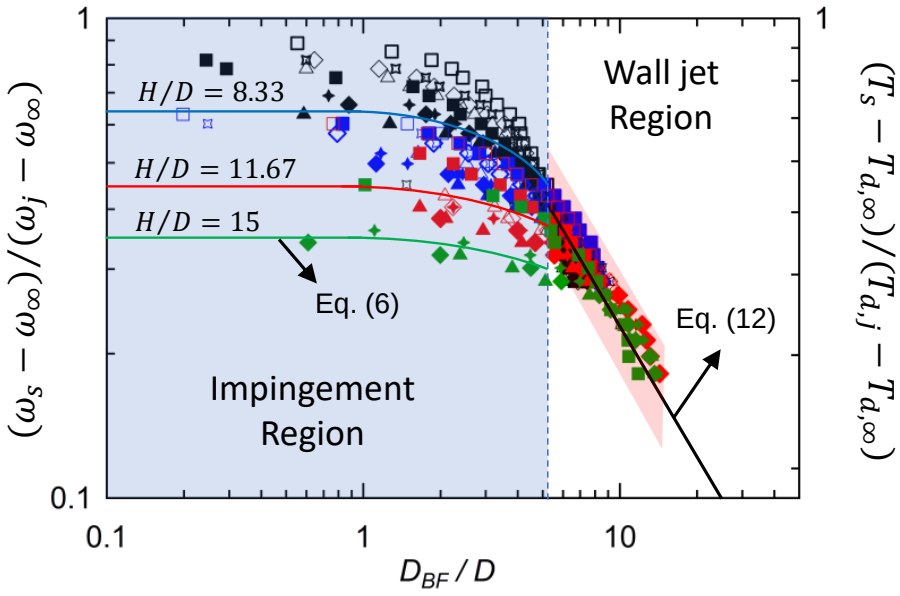

Figure 4.7: Recovery concentration distribution. A plot of nondimensional vapor mass fraction and nondimensional surface dew temperature with respect to the extent of BF spot circle. The plot is split into two regions; impingement region ($D_{BF}/D < 5$ - blue-shaded region); and wall jet region ($D_{BF}/D > 5$). The derivation of Eq. (4.6) is valid in the impingement region while Eq. (4.12) is valid in the wall jet region. The red-shaded region correspond to the experimental uncertainty in measurements.

4.5 Summary and concluding remarks

In conclusion, measurements were made of an isothermal humid air jet exiting a tube into a stagnant room-condition air. Because the humid air jet has higher vapor content than the environment, vapor diffuses from the former to the latter. It has been shown that humid laminar jets lose less vapor content as they travel into the environment compared to the turbulent jets because of the improved mixing mechanism of the latter. This was clear by observing the maximum concentration of the jet as it travel into an ambient air. On the other hand, for jets with $1340 \leq Re \leq 4130$, we showed experimentally that the vapor content diffusion into the environment is independent of the jet's velocity magnitude. The maximum vapor concentration becomes a function of standoff distance only beyond the developing free jet region. We also showed for the first time that visible BF spots are manifestations of a new concept of a recovery concentration. We drew our analogy from the recovery temperature concept in heat transfer applications. The newly found concept is very important in studying species mass transfer due to jet impingement in general. Our findings show that BF spot is the area over which effective condensation takes place. Quantification of BF spot size is essential in optimizing the surface area of condensers as well as their temperatures to obtain effective condensation rates. We also predicted theoretically the concentration distribution on a surface exposed to humid air jet impingement. Eq. (4.6) and Eq. (4.12) present important conclusions with which concentration distributions on an impinged wall are found. We believe that this study is of great importance to optimize jet impingement heat and mass transfer rates. Several applications could utilize

this work's findings, such as in textile drying, dehumidification technologies or exhaled breath condensate (EBC) technology [165, 166].

CHAPTER 5

Jet Impingement Condensation: Part II (Droplet Mobility and Condensation Rate Evaluation)

The previous chapter investigated the area over which effective condensation takes place (BF spot). Inside the BF spot, dropwise condensation is the dominant mode of condensation even for hydrophilic surfaces. Once condensate droplets reach certain sizes, the shedding capability of jet impingement mobilizes them. The interesting mobility and growth of droplets is discussed further in this chapter.

5.1 Chapter objective

The objective of this chapter is to visualize the droplet motion at various experimental conditions namely jet velocity and surface wettability. Additionally, this chapter sheds some light on the condensation rates under the given conditions. Lastly, we trace a single droplet from the onset of departure to its final location away from the jet source.

5.2 Literature review

Condensation is a perplexing problem to fully uncover, yet, its applications play crucial roles in industrial development [68, 167, 168, 169, 170]. In order to promote more efficient applications, improving the condensation process has been the focus of many scientific research. Various condensation heat transfer augmentation techniques have been utilized, these techniques can be classified to; Passive [6, 69, 70, 71, 72, 73, 74]; active [171, 172]; and compound techniques. Unlike passive, active techniques require external forces to be applied either on the heat transfer surface or working fluid. Unsurprisingly, passive techniques have caught major attention of the scientific community because of their easier implementation in existing industrial applications. Contrarily, active techniques require additional equipment to exert the required forces to improve the heat and mass transfer efficiencies. This, in turn, means higher capital expenditures and operating expenses. Observing the state-of-the-art literature, the most trending technology is altering surface wettability [6]. However, it is still under development due to the chemical and physical durability issues of coating techniques [75, 6, 76, 77, 173].

Major research efforts have been focused on developing durable and cost effective coating techniques to promote drop-wise condensation (DWC) and mitigate the formation condensate films on surfaces, i.e. film-wise condensation (FWC). DWC has shown to possess at least an order of magnitude improved heat transfer coefficient compared to FWC [174]. This improvement is highly dependant on the frequency of droplet shedding

on surfaces. Droplets shedding has been achieved primarily by gravity assistance [9, 8, 175], droplet jumping [176, 172, 177, 178], drag force [179, 180, 181, 182, 183], or by capillary driven movement [184, 185]. It has been widely accepted that droplets of diameters below 20 micron contribute about 80% of the total heat transfer to the surface [186]. This implies that removing droplets of higher diameters is preferred, otherwise, their higher thermal resistance and coverage area will impede further condensation. Combining superhydrophobic surfaces and a shedding mechanism might seem to be the obvious solution for achieving efficient DWC. However, superhydrophobic surfaces are characterized by their low nucleation site density for condensation and higher droplet thermal resistance, therefore presenting a conflicting purpose [173]. Therefore, there is a high demand to sustain efficient DWC with innovative techniques that go beyond surface modifications.

An extremely important concern most passive augmentation techniques has not resolved is the degradation of heat/mass transfer coefficients caused by the existence of non-condensable gases (NCG) [173, 187]. Experimentally, degassing prior to running condensers has been successful in alleviating the effect of NCG [9, 173]. Despite the experimental convenience of such method, it is a highly impractical solution in large scale condensers. NCG can find their way into condensers via leak points or as chemical reaction products of vapor interacting with the equipment material [82]. On another front, the emerging humidification-dehumidification (HDH) desalination technology relies heavily on NCG as carrier gases. The premise of this technology is the low energy required to humidify air compared to

other thermal desalination counterparts [188, 189, 190]. Even though it is evident that the dehumidifier in HDH technology is highly inefficient, the heat transfer deficit has been compensated by three alternatives. They are; (1) extended contact area [83, 84, 85, 149] (2) direct contact between humid air and cooling medium [86, 87, 88, 89, 90, 91, 150]; and (3) different NCG carrier [92, 93]. Even though the former two solutions are promising, the latter seems to address the problem at its core, i.e. the effect of vapor diffusion coefficient thus condensation rate. Therefore, there is a pressing demand on working out a solution to enhance condensation with the presence of NCG.

To overcome the problem of sustaining efficient condensation without requiring unstable and expensive surface modifications, an active method needs to be designed. The active augmentation method needs to mitigate the negative effect of NCG while maintaining practical applicability. Several active methods have been tried, such as fluid/surface vibration [191, 192, 193, 194], electrohydrodynamic effects [195, 196, 197, 172, 198], and rotating surfaces [199, 200, 201], to name a few. The general goal of the different active methods is to prevent the condensate from growing by actively sweeping it off the surface. While this has shown to be effective, surface wettability is still important to generate DWC rather than FWC. In addition, the effect of NCG is still not resolved with the aforementioned methods. Here, we investigate utilizing jet impingement as an active method for providing DWC on surfaces with varying surface wettability. The jet impingement method not only helps with shedding droplets on wettable surfaces but also helps with mitigating the effect of NCG. The uti-

lization of jet impingement in heat and mass transfer applications has been studied in heating/cooling for single phase flow [15, 17], drying application [36], nucleate boiling [38], and spray cooling [52]. Recently, on-demand impingement of pure steam jet has shown to alleviate the effect of NCG in accidental leakage [65, 151].

To sustain efficient DWC without requiring unstable and expensive surface modifications, we present a novel 'continuous drop-wise condensation' (CDC) as a method to tune the maximum droplet size on modified and unmodified condensation surfaces. We also present CDC as a method to improve condensation with NCG by means of thinning the diffusion boundary layer and therefore reducing the resistance to diffusion. Impinging a modified or unmodified surface with a jet of humid air or pure vapor results not only in a higher heat and mass transfer coefficients but provides an excellent droplet shedding mechanism (Fig.5.1). Controlling the diameter of droplet shedding is made possible by tuning the jet parameters, e.g. exiting diameter, velocity, and standoff distance. To provide evidence of the proposed mechanism, several experiments were conducted under various jet parameters as well as different surfaces with a wide range of advancing contact angles, i.e. $\theta_A = 70^o$ - 160^o. In addition, we utilize our experimental observation to show that CDC provides over 6-fold improvement in compactness factor compared to state-of-the-art dehumidifiers. Furthermore, using an analytical model, we show that CDC provides enhancement in heat flux of over 300% compared to gravity-assisted shedding mechanisms. This is made possible by the improved mechanism of tuning the maximum droplet size compared to state-of-the-art techniques. Finally, We provide

a theoretical framework for understanding droplet dynamics by comparing the different forces acting on a droplet during jet impingement.

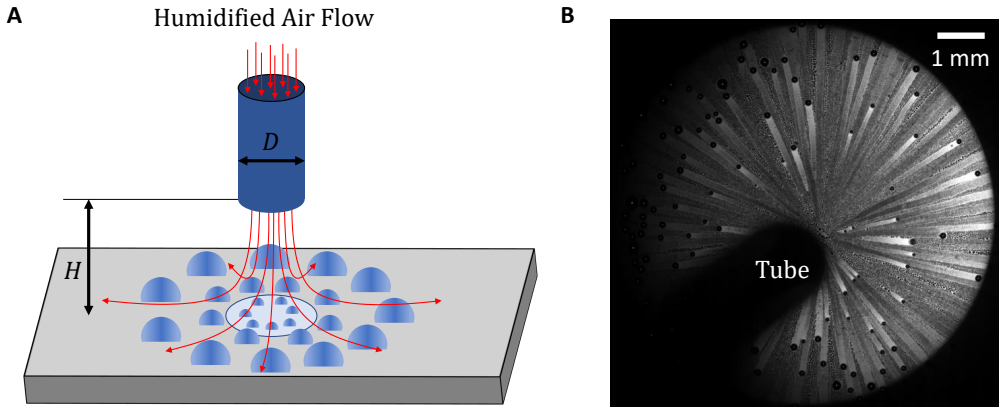

Figure 5.1: Utilizing Jet impingement as a means of compact continuous drop-wise condensation (CDC). **A.** A schematic of CDC illustrating the condensation mechanism utilizing jet impingement as a means of enhanced condensation rate and droplet shedding. pure vapor or Humidified-air jet exits a tube of diameter (D) at a standoff distance (H) with a mean velocity (v_j). **B.** A still Microscopic image of CDC under a selected experimental condition ($D = 0.047$ inches, $H = 0.32$ inches and $Re_j = 3600$). Complete description of experimental set up is presented in methods section and supplementary material Fig.D.1

5.3 Experimental methods

5.3.1 Surface preparation and characterization

Commercially available Silicon wafers (Techgophers) were used as the base condensation surfaces. In this work, we utilized five surface modifications namely (1) Hydrophilic Si surface, (2) hydrophilic micro-structured Si surface, and (3) hydrophobic silanized Si surface (4) superhydrophobic micro-structured Si surface, and (5) superhydrophobic spray-coated Si surface. Silicon wafers of similar thicknesses were used in this work to provide similar thermal resistances over the different tests. Checking the temperature distribution on the Si surfaces shows that their thermal resistance is quite negligible compared to the vapor-NCG side dominating thermal resistance. Before each experiment, the surfaces were cleaned with acetone (J.T.Baker), isopropanol (J.T.Baker), ethanol (J.T.Baker) and DI water and dried with filtered nitrogen stream. Experiments were done immediately after the cleaning process so that the effect of organic compounds found in room environment is negligible.

After Si wafers were cleaned different methods were utilized to change their wettability. The untreated Si wafer provides the base surface which happens to be slightly hydrophilic ($\theta_A = 85^o$ and $\theta_R = 72^o$). For altering the surface wettability, extra steps were performed other than the cleaning process. Micro-posts are fabricated on top of the silicon wafer with a diameter of 34 μm, height of 34 μm, and pitch of 50 μm. Because water condensation exists between the posts, a Wenzel state is noticed which renders the silicon wafer more hydrophilic ($\theta_A = 70^o$ and $\theta_R = 50^o$). To render the substrate

hydrophobic ($\theta_A = 107^o$ and $\theta_R = 103^o$), the surface was silanized with a thin layer of polydimethylsiloxane (PDMS) using a conventional dip coating method. The film thickness is negligible compared to the thickness of the silicon wafer and therefore does not impede the heat transfer rate. Inverted micro-posts are fabricated on top of the silicon wafer with a diameter of 40 μm, height 40 μm, and pitch of 50 μm. To obtain superhydrophibicity, a combination of silanization process with the roughened surface yielded a superhydrophobic surface with a high contact angle hysteresis ($\theta_A = 160^o$ and $\theta_R = 127^o$). For the last surface, we utilized an aerosol spray coating method to coat the silicon wafer with WX2100 (purchased from cytonix) in which Fluorothane is the active ingredient. The resultant surface is superhydrophobic with negligible contact angle hysteresis ($\theta_A = 157^o$ and $\theta_R = 154^o$). The contact angle is independent of the coating thickness. Therefore, we coated the surface with about 50 μm without significant impedance of heat transfer.

The surface wettability was characterized before and after each experimental run to assess the homogeneity of their wettability as well as the consistency of contact angle measurements. Droplet shape analyzer (KR$\ddot{U}$SS, DSA100) was used for contact angle measurements. The static advancing and receding contact angles were measured using the protocol outlined in this paper [202]. Measurements were repeated on different spots of the Si wafers to ensure homogeneity and consistency. Droplets with diameters less than the capillary length were tested to ensure negligible effects of gravity. Static advancing and receding contact angles are summarized in Table 1.

5.3.2 Condensation experiments

In Fig.D.1, we show a schematic of the experimental setup which consists of a bubble humidifier, a flow system, and a cooled surface. Dry filtered air was bubbled into a pool of room-temperature DI water through several spargers (Ferroday). The spargers generate micron-sized bubbles which due to their high contact area with water get humidified to above 95%. The humid air generated exists at a room temperature ($T_\infty = 21^o\text{C} \pm 1\ ^o\text{C}$) and ambient humidity of (60% $\pm$1%). Humidity of ambient air and humidified jet was measured using a Hygrometer (VWR). The humidified air was led through a tube (Mc-MASTER-CARR) of inner diameter ($D = 0.047$ in) to impinge normally on the cooled surface. For experimental convenience, the tube was bend to 90^o while allowing enough length ($L = 0.84$ in) before the exist section ensuring fully developed flow beyond the secondary flow region. The flow rate of humidified air was controlled by flow-adjustment valve and measured using a rotameter (OMEGA, model no. FMA-A2323). Volumetric flow rates tested range from 1 LPM to 5 LPM. The humid air jet exits the tube at a standoff distance ($H = 0.32$ in).

The condensation surface was the different Silicon wafers described earlier. The surfaces were placed on an Aluminum substrate with a thermally conductive paste in between. The Aluminum substrate was placed on the cold side of a Peltier plate with a thermally conductive paste. A simple peltier plate with a temperature controller unit was used to maintain a constant surface temperature ($T_s = 15^o\text{C} \pm 1\ ^o\text{C}$). An Infra-red (IR) camera (FLIR, A6753sc), and two flush-mounted k-type thermocouples (OMEGA, HH378) were used to observe the condensation substrate temperature as

well as the condensate droplets. The substrate temperatures measured by the three sensors were in agreement within 1 ^{o}C. This ruled out any possible temperature variation on the surface and ensured that the thermal resistance of vapor-gas side was dominant.

Systematic experiments were performed by first adjusting the flow to the desired jet Reynolds number $Re_j = 4Q/\pi\nu D$, where ν is the kinematic viscosity of humid air. Then, the surface temperature was set to the desired temperature. The condensation process was allowed to reach a quasi-steady state by waiting for about 15 minutes before taking experimental measurements. To visualize the condensation process an optical microscope (Nikon, AZ100) with a high-speed camera (Photron, FASTCAM Nova) were used.

5.4 Results and Discussion

5.4.1 Shedding of Droplets Under Jet Impingement

The dynamics of jet impingement on a surface is characterized by a stagnation region that spans almost two nozzle diameters [14, 28]. Beyond this radial location, a wall jet forms that behaves similar to a Blasius boundary layer. Here we show that the force within the stagnation region provides an excellent shedding capability. To study this, we visualize under a microscope the growth and onset of shedding of droplets under different jet Reynolds numbers $Re_j = 4Q/\pi\nu D$, where Q is the jet flow rate, ν is the kinematic viscosity of humid air, and D is the tube exit diameter (Fig.5.2). To provide consistent comparisons, the surfaces were cleaned prior to each experimental run as outlined in the methods section. Additionally, the ad-

vancing and receding contact angles were measured before and after each experimental run with no significant changes due to mobile droplet shearing effects. Here, we utilized a hydrophobic Si wafer ($\theta_A = 107^o$ and $\theta_R = 103^o$) as the condensation surface (see methods section and Table 1). The jet flow rate was first set to the desired value of jet mean velocity, after which the surface temperature was brought down to the desired temperature ($T_s = 15^oC$). A high speed camera (Photron, FASTCAM Nova) attached to an optical microscope (Nikon, AZ100) was utilized to obtain videos and images of the condensation process (Video 3 and Fig.5.2).

In Fig.5.2, we show the quasi-steady droplet distribution on the condensation surface under different jet Reynolds numbers. In these experiments, the relative humidity of ambient air was 60% and the jet was 95%. The tested surface was a hydrophobic Si wafer with an advancing contact angle of $\theta_A = 107^o$ and a receding contact angle of $\theta_R = 103^o$. In Fig.5.2 and the corresponding Video 3 found in the supplemental material, the droplets can be observed to go through three main growth stages with time: Stage I - slow growth of stationary drops beneath the impinging jet; Stage II - fast growth as mobile droplets move radially outward merging with other droplets; and Stage III - slow growth of droplets that have come to rest far from the center of the impinging jet. In Stage I, single droplets residing on nucleation sites present on the surface initially start growing by direct condensation on their exposed surfaces. As single droplets reach a critical size ($R_c \sim 1/\sqrt{4N_s}$, where N_s is the nucleation site density), they start coalescing with neighboring droplets. The growth mechanism in Stage I can be described by a combination of direct condensation and coalescence with

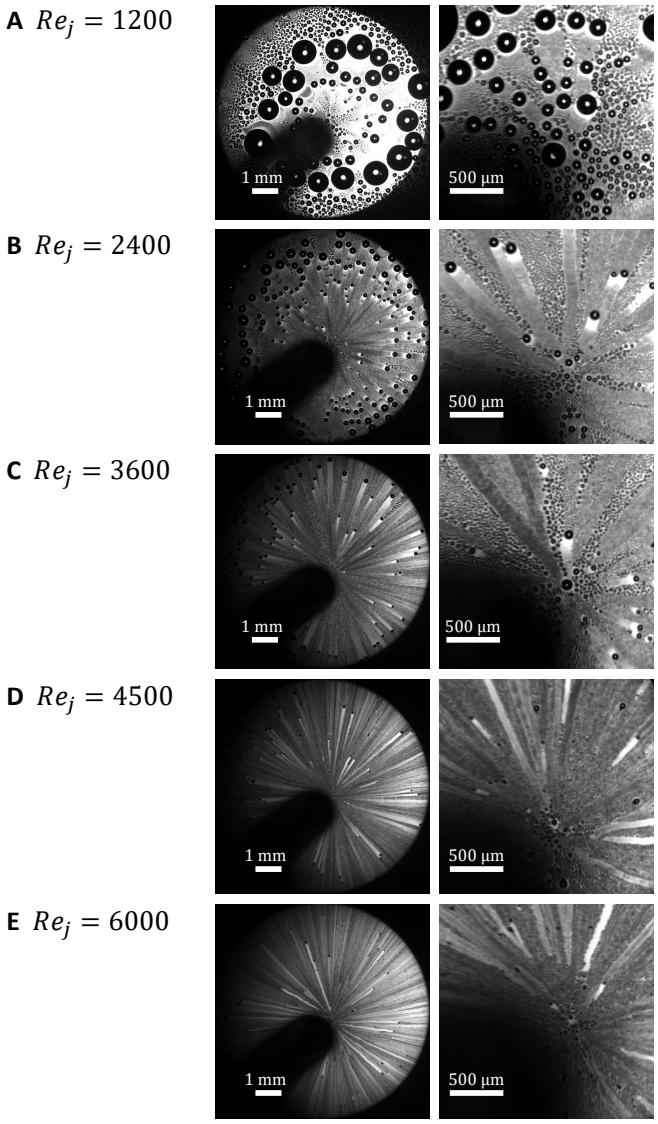

Figure 5.2: Effect of jet Reynolds number on the size of shed droplets. Images show results of condensation experiments performed at an ambient temperature of 21^{o}C and surface temperature of 15^{o}C where the relative humidity of ambient and jet were 60% and 95%, respectively. The tested surface was a hydrophobic Si wafer with $\theta_A = 107^o$ and $\theta_R = 103^o$. Two different close up view are shown for condensation with jet Reynolds numbers of **A.** $Re_j = 1200$, **B.** $Re_j = 2400$, **C.** $Re_j = 3600$, **D.** $Re_j = 4500$, and **E.** $Re_j = 6000$.

neighboring droplets. As droplets grow to another critical size, determined by the jet shedding capability, they start departing their equilibrium location on the surface. The onset of droplet departure is observed to be located near the stagnation region. This implies that droplets in this region possess higher growth rates and experience higher drag forces compared to droplet located further away. It is also observed that the critical droplet size at the onset of departure is reduced with increasing the jet Reynolds number. As droplets depart their first equilibrium location, they start moving radially outward coalescing with droplets in their path (Stage II). The action of movement and coalescence acts as an effective sweeping mechanism for improved DWC. The growth mechanism of a mobile droplet is determined only by coalescence and negligible direct condensation. After droplets move to locations further from the center of the impinging jet, the retention force due to surface tension overcomes the drag force by the gas flow around them and they decelerate and stop. Stationary far-field droplets can be observed clearly in Fig.5.2A but are out of frame in Fig.5.2B-C. Stationary droplets continue to grow by smaller mobile droplets that are generated from the stagnation region following their mother droplet path (stage III).

It is also worth noting that as droplets move along their radial path, they leave dry traces which appear as white traces under the microscope. The process of droplet growth then repeats on the traces until another droplet coming from the stagnation region sweeps it away. Under ideal circumstances, the size of the stationary droplets withing these traces is limited by the size of the mobilized droplets. Hence, a mobilized droplet can be thought of as the maximum size a droplet can grow. In some circumstances,

surface imperfections or dust particles can interfere with the mobile droplet sweeping action but could be mitigated by cleaning the surface thoroughly.

In Fig.5.2A-E, a magnified view of the droplets formed beneath the impinging jets are shown to illustrate the effect that jet velocity and jet Reynolds number have on droplet mobility. At the smallest Reynolds number presented in Figure 2A, $Re_j = 1200$, droplets were not observed to shed even as they grew quite large. In Fig.5.2B, at a $Re_j = 2400$, droplets with radii greater than $R_{max} = 33$ μm were observed to shed and move radially outward coalescing with smaller drops and growing as they moved. With increasing Reynolds number, a further reduction in shedding drop size was observed. For the highest flow rate tested, $Re_j = 6000$, droplets with radii greater than $R_{max} = 13$ μm were observed to shed. These drop sizes are significantly smaller than the case of gravity-assisted droplet shedding or the shearing effect of boundary layer flows where only droplets with radii above 250 microns shed from a hydrophobic surface [184]. Our results clearly demonstrate that the maximum condensed droplet size can be efficiently tuned by controlling the impinging jet velocity and Reynolds number.

Surface wettability is an important factor in determining the shedding capability of a surface regardless of the active mechanism generating the shedding forces. In order to test the effect of wettability on CDC, the results of a series of experiments are presented in Fig.5.3 for five different surfaces with a wide range contact angles at a fixed jet Reynolds number of $Re_j = 3600$. In these experiments, ambient temperature was 21^oC and the surface temperature 15^oC while the relative humidity of ambient air and the jet were 60% and 95%, respectively. The advancing, θ_A, and re-

ceding contact angle, θ_R, for each surface are presented in Table 1 along with the contact angle hysteresis, $\theta_A - \theta_R$. The condensation process and shedding capability is visualized in Fig.5.3 with videos available as supplementary material (Videos 1-5). Two hydrophilic surfaces, one smooth and one microstructured, with different contact angles are presented in Fig.5.3A and 3B. On the smooth hydrophilic surface, Fig.5.3A, droplets with radii greater than 20 μm were observed to shed. The microstructured hydrophilic surfaces has roughly twice the contact angle hysteresis of the smooth hydrophilic surface, $\theta_A - \theta_R = 20^o$ vs 13^o. As a result, the mobility of the droplets is hindered by the increased interfacial pinning force on the droplets caused by the presence of the microstructures and an increase in the radius of the shedding drops was observed to a value of 36 μm. On the other hand, minimizing the contact angle hysteresis, as is done for both the hydrophobic and the nanostructured superhydrophobic surface shown in Fig.5.3C and 3E, dramatically reduces the minimum droplet shedding radius by reducing the interfacial pinning force. For example, droplet radius of the drops shedding from the hydrophobic surface in Fig.5.3C was 13 μm. For the nanostructured superhydrophobic surface shown in Fig.5.3E, the surface looks clear under the microscope with no evidence of the pathlines of shedding droplets clearly visible in Fig.5.3A-C. This is probably due to the low condensation rate due in large part to the low density of nucleation sites on these nanostructured superhydrophobic surfaces, but it could also be the result of droplet jumping from the surface as they coalesce and interfacial energy is recovered in the form of kinetic energy. Some evidence for the presence of droplet jumping can be seen in the videos provided in the

Table 5.1: Advancing and Receding contact angles of the different surfaces used. Surfaces have different wettability and contact angle hysteresis.

Name: Description	θ_A	θ_R	$\theta_A - \theta_R$
Surface 1: Hydrophilic	85 ± 2^o	72 ± 2^o	13 ± 3^o
Surface 2: Hydrophilic Microstructured	70 ± 2^o	50 ± 2^o	20 ± 3^o
Surface 3: Hydrophobic	107 ± 2^o	103 ± 2^o	4 ± 3^o
Surface 4: Superhydrophobic Microstructured	160 ± 2^o	127 ± 2^o	33 ± 3^o
Surface 5: Superhydrophobic Nanostructured	157 ± 2^o	154 ± 2^o	3 ± 3^o

supplementary materials. Droplet jumping has been shown to improve the heat transfer to a surface during condensation [176] and will be discussed in more detail later. Finally, we analyze the results of the microstructured superhydrophobic surface in Fig.5.3D. Interestingly, even though it had the largest advancing contact angle, the microstructured superhydrophobic surface also had the highest contact angle hysteresis. The CDC experiments for this were characterized by a significant pinning of droplets and a very large variability and uncertainty in the size of the shedding droplets. As a result, the discussion of the drop dynamics that follows will be focused primarily on Surfaces 1, 2 and 3 for which repeatable data could be obtained.

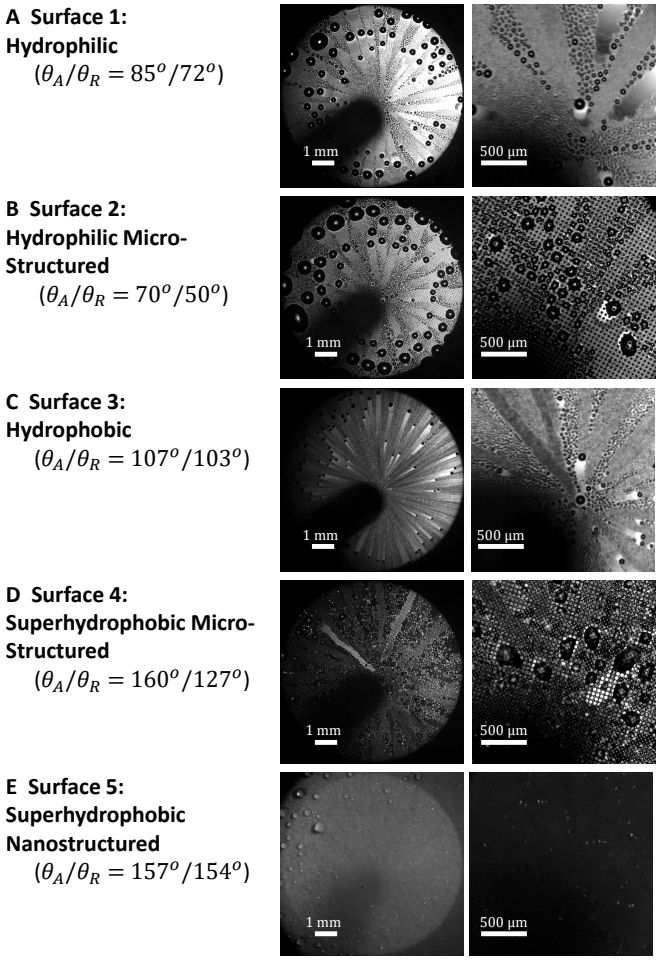

Figure 5.3: Effect of surface wettability on the condensation process. The condensation experiments were performed with an ambient air temperature of 21^oC and surface temperature of 15^oC, while the relative humidity of ambient and jet were 60% and 95%, respectively. Two different close up views are shown for condensation with varying surface wettability and contact angle hysteresis at a fixed jet Reynolds number of $Re_j = 3600$. The advancing and receding contact angles is displayed beside images of each surface.

5.4.2 Dehumidification with CDC for improved heat and mass transfer rates

In this section, we analyze the heat transfer and condensation rates for the CDC and compare their performance with the current state of the art dehumidifiers. To compare the heat flux or condensation rate across many different dehumidifier designs, we compare their compactness factors. The compactness factor indicates the heat or mass transfer rate per unit driving potential (temperature or vapor mass fraction) per unit volume and is defined as follows [150].

$$C_h = \frac{hA}{V} \tag{5.1}$$

$$C_m = \frac{h_m A}{V} \tag{5.2}$$

where C_h is the compactness factor of heat transfer unit, C_m is the compactness factor of mass transfer unit, h is the heat transfer coefficient, h_m is the mass transfer coefficient, A is the surface area over which measurement takes place, and V is the volume of the dehumidification system. In order to experimentally evaluate the mass transfer coefficient, we utilized an optical method of observing the growth of condensate droplets near the impingement region. The mass transfer coefficient can be written as follows.

$$h_m = \frac{\rho_l}{(\omega_\infty - \omega_s)A} \frac{dV_d}{dt} \tag{5.3}$$

where ρ_l is the liquid density, ω_∞ is the vapor mass fraction at ambient conditions, ω_s is the vapor mass fraction evaluated at the surface temperature and dV_d/dt is the condensate volumetric growth per unit time. The

volumetric growth rate can be calculated directly from the video images. To calculate the droplet volume, the droplets are assumed to take the form of a spherical cap because their radii are smaller than the capillary length. For a droplet that is a spherical cap with an optically observed radius of R on the hydrophobic surface, the volume of a droplet can be calculated from

$$V_d = \frac{\pi}{3}(2 + cos\theta_A)(1 - cos\theta_A)^2 R^3 \tag{5.4}$$

The evolution of droplet volume with time was calculated within the impingement region (a surface with a diameter of 1 mm). Additionally, the number and volume of droplets shedding and leaving the impingement region was tracked with time. Because droplets departing the impingement region collect more liquid as the travel radially outward, this procedure provides the lower limit of the condensation rates and the mass transfer coefficient (Fig.5.4A).

In Fig.5.4, results for the mass transfer coefficient and the mass transfer compactness factor are presented for different jet Reynolds numbers. In these experiments, the relative humidity of ambient air was 60% and the jet was 95%. The tested surface was a hydrophobic Si wafer with an advancing contact angle of $\theta_A = 107^o$ and a receding contact angle of $\theta_R = 103^o$. The mass transfer coefficient ranged from $0.2 < h_m < 0.6$ kg/m^2-s while the compactness factors obtained were in the range of $30 < C_m < 300$ kg/m^3-s. The largest values of compactness factor were found for the lowest Reynolds numbers tested. In Fig.5.4B, a comparison of the compactness factor for different dehumidifiers along with the current CDC method is presented

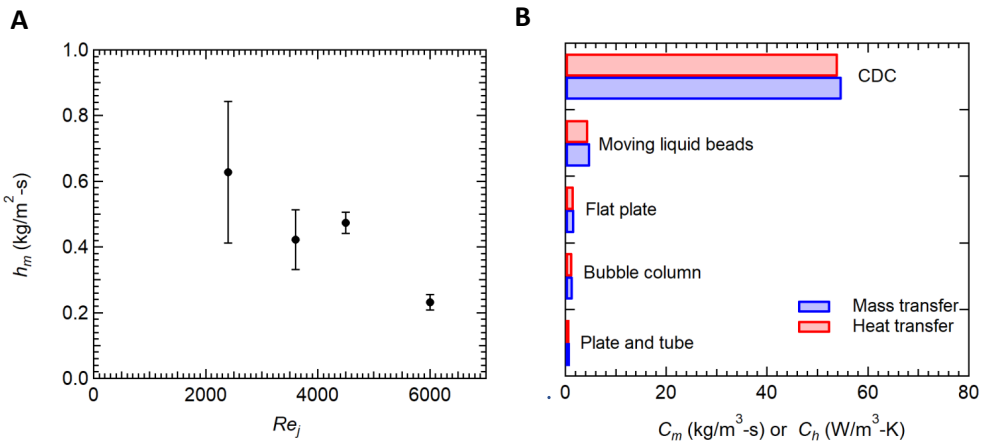

Figure 5.4: **A.** Experimental evaluation of mass transfer coefficient, h_m of CDC as a function of impinging jet Reynolds number. The experiments were performed at an ambient temperature of 21^{o}C and surface temperature of 15^{o}C where the relative humidity of ambient and jet were 60% and 95%, respectively. The tested surface was a hydrophobic Si wafer with θ_A = 107^o and θ_R = 103^o. B. Comparison of heat and mass transfer compactness factors for different state-of-the-art dehumidifiers; plate-and-tube dehumidifier [85], bubble column dehumidifier[90], flat plate dehumidifier [203], moving liquid beads dehumidifier [150]. The average value of our current experiments is shown.

for condensation on hydrophobic surfaces. Four state-of-the-art dehumidifiers are shown namely (1) plate-and-tube dehumidifier [85]; (2) bubble column dehumidifier[90], (3) flat plate dehumidifier [203], (4) moving liquid beads dehumidifier [150]. As seen in Fig.5.4B, even when compared against the lowest value obtained utilizing CDC, the compactness factor of CDC exceeds the highest state-of-the-art dehumidifier by almost 6 times. Thus, CDC provides an extremely compact dehumidifier as well as a very compact heat transfer technique. We expect that even higher values of compactness factor are possible through optimization of geometric parameters like nozzle standoff distance and impinging jet diameter.

5.4.3 Pure steam condensers with CDC for improved heat and mass transfer rates

We now turn to the case of utilizing our method to improve the heat and condensation rates for the case of pure vapor/steam. To characterize the condensation process due to the CDC improved droplet shedding, we visualized the condensation process on different jet Reynolds numbers (Fig.5.2) and different surface wettability (Fig.5.3). As observed, when droplets grow to their maximum droplet size near the stagnation region, they are shed by the jet impingement action. In contrast, in regular gravity-assisted DWC, the shedding mechanism is mainly due to the weight of the droplet. This requires droplets to grow by direct condensation and coalescence with neighboring droplets until reaching the capillary length (mm range) beyond which their weight overcomes the surface tension force. For pure vapor condensation, the high thermal resistance of large droplets reduces the heat transfer significantly (Fig.D.2). In addition, allowing a surface to sustain high droplet size before shedding results in a decrease in the small droplet density (Fig.5.5A). It is well established that droplets with radii below 20 μm contribute to almost 80% of the overall heat transfer to the surface [186]. Therefore, CDC is an efficient means of reducing the maximum droplet size and increasing the population density of droplets below 20 μm (Fig.5.5A).

To evaluate the heat transfer flux, we utilize the analytical model developed by Rose et al. [204, 8]. The overall heat flux to a surface exposed

to condensation in an ambience of pure vapor is given as

$$q'' = \int_{r_{min}}^{r_e} q_d(r,\theta) n(r,\theta) dr + \int_{r_e}^{r_{max}} q_d(r,\theta) N(r,\theta) dr \tag{5.5}$$

where $q_d(r,\theta)$ is the heat transfer through a single droplet with Radius r and contact angle θ, $n(r,\theta)$ and $N(r,\theta)$ are the population density of of small and large droplets, respectively. Droplet below the critical droplet radius ($r_e = 1\sqrt{4N_s}$) grow by direct condensation (small droplets) while droplet above the critical radius grow by direct condensation an coalescence with neighboring droplets (large droplets). The heat transfer through a single droplet can be written as

$$q_d(r,\theta) = \pi r^2 (T_{sat} - T_s - \frac{2T_{sat}\gamma}{\rho_l h_{fg} r})(\frac{1}{2h_i(1-\cos\theta)} + \frac{r\theta}{4k_l \sin\theta} + \frac{\delta_s}{k_s \sin^2\theta})^{-1} \tag{5.6}$$

Detailed analysis is given in Supplementary material (section S-4). It is worth noting that the previous equation was derived for the case of pure vapor. The main variable CDC introduces is the modification of maximum droplet radius value which consequently changes the heat transfer characteristics as shown in Fig.5.5B. Because for this case the jet advective transport does not introduce a thermal resistance, it acts only as an improved shedding mechanism and no further modification is required to Eq.D.15. In Fig.5.5B, the heat flux to a surface is improved significantly by lowering the maximum droplet radius. Improvement as high as almost 150% in heat flux (or condensation rate) can be obtained by utilizing a hydrophilic surface with maximum droplet radius of 20 μm. If one compares utilizing the hydrophilic surface over the superhydrophobic surface,

a maximum improvement of heat flux above 375% can be achieved (see supplementary material section S.4). This shows that heat transfer and consequently condensation rate can be improved by tuning the maximum droplet size which can be achieved easily with CDC.

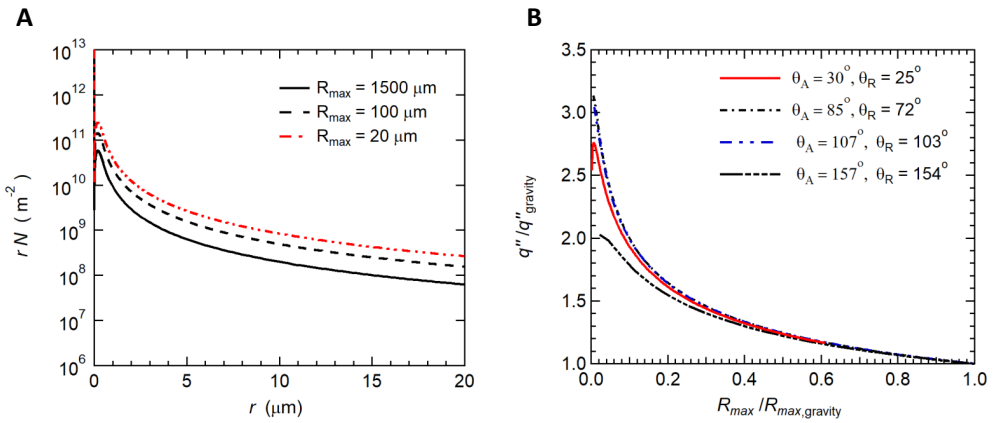

Figure 5.5: Heat transfer characterization of CDC. **A.** The population density of droplets (rN) of radii below 20μm for different maximum droplet radius (R_{max}) being shed by the jet impingement action. The ordinate is defined as the number of droplets per unit surface area. **B.** Heat flux (q'') to a surface exposed to pure vapor analytically evaluated at different maximum droplet radius (R_{max}). The heat flux and maximum droplet radius are normalized with values evaluated in case of gravity-assisted droplet shedding (see supplementary material section S-4).

5.4.4 Jet-Droplet Dynamics

The dynamics of droplet shedding and motion is governed by an interplay between droplet inertia, droplet retention forces due to surface tension, viscous friction within the drop, and drag force due to flow of air around the drop. The effect of each of these was investigated by tracking the motion and size of individual droplets at the different stages of growth and motion as they as they moved across different substrates under different impinging jet conditions. In Fig.5.6A, a sample droplet is traced with time along the hydrophobic surface ($\theta_A = 107^o$ and $\theta_R = 103^o$) for one representative case at a jet Reynolds number of $Re_j = 3600$. The diameter and location of the droplet is plotted as functions of time in Fig.5.6B. Three different periods can be clearly distinguished from the data: Period I - a waiting period before droplet departure; Period II - a period of radial acceleration of the droplet; and Period III - a period of droplet deceleration until the droplet comes to rest. The onset of droplet motion occurs after a waiting period during which the droplet grows through condensation to a critical size. At this critical size, the aerodynamic drag force acting on the droplet becomes larger than the interfacial retention forces acting along the contact line between the droplet and the surface. After the droplet departs its initial location (onset of period II), it coalesces with droplets in its path resulting in a fast growth in droplet size and an acceleration across the surface because with increasing size the aerodynamic drag force grows faster with droplet radius than then the interfacial retention force (R^2 vs. R). During period II, the droplet roughly triples meaning the volume has increased by a factor close to thirty. During period III, the droplet decelerates and the rate of

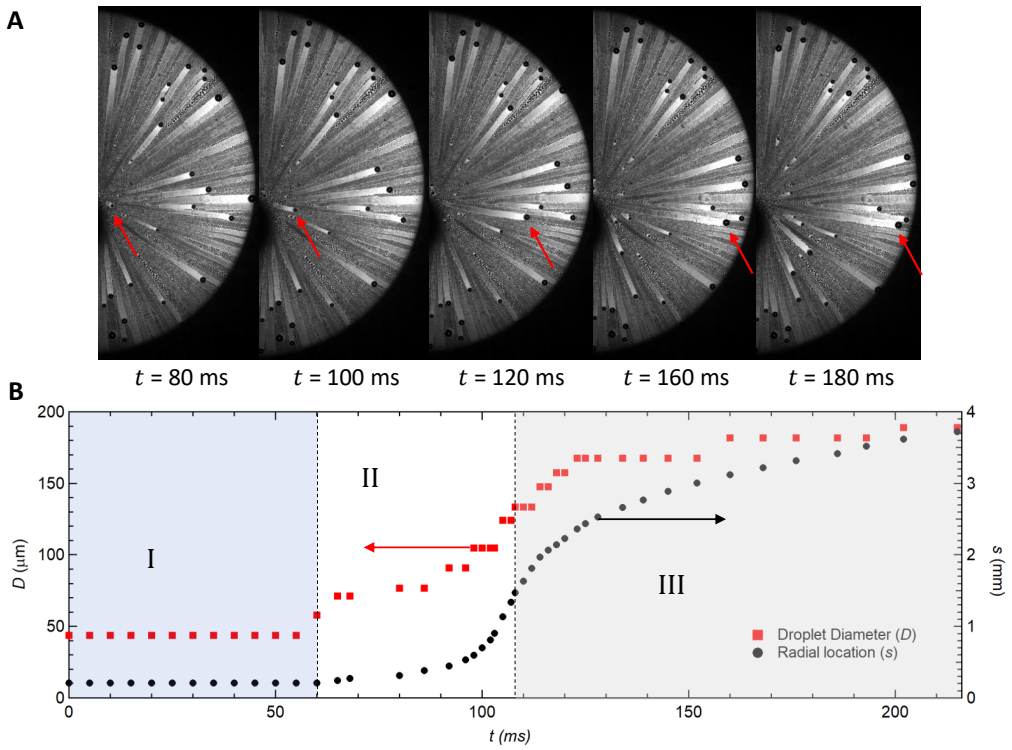

Figure 5.6: **A typical time evolution of droplet motion and growth. A.** Time evolution of a droplet departing its first equilibrium location and moving radially outward. **B.** Typical transience plot illustrating both the location of the droplet (s) and its diameter (D) as it coalesces with other droplets in its path. The droplet goes through three different periods; (I) a waiting period before droplet departure, (II) an accelerating droplet period, and (III) a decelerating droplet period. This plot is generated for a selected case of $Re_j = 3600$ and hydrophobic surface ($\theta_A = 107^o$ and $\theta_R = 103^o$).

diameter growth slows as fewer coalescence event occur. This deceleration occurs because the strength of the shear flow near the wall decreases as the drop moves radially outward from the center of the impinging jet ($1/s$). Qualitatively similar results were observed for all surfaces tested provided the jet Reynolds number was larger than the critical Reynolds number to initiate droplet motion.

In Fig.5.7A, the droplet location (s) is shown as a function of elapsed time ($t-t_o$) for four different jet Reynolds numbers (Re_j) for the hydrophobic surface, where t_o is the time of onset of motion. The different curves show similar trends depicted in Fig.5.6B and the existence of three different motion periods. Note that the transition from period II to period III is delayed by lowering the jet Reynolds number. Additionally, the droplet begins to decelerate at a location further from the center of the impinging jet for larger jet Reynolds numbers. Ideally, we would like to collapse all of these curves onto a single master curve. The obvious choice is non-dimesionalize the time on the x-axis with the jet velocity divided by the jet diameter, $(t-t_0)V_j/D_j$. Unfortunately, this simple non-dimensionalization does not collapse the data. Nor will the data collapse if the critical diameter for droplet motion, D_0, is used in place of the jet diameter, $(t-t_0)V_j/D_0$. The dynamics of drop motion are clearly quite complicated in this process.

In Fig.5.7B, the diameter of droplets is presented at the onset of departure over a range of jet Reynolds numbers for three different surfaces: hydrophobic, hydrophilic and microstructured hydrophilic. For the same jet Reynolds number, the hydrophobic surface, which has the largest advancing contact line and smallest contact angle hysteresis, consistently shows

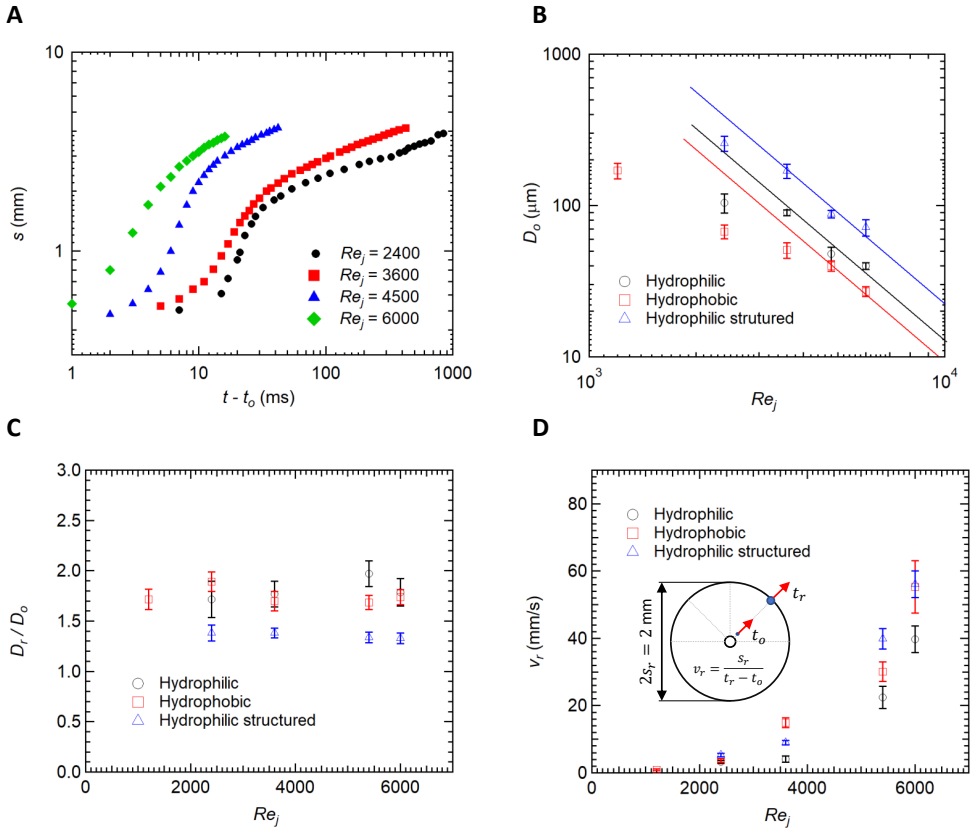

Figure 5.7: Dynamics of droplet-jet interaction. **A.** Droplet location from the center of the impingement region (s) as a function of time ($t-t_o$), where t_o is the time of onset of motion. The plot shows the effect of different jet Reynolds numbers (Re_j) for the hydrophobic surface ($\theta_A = 107^o$ and $\theta_R = 103^o$). **B.** The diameter of droplets at the onset of droplet departure (D_o) is depicted for three different surfaces at different jet Reynolds numbers (Re_j). **C.** For a comparison purpose, ratio of droplet diameter at a reference location ($s_r = 1$ mm) from the center of the impingement region to that at the onset of motion (D/D_o) is plotted against the jet Reynolds numbers (Re_j) for three different surfaces. **D.** a reference apparent speed of droplets ($v_r = s_r/(t_r - t_o)$) at a reference location ($s_r = 1$ mm) is plotted against the jet Reynolds numbers (Re_j) for three different surfaces.

the smallest critical droplet diameter for the onset of droplet motion. With decreasing advancing contact angle and contact angle hysteresis, the critical droplet diameter increases for a given jet Reynolds number with the microstructured hydrophilic surface consistently showing the largest values of critical diameter needed to induce droplet motion. Importantly, the critical droplet diameter can also be tuned by controlling the jet parameters, namely the jet velocity or Reynolds number. As can be seen in Fig.5.7B, increasing jet Reynolds number results in a significant decrease in critical droplet diameter. At large values of jet Reynolds number, a distinct scaling can be observed that suggests, $D_0 \sim Re_j^{-2}$. To investigate this further, forces acting on the droplet at force equilibrium are analyzed just before droplet departure.

The dominating forces are surface tension force along the droplet's contact line and aerodynamic drag forces on the droplet surface. Viscous friction is assumed to be negligible because the droplet is static at this period. The surface tension force along the contact line can be written as [205]

$$F_s = \Gamma_L D_o \gamma (\cos\theta_R - \cos\theta_A) \tag{5.7}$$

where Γ_L is a contact line shape factor and γ is the interfacial surface tension. The value of the contact line shape factor depends on the droplet geometry and symmetry. In general, its value has been experimentally found to lie within $1/2$ and $\pi/2$. [206, 207] It has been observed that the state of motion of a droplet affects the surface tension force acting on a droplet, e.g. static and dynamic behavior [208]. Additionally, external

vertical forces on the droplet can play a role in pinning the droplet [209]. Rather than resorting to a different mathematical description as suggested by Tadmor et al. [210], Eq.5.7 is used and the mentioned effects are absorbed in the order one contact line shape factor, Γ_L.

At equilibrium, the contact line force is balanced by the aerodynamics force generated by impinging jet that is trying to dislodge the droplet. The effects of velocity variation across the boundary layer can be ignored as the droplets are significantly larger than the boundary layer thickness (see supplementary material section S-5) [205, 211, 212, 180]. Thus, the drag force, which is proportional to the stagnation pressure on the droplet, can be written as

$$F_d = \frac{1}{8}\rho_g \Gamma_A C_d u_o^2 D_o^2 \tag{5.8}$$

where C_d is the drag coefficient of the droplet, ρ_g is the surrounding gas density, Γ_A is a shape factor of the projected area of the droplet in the flow direction (see supplementary material section S-5), and u_o is the effective air velocity around the droplet. Note that u_o scales with the jet mean velocity, $u_o \sim v_j$, and decays with distance from the location of jet impingement. Balancing the forces acting on a droplet at the onset of motion, yields the following relation.

$$D_o = \frac{\gamma(\cos\theta_R - \cos\theta_A)\Gamma_L}{\frac{1}{2}\rho_g C_d \Gamma_A}\frac{1}{v_j^2} \sim \frac{1}{Re_j^2} \tag{5.9}$$

Note that the scaling of critical diameter with jet Reynolds number predicted by Eq. 5.9 fits the experimental data in Fig.5.7B quite well for the high jet Reynolds number cases of all three surfaces tested. However, a

deviation is observed at the lowest jet Reynolds number studied. This is likely attributable to the complexity of evaluating the geometrical shape factors and the drag coefficient which are not constant as assumed her, but depend on the air velocity and diameter of the drop [182].

Following the onset of droplet motion, the droplets grow through a combination of continued condensation, which is slow, and coalescence with smaller stationary droplets in their path, which is fast. At least initially, increasing droplet size is observed to result in an acceleration of the drop and an increased droplet velocity. As shown by Eq. 5.7, the interfacial retention force increases with $F_s \sim D$, while the aerodynamic drag force in Eq. 5.8 scales increases with $F_d \sim D^2$. Hence, as the droplets coalesce and grow beyond the critical diameter for droplet motion where these two forces are in balance, a force imbalance favoring aerodynamic drag over retention force exists and the droplets accelerate. In order to quantify the rate of droplet diameter growth during this acceleration period, the droplet diameter normalized by the critical diameter, D_r/D_o, was measured at a reference location ($s_r = 1$ mm) and is plotted against the jet Reynolds number for each of the three surfaces. A schematic diagram is shown in in Fig.5.7D as a reference. The reference location lies within the accelerating period (Period II) for all the cases presented. In Fig.5.7C, the diameter of each droplets was found to increases significantly by the time it reached a position 1mm from the center of the impinging jet. The hydrophilic structured surface, which had the largest contact angle hysteresis shows the smallest increase in droplet diameter with an average of just $D_r/D_o = 1.35$. This diameter increase suggests a volume increase of roughly 2.5x meaning that on average

2.5 coalescence events with similar sized drops have occured during the first 1mm of travel. Within uncertainty, no significant difference between the hydrophilic and the hydrophobic cases could be observed. On average, the droplets on these surface grew faster than the microstructured hydrophilic surface with an increase of in droplet diameter of roughly $D_r/D_o = 1.7$ and a corresponding volume change of 5x. It is interesting to note that even though the size of droplets is different under varying jet Reynolds numbers, the ratio of increase is constant for the same surface wettability independent of jet Reynolds number. This suggests a self-similarity property of the condensation process.

In Fig.5.7D, the velocity of the droplets, v_r is presented as a function of jet Reynolds number. Here, again the velocity is measured at a location within the accelerating region ($s_r = 1$ mm). The droplet velocity can be seem to vary monotonically with the jet Reynolds number. Moreover, the droplet apparent speeds are similar for the three surfaces within the experimental uncertainty. A simplistic equation of motion (EOM) is given in supplementary material section S.6. In the acceleration period, the drag force is assumed to be much greater than the retention forces. This in turn means that the droplet motion in Period II should be independent of the surface wettability which agrees with our experimental observation in Fig 7D.

5.5 Further Discussion

A novel continuous drop-wise condensation that is efficient and compact is achieved by utilizing jet impingement of water vapor on a cooled surface. The fluid dynamics of an impinged jet showed an excellent shedding capability to overcome the limitations of the state-of-the-art techniques.

The droplets generated withing the impingement area are of sizes less than the capillary length of water (or bond number $Bo << 0.1$). Therefore, gravitational force effect is negligible which in turn means the current analysis is independent of surface orientation. Gravitational force will be effective on the stationary droplets which reside in the region corresponding to the decelerating period (Period III, Fig.5.6B). The effect of gravitational force as well as other dominating forces, such as viscous dissipation are subjects of future research.

It was noticed that in surfaces that are characterized by high contact angle hystereses droplets tend to stop at random locations corresponding to the decelerating period (Period III in Fig.5.6B). This indicates that the droplet shedding advantage of jet impingement is lost away from the impingement region. We believe that this does not undermine the effectiveness of CDC as most of vapor condensation takes place where shedding is significant. To overcome the accumulation of condensate in that region, different engineering solutions could be applied. Placing the condensation surface vertically helps with shedding larger droplets. It is experimentally observed that stationary droplets in regions corresponding to period III grow quickly by droplet feeding coming from the impingement region. Other methods,

such as surface texturing or capillary wicking could be utilized to effectively drain excessive condensate.

Surfaces with low contact angle hystereses tend to show better uniformity of droplet shedding and stoppage location. The shedding of droplets is further improved by droplet jumping in the case of superhydrophobic surface ($\theta_A = 157^o$ and $\theta_R = 154^o$). As noticed in Fig.5.3E and video S.6, droplets in the micro-scale jump off the surface due to the release of energy upon coalescence. This phenomenon has been shown earlier to have potential in improving DWC [176] and energy harvesting [213]. A great advantage offered by CDC is that jumping droplets are further shed by flow generated from jet impingement. Hence, mitigate the return of micro-droplets on the surface and therefore prevent flooding of the surface.

5.6 Summary and concluding remarks

A novel continuous drop-wise condensation that is efficient and compact was achieved by utilizing jet impingement of water vapor on a cooled surface. The fluid dynamics of an impinged jet showed an excellent shedding capability to overcome the limitations of the state-of-the-art techniques.

In summary, we have demonstrated the capability of our CDC design in improving the condensation process substantially compared to state-of-the-art condensers and humidification technologies. We performed condensation experiments on modified and unmodified Silicon substrates on a broad range of contact angles. The drop size being shed was controlled by tuning the jet parameters namely the jet velocity in this work. We showed that micron-

sized droplets could be shed effectively even on hydrophilic surfaces.

By comparing the condensation rate per unit volume of state-of-the-art dehumidification technologies, we showed that our design is at least six fold higher. This significant increase is attributed to the thinning of the diffusion layer which is known to impede vapor condensation. We also illustrated that by controlling the maximum droplet size being shed, improvements as high as 375% in heat flux was possible for steam condensers in the absence of NCG.

Finally, we discussed the droplet dynamics and growth under the jet impingement action. By comparing the different forces acting on a droplet, we were able to predict the size of droplet being shed under varying jet Reynolds number and surface wettability. Furthermore, the models presented in this work are the starting point for further optimization of the design to obtain more compact dehumidification using CDC technique.

CHAPTER 6

Overall Conclusion

In this thesis, the problem of condensation in the presence of non-condensable gases (NCG) was further investigated. This problem is termed Breath Figure Condensation (BFC) for reasons discussed in section 1.2. Even though the condensation heat transfer rates are of great magnitudes, this advantage is hindered by the presence of minute traces of NCG. Several techniques have been implemented in the literature to tackle the problem, such as vacuuming the condenser prior to condensation. Additionally, utilizing several active methods, such as fluid/surface vibration, electrohydrodynamic effects, or rotating surfaces, has shown great potential in alleviating the NCG effect. On the other hand, improving the condensation rates in the absence of NCG has been steered towards altering surface wettability. The latter technique is effective in generating drop-wise condensation (DWC) rather than film-wise condensation (FWC). The latter type of condensation is characterized by about an order of magnitude lower heat transfer rates than the former. However, to this date, the coating techniques that have been used are physically and chemically unstable. In a recent publication, it was concluded that "nine decades of research on dropwise condensation have still not produced a satisfying heat transfer surface design that allows

its stable low-maintenance industrial application. This is mainly due to the fact that its fundamental mechanisms are not yet fully understood" [77]. Therefore, in this thesis, we further investigated the process of condensation especially with the presence of NCG - BFC. Additionally, we introduced a novel technique to maintain efficient DWC even on wettable surfaces.

To assess the problem of condensation, numerical simulations provide excellent tools to understand the underlying physics of the problem. Our literature survey revealed that the state-of-the-art simulation techniques were divided to two categories; 1- models that ignored the condensate film and simulated only the gas-vapor domain, and 2- models that included the condensate film. The first models were observed to be effective in case of high NCG mass fractions ($> 10\%$). The second models are valid for the entire range of NCG concentrations, however, with an additional computational cost due to the necessity of simulating two domains and a coupling interface separately. With the lack of a model that encompasses the entire NCG mass fractions and is characterized by a low computational cost, we proposed our numerical-analytical technique. In this technique, the governing equations in the gas-vapor domain (continuity, momentum, energy, ans species conservation equations) were solved independently. Additionally, heat transfer rates in the condensate film were obtained analytically. An iterative algorithm is used to couple the two solutions through the liquid-gas interface while the mass and energy across the interface were conserved. Several concluding remarks were obtained as follows.

1. Excellent agreement between the current model and experimental work was observed. Contrasting the current model with state-of-the-

art models as well as heat and mass transfer analogy showed that our model outperformed them in several aspects. Comparisons of the computational cost (computational time) showed that our model was much lower than the most recent models by almost three folds. for similar geometries. Models that ignore the condensate film, neglects its thermal resistance which is valid for extremely high NCG mass fractions. However, we showed that for NCG mass fractions above 20%, the thermal resistance of the condensate film is an order of magnitude lower than that of the diffusion layer. This indicated the range of validity for ignoring the condensate film. For NCG mass fractions below 20%, both domains should be included in modeling the condensation process.

2. Even though neglecting the condensate film is valid for the aforementioned NCG concentration range, neglecting it comes with the problem of underestimating the liquid-gas interface temperatures despite the valid heat transfer rates obtained. This, in turn, might result in inaccurate heat exchanger designs or unpredictable chemical reactions that may depend on the interfacial temperature.

3. Excellent matching was obtained between the current model and the analytical model of Sparrow and coworkers for nearly pure vapor condensation. With this validation, we proposed a model of condensation heat and mass transfer systems that encompasses the entire range of NCG mass fractions ($0\% - 100\%$) for an axisymmetric condensation surface.

After developing the numerical model to simulate the steady state condensation problem, we observed the fact that for high NCG concentrations, the nature of the condensate formation is not important in determining the overall heat and mass transfer rates. However, we postulated that the frequent disruption of the diffusion boundary layer due to droplet departure on a surface should improve the condensation rate. The effect of droplet departure in disrupting the diffusion boundary layer should act as a mixing mechanism and therefore thin the boundary layer. To understand this, we developed a simplified one dimensional model to understand the transient nature of condensation in the presence of NCG. In the simplified approach, we modeled the problem as two semi-infinite gas and solid domains in contact with the condensate film as a coupling condition. The typical transient behavior of heat and condensation rates start by very high values and decrease to steady state rates. This suggested that by frequently sweeping off the surface in a frequency such that steady state has not been reached yet, the over-all time-averaged heat and mass transfer rates would be greater than the steady state value, i.e. without sweeping. The effect of different variables were presented, such as the degree of surface subcooling, surface effusivities, and ambient NCG mass fractions. We drew our model from the analogy between this problem and the nucleate boiling problem. In developing nucleate boiling (NB), the bubble departure acts as a mixing mechanism by frequently disrupting the superheated thermal boundary layer near the heated surface. However, unlike in the case of NB, typical boundary layer thicknesses are much greater than the droplet size. Additionally, the droplets typically depart parallel to the surface. Therefore, in

typical DWC studies, no clear improvement has been reported in the presence of NCG. To overcome this problem, we introduced jet impingement technique as a viable solution to thin the diffusion layer significantly. An additional advantage we obtained from jet impingement condensation was the better droplet removal rates due to the high shedding forces caused by stagnation flow. The two advantages provided by the solution were theoretically in accordance with our understanding to frequently disrupt the diffusion boundary layer.

In the last two chapters, we discussed the potential of utilizing jet impingement as a means for improving the condensation rate in the absence or presence of NCG. Even though the use of this technique has shown great potential in other heat and mass transfer processes, its use in condensation has been extremely limited. Initially, my family and I tried an interesting home experiment in which we used a paper straw and a bathroom mirror. Upon breathing into the straw and directing the exiting jet to the mirror, we observed initially the appearance of a typical fogging spot that was circular in shape. We tried different straw shapes, the spot was similar to the tube's exit cross section. We also observed that upon breathing stronger (faster jet), the shape retained its size, i.e. did not expand to cover a larger foot print. We tried going closer to the mirror but the shape and its size remained unchanged. Additionally, as we breathed with a higher jet velocity, we observed that micro-droplets depart the surface in an axissymetric fashion in a mesmerizing way. Taking this experiment to the lab allowed for further parametric control of the variables pertaining to this problem.

In chapter 6, we discussed the breath figure (BF) spot appearance and

size with varying the jet velocity, surface temperature, and tube-to-surface standoff distance. A humidified air jet was generated buy bubbling dry air into a pool of room-temperature water. The humidified air jet was directed to impinge normally on a cooled surface. By visualizing the generated BF spot under the mentioned variables several concluding remarks were obtained.

1. For a given jet Reynolds number and standoff distance, there exists a temperature below which the BF spot appears. This temperature was equivalent to the dew point temperature at the center of the jet. Increasing the standoff distance shifted the appearance of the BF spot to a lower surface temperature. This was inline with the understanding that the vapor content in the jet diffuses into the ambience as it travels further into the latter. Therefore, less vapor content reached the surface as it traveled longer distances.

2. In the case of lowest jet Reynolds number ($Re_j = 500$), the jet threw more water vapor content to the ambience than the higher jet Reynolds cases. This could be attributed to the higher mixing due to turbulent eddies in the higher jet Reynolds cases. Within the developing jet region ($H/D < 5$), we observed that the appearance of the BF spot is independent of the standoff distance. This is attributed to the fact that diffusion effect has not reached the center of the jet. However, the inverse proportionality discussed earlier was noticed beyond the developing region.

3. For a given jet Reynolds number and standoff distance, lowering the

surface temperature below the onset temperature discussed above acted to expand the extent of the BF spot on the surface, i.e. an increase in its diameter. It was observed under the microscope that the boundary of the BF spot separates two regions; DWC withing the BF spot, and a dry region outside the BF spot. This indicated that the BF spot is the region over which effective condensation takes place. Therefore, it is crucial to quantify such region and how other variables could affect it.

4. The effect of the jet Reynolds number is quite interesting. We observed that in the turbulent jet cases ($Re_j > 1340$), the jet speed had no influence on the extent of the BF spot at a given standoff distance and surface temperature. This conclusion was inline with our home experiment mentioned earlier.

5. Based on our previous understanding and the information in the literature, we hypothesized that the BF spot is a manifestation of a recovery concentration concept. This concept was drawn from its analogous recovery (adiabatic-wall) temperature discussed extensively in heat transfer determination for jet impingement heat transfer applications. As in the case of recovery temperature, recovery concentration is extremely important in quantifying the mass transfer rates due to jet impingement processes. Even though the concept of recovery concentration can be inferred from heat and mass transfer analogy, it has not been reported in the literature. More specifically, the fact that BF spots are manifestations of the recovery concentration is shown for the first time.

6. Based on the mentioned heat and mass transfer analogy, we developed a theoretical model to predict the concentration of water vapor on a cooled surface exposed to a jet of humidified air. Theses predictions can be extended to any other jet impingement processes where species transport is important. Excellent agreement between the experimental results and the theoretical derivations were found. A Numerical model was also appended to the chapter presenting a good agreement and visual understanding of the problem.

In Chapter 6, we initially started by observing how droplets grow, coalesce, and depart the stagnation region. In parallel to this observation, we shed some light on how this technique improved the compactness of heat and mass transfer system. The main concluding remarks can be summarized as follows.

1. Utilization of jet impingement as a technique to augment condensation rate has not been investigated thoroughly in the literature. This work is the first attempt to tackle the complex problem which consists of an interplay of heat transfer, species transfer, phase change, fluid dynamics and interfacial physics, to name a few.

2. Observations of the condensation process under the microscope proved that with this technique, the droplets being shed were effectively reduced for the same surface wettability condition by tuning the jet parameters namely the jet velocity in this work. For instance, droplets as low as 20 μm in radius were shed with this technique for a hydrophilic surface (θ_A / $\theta_R = 85^o/72^o$) surpassing the traditional gravity-assisted

shedding mechanism by almost 80 folds. This translated to an improvement of nearly 150% in heat transfer rates in pure vapor condensation case.

3. Different surfaces with a wide range of contact angle and contact angle hysteresis were investigated. We showed that even though highly non-wetting surfaces are characterized by lower droplets being shed under the same jet parameters, wetting surfaces showed comparable performance. This alleviates the heavy dependence on coating techniques reported in the literature. On the other hand, it is extremely desirable to shed smaller droplets for hydrophilic surfaces. This is due to the higher thermal conductance of droplets residing on hydrophilic surfaces compared to them residing on hydrophobic surfaces, i.e. the higher droplet thickness associated with the latter.

4. To observe the droplets growth under the jet impingement influence, we traced a single droplet from a moment where the surface was swept off by a past generation droplet to the point it grew and started moving. We noticed three different growth stages under the microscope; Stage I - slow growth of stationary drops beneath the impinging jet; Stage II - fast growth as mobile droplets moving radially outward merging with other droplets; and Stage III - slow growth of droplets that have come to rest far from the center of the impinging jet.

5. To investigate the droplet dynamics, a single droplet was traced from the moment it departs the stagnation region. Results showed that the droplet mobility went through three periods of motion; Period I

- a waiting period before droplet departure; Period II - a period of radial acceleration of the droplet; and Period III - a period of droplet deceleration until the droplet came to rest. Scaling analysis of the acting forces on a single droplet was matched with the experimental results with a good agreement.

6. Lastly, we evaluated the heat and mass transfer rates using an optical method from the microscopic images obtained. The effect of jet Reynolds number on the mass transfer coefficient was investigated as an initial attempt to quantify the parameter. From the experimental evaluations, we compared the compactness of our technique with state-of-the-art dehumidification technology. Utilizing jet impingement condensation proved to be superior as a compact mass exchanger design.

7. Lastly, we extended the calculations to include pure vapor condensation. We showed using a well-known analytical solution, that by reducing the size of shed droplets a high improvement in heat transfer rates were possible. It was illustrated that by controlling the maximum droplet size being shed, improvements as high as 375% in heat flux was possible for steam condensers in the absence of NCG.

APPENDIX A

Supplementary Material for Chapter 2

A.1 Modification to Dehbi's empirical correlation

A. Dehbi (2015) [118] presented a generalized correlation of overall heat transfer coefficient for steam condensation in the presence of air under turbulent free convection. The correlation was based on a basic theoretical origin and was validated for a wide range of operating pressures, i.e. up to 20bars, and steam mass fractions, i.e. 10-95%. The resulting correlation gave a standard deviation of about 16% for the 350 points studied. In the following, we extend Dehbi's work to include the effect of the condensate film. The general correlation of overall heat transfer coefficient is given in Eq. A.1.

$$\overline{h} = 0.185 D_{ij}^{2/3} (\rho_s + \rho_\infty) \big(\frac{\rho_s - \rho_\infty}{\mu_g}\big)^{1/3} \frac{h_{fg}}{T_\infty - T_s} \ln \big(\frac{\omega_{v,s}}{\omega_{v,\infty}}\big) \tag{A.1}$$

Eq. A.1 was derived based on the assumption that convective heat transfer coefficient is negligible compared to latent heat of condensation. In addition, the condensate film heat transfer coefficient was ignored due to the low resistance it provide to the argument. The generalized correlation works quite well in predicting the effect of different parameters on the overall

heat transfer coefficient while other ignored factors are absorbed in the leading constant [118]. In order to estimate the heat transfer coefficient of condensation and condensate film, we resort to Nusselt's solution given in Eq. A.2.

$$\overline{h}_l = 0.943\left[\frac{h'_{fg}\rho_l^2 g k_l^3}{\mu_l L(T_o - T_s)}\right]^{1/4} \tag{A.2}$$

The heat transfer flux to the condenser can be calculated using Eq. A.3

$$q = \overline{h}(T_\infty - T_s) = \overline{h}_l(T_o - T_s) \tag{A.3}$$

Knowing the ambient conditions and surface temperature, one could easily find the overall heat transfer coefficient using Eq. A.1. Then, using Eq. A.2 and Eq. A.3, the interfacial temperature and the corresponding film heat transfer coefficient are found.

A.2 Heat/mass transfer analogy

In all the validated cases we compared our model with heat/mass transfer analogy due to the similarities between the two approaches. Figure B.1 shows a simplified model of the condensation problem with NCG adopted from Deen [214]. For a vertical condenser, Nusselt's theory provides the film heat transfer coefficient which is given in Eq. A.2.

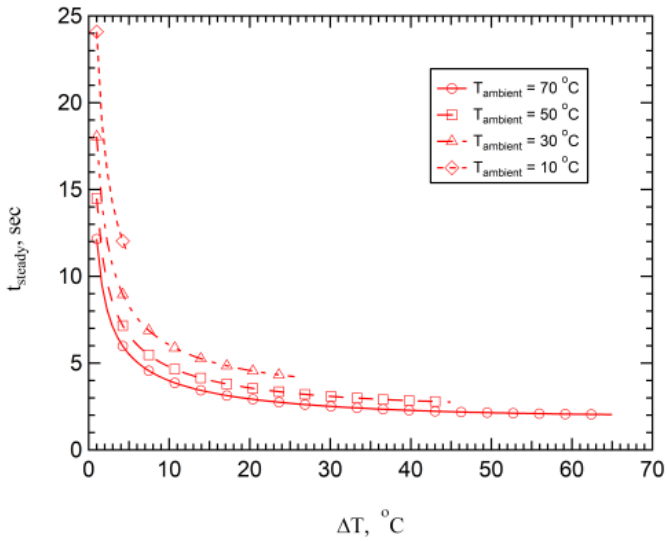

Figure A.1: Configuration of the simplified model of the film wise condensation problem with NCG.

The condensation rate can be found by solving a simplified 1D species transport equation given in Eq.A.4.

$$\frac{dn_i}{dy} = 0 \tag{A.4}$$

Where the total mass flux (n_i) of either vapor or NCG species is given

as

$$n_j = -D_{ij}\vec{\nabla}\rho_j + \omega_j \sum n_j \tag{A.5}$$

For the non-condensable component, the solution gives a zero net mass flux throughout the domain, i.e. normal to the condensation surface. Substituting Eq. A.5 and applying the known mass concentrations at the diffusion layer boundaries give the vapor mass flux as

$$n_v = \frac{\rho D_{ij}}{\delta_g} ln\left[\frac{1-\omega_{v,\infty}}{1-\omega_{v,o}}\right] \tag{A.6}$$

The vapor mass flux can be calculated using a convective mass transfer coefficient as well as in Eq. A.7

$$n_v = \frac{\beta Sh_o \rho D_{ij}}{L}\left(\frac{\omega_{v,\infty}-\omega_{v,o}}{1-\omega_{v,o}}\right) \tag{A.7}$$

Equating Eq. A.6 and Eq. A.7 results in a solution of the diffusion layer thickness. To infer the heat transfer coefficient due to condensation and convection, a simplified energy equation is given by

$$-k_g\frac{d^2T}{dy^2} + n_v c_{p,v}\frac{dT}{dy} = 0 \tag{A.8}$$

Solving the differential equation subjected to known temperatures at the diffusion layer boundaries gives an expression of temperature as

$$T(y) = \frac{1}{exp[\zeta]-1}\left[T_\infty(exp[\zeta(\frac{y}{\delta_g})]-1) + T_o(exp[\zeta]-exp[\zeta(\frac{y}{\delta_g})]\right] \tag{A.9}$$

Where we define the exponential power as $\zeta = n_v c_{p,v} \delta_g / k_g$. Finally, an energy balance at the condensation interface yields a closure relation given in Eq. A.10

$$\left.\frac{dT}{dy}\right|_{y=0^+} = \frac{1}{k_g}\left(n_v h_{fg} + \overline{h}_l (T_o - T_s)\right) \tag{A.10}$$

An iterative solution is then performed where a value of interfacial temperature is guessed initially. The corresponding film heat transfer coefficient, vapor mass flux, and diffusion layer thickness are found using Eq. A.2, Eq. A.6, and Eq. A.7, respectively. The terms left to the equal sign in Eq. A.10 is evaluated using Eq. A.9. Different interfacial temperature are tried until Eq. A.10 is satisfied.

APPENDIX B

Supplementary Material for Chapter 3

B.1 Theoretical Derivation of Pure Vapor Transient Condensation

In these pages, I replicate the work of Sparrow and Siegel [119] considering transient film condensation of pure vapor over a verticl plate. In this work we start by applying an energy balance over an element of the condensate film having a height of dx and thickness of $\delta(x,t)$. The energy equation can be written in an integral form as

$$\rho C_p[\frac{\partial}{\partial t}\bigg(\int_0^\delta (T-T_o)dy\bigg)+\frac{\partial}{\partial x}\bigg(\int_0^\delta u(T-T_o)d\eta\bigg)] = h_{fg}\frac{\partial \dot{m}}{\partial x}-k(\frac{\partial(T-T_o)}{\partial y})\bigg|_{y=0} \tag{B.1}$$

Assuming the steady state velocity and temperature profiles can be used in the transient case, with the understanding that the condensate film thick-

ness is a function of both time and position x.

$$u(y) = \frac{g(\rho_l - \rho_v)\delta^2}{\mu_l}(\zeta - \frac{\zeta^2}{2}) \tag{B.2a}$$

$$\theta = \frac{T - T_o}{T_w - T_o} = 1 - \zeta \tag{B.2b}$$

where $\zeta = y/\delta(x,t)$. Substituting the equations into the Eq. B.1 results in the following differential equation

$$\frac{1}{2}\frac{\partial\delta}{\partial t} + \frac{g(\rho_l - \rho_v)}{2\mu_l}\delta^2\frac{\partial\delta}{\partial x} = \frac{h_{fg}}{C_{p,l}(T_w - T_o)}\frac{\partial(\dot{m}/\rho_l)}{\partial x} - \frac{\alpha_l}{\delta} \tag{B.3}$$

In order to get rid of the condensation rate term, we resort to the conservation of mass which takes into account the accumulation of condensate with time. The resulting equation is

$$\frac{\partial(\dot{m}/\rho_l)}{\partial x} = \frac{\partial\delta}{\partial t} + \frac{\partial}{\partial x}\left(\int_0^\delta u dy\right) \tag{B.4}$$

Substituting the velocity profile gives

$$\frac{\partial(\dot{m}/\rho_l)}{\partial x} = \frac{\partial\delta}{\partial t} + \frac{g(\rho_l - \rho_v)}{\mu_l}\delta^2\frac{\partial\delta}{\partial x} \tag{B.5}$$

This translates to the sum of the accumulated and advected condensate is equal to the total condensation rate. Substituting Eq. B.5 into Eq. B.3 results in the following relation

$$P\frac{\partial \delta}{\partial x} + Q\frac{\partial \delta}{\partial t} = R \tag{B.6}$$

Where the parameters appearing in the above equation are

$$P = \frac{\rho_l(\rho_l - \rho_v)gh'_{fg}}{k\mu_l(T_o - T_w)}\delta^3 \tag{B.7a}$$

$$Q = \frac{\rho_l h'_{fg}}{k(T_o - T_w)}(1 + \frac{1}{8}\frac{C_{p,l}(T_o - T_w)}{h'_{fg}})\delta\delta^3 \tag{B.7b}$$

$$R = 1 \tag{B.7c}$$

Using the characteristic method of solving the partial differential equation results in the following

$$\frac{dt}{dx} = \frac{Q}{P} = \frac{1}{\delta^2}\left[\frac{\mu_l(1 + \frac{C_{p,l}(T_o - T_s)}{8h'_{fg}})}{g(\rho_l - \rho_v)}\right] \tag{B.8a}$$

$$\delta^3\frac{d\delta}{dx} = \frac{k_l\mu_l(T_o - T_w)}{\rho_l(\rho_l - \rho_v)gh'_{fg}} \tag{B.8b}$$

$$\delta\frac{d\delta}{dt} = \frac{k(T_o - T_w)}{\rho_l h'_{fg}\left[1 + \frac{C_{p,l}(T_o - T_s)}{8h'_{fg}}\right]} \tag{B.8c}$$

Subjecting the last two equations to the boundary and initial conditions

$\delta(x,0) = \delta(0,t) = 0$ and integrating in an ordinary manner gives

$$\delta_{steady} = \left[\frac{k_l \nu_l (T_o - T_w)}{4(\rho_l - \rho_v) g h'_{fg}} x\right]^{1/4} \tag{B.9a}$$

$$\delta(t) = \left[\frac{k(T_o - T_w)}{2\rho_l h'_{fg}\left[1 + \frac{C_{p,l}(T_o - T_s)}{8h'_{fg}}\right]} t\right]^{1/2} \tag{B.9b}$$

If we equate the two equations, we obtain the time at which steady state condensation occurs, which is

$$t_{steady} = \left[\frac{h'_{fg}\rho_l \mu_l}{kg(T_o - T_w)(\rho_l - \rho_v)} x\right]^{1/2} \left(1 + \frac{1}{8}\frac{C_{p,l}(T_o - T_w)}{h'_{fg}}\right) \tag{B.10}$$

The heat transfer coefficient can be written as

$$h_{steady} = \left[\frac{k_l^3(\rho_l - \rho_v) g h'_{fg}}{4\nu_l (T_o - T_w) x}\right]^{1/4} \tag{B.11a}$$

$$h(t) = h_{steady}\left(\frac{t_{steady}}{t}\right)^{1/2} \tag{B.11b}$$

Figure B.1 shows the effect of subcooling level on the steady-state time at different ambient temperatures for pure vapor condensation. It is clear that the lower the subcooling of the condensation surface, the higher the duration of transience. The ambient temperature has an insignificant effect of the steady-state time especially at high subcooling degrees. In contrast

to the vapor condensation with NCG, pure vapor condensation is characterised by higher time scales. This, in turn, suggests that condensation can be improved by lower sweeping-off frequencies compared to those of vapor condensation in the presence of NCG.

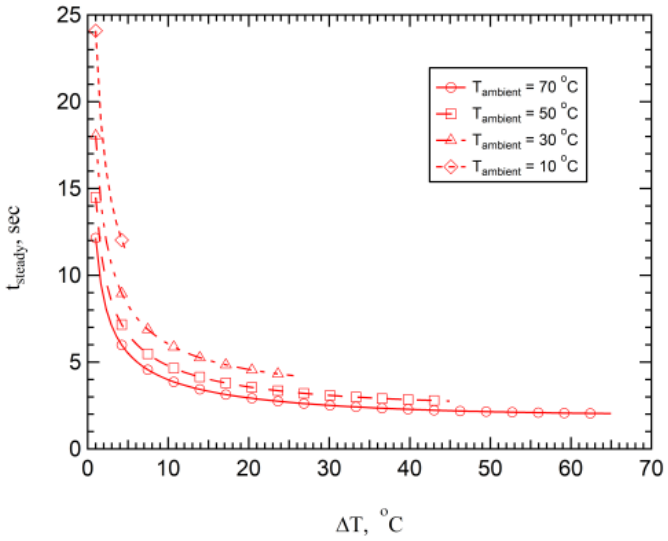

Figure B.1: Effect of the subcooling degree at different ambient temperatures on the steady-state time for pure vapor condensation.

APPENDIX C

Supplementary Material for Chapter 4

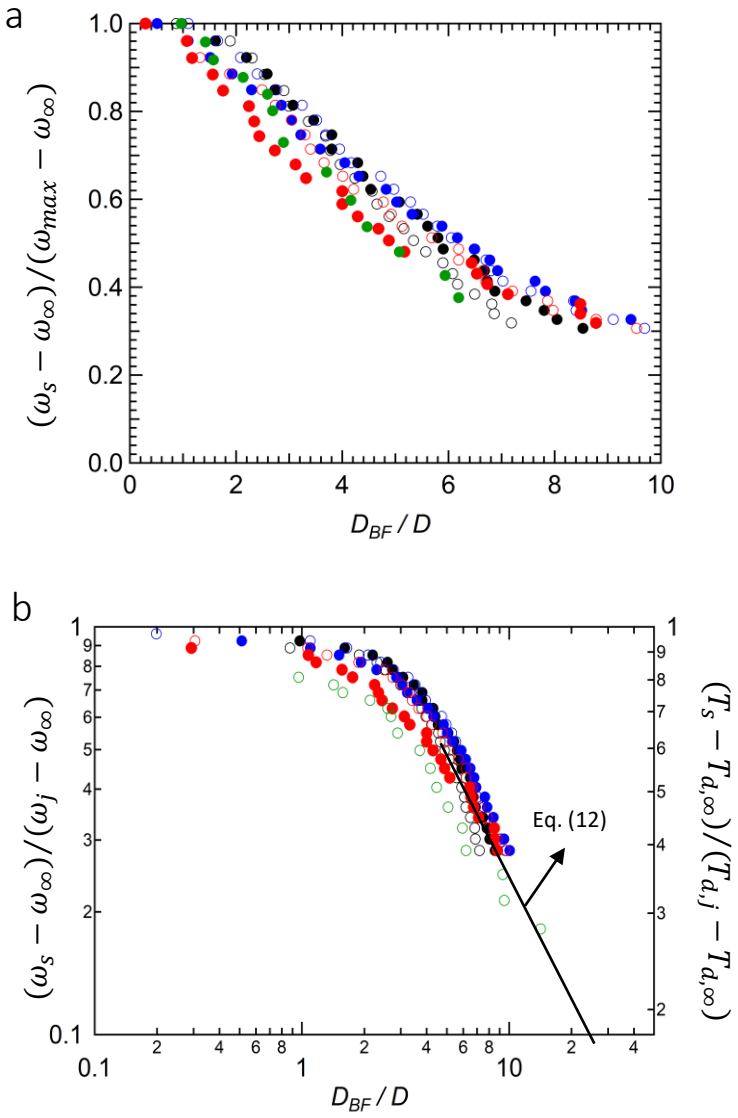

Figure C.1: Laminar jet experimental results. **a.** Dimensionless concentration distribution on the surface as a function of dimensionless radial distance (D_{BF}/D). Colour and shape coding correspond to Figure 1(b). **b.** plot of nondimensional vapor mass fraction and surface dew-point temperature with respect to the extent of BF spot circle.

Table C.1: Leading constant results from curve fitting of BF spot diameter, see equation (6) and equation (12).

H/D	Re_j	$(a_v + a_\omega)/\sqrt{2a_v}$	C_4	H/D	Re_j	$(a_v + a_\omega)/\sqrt{2a_v}$	C_4
3.33	500	2.97	1.08	10	500	9.23	1.38
3.33	1340	2.97	1.04	10	1340	6.03	1.23
3.33	2230	2.60	0.96	10	2230	4.27	1.11
3.33	3120	2.73	1.04	10	3120	4.03	1.12
3.33	4130	2.73	1.05	10	4130	4.5	1.18
5	500	4.63	1.29	11.67	500	10.37	1.24
5	1340	4.10	0.99	11.67	1340	6.10	1.20
5	2230	3.17	1.03	11.67	2230	4.73	1.07
5	3120	3.30	1.08	11.67	3120	4.47	1.11
5	4130	3.47	1.10	11.67	4130	4.73	1.11
6.67	500	6.17	1.40	15	500	11.3	1.04
6.67	1340	4.20	1.20	15	1340	6.73	1.21
6.67	2230	3.50	1.11	15	2230	4.80	0.77
6.67	3120	3.83	1.10	15	3120	5.10	0.92
6.67	4130	4.03	1.10	15	4130	5.43	0.96
8.33	500	7.70	1.46				
8.33	1340	5.03	1.27				
8.33	2230	3.73	1.14				
8.33	3120	4.13	1.11				
8.33	4130	4.37	1.11				

C.1 Reproduction of Recovery Temperature Derivation

In these pages, I replicate the work of Hollworth and Gero (1985) [28]. Because this work is essential to understand the derivation of BF spots discussed in Chapter 5. We start by postulating that as a jet impinges on an adiabatic solid surface, the surface temperature is going to correspond to a recovery temperature (T_r). Further, the dynamic of the flow in the wall jet region consists of two layers on top of each other. The lower layer behaves similar to an ordinary boundary layer problem with a characteristic velocity (v^*). This velocity coincides with the maximum velocity profile in the wall jet region in Figure 2.4. The upper layer can be treated as a free jet. This analysis was followed by Glauert [163] and Poreh et al. [164]. Following the analysis of the latter, the characteristic velocity is given as

$$\frac{v^*}{v_j} = C_1 \left(\frac{H}{D}\right)^{0.1} \left(\frac{r}{D}\right)^{-1.1} \tag{C.1}$$

It was also concluded that the thickness of the inner layer varies almost linearly with the radial location as

$$\frac{\delta}{D} = C_2 \left(\frac{H}{D}\right)^{-0.1} \left(\frac{r}{D}\right)^{0.9} \tag{C.2}$$

Applying an energy balance on a jet that exists at a temperature ($T_j \neq T_\infty$) and impinges on an adiabatic surface results in

$$\int_0^{\delta} v(T_o - T_\infty)(2\pi r)dy = \dot{V}(T_j - T_\infty) \tag{C.3}$$

It is noticed that both density and specific heat are assumed constants. The volume flow rate emanating from the nozzle exit is given as

$$\dot{V} = \frac{\pi}{4} D^2 v_j \tag{C.4}$$

Substituting in Eq.C.3 and normalizing with the recovery temperature difference $(T_r - T_\infty)$ and the characteristic velocity gives

$$r\delta(T_r - T_\infty)v^* \int_0^1 \left(\frac{v}{v^*}\right)\left(\frac{T_o - T_\infty}{T_r - T_\infty}\right)\frac{dy}{\delta} = \frac{D^2 v_j}{8}(T_j - T_\infty) \tag{C.5}$$

If one assumes that both dimensionless velocity and temperature distributions to be self similar, then the integral would reduce to a constant. Substituting Eq.C.1 and Eq.C.2 into Eq.C.5 and lumping the constants yield

$$\frac{T_r - T_\infty}{T_j - T_\infty} = C_3 \left(\frac{H}{D}\right)^{-0.1} \left(\frac{r}{D}\right)^{-0.9} \tag{C.6}$$

Experimental verification of this behaviour over Reynolds numbers of 7000 to 70,000 was performed. Results matched quite well with minor deviations. The leading constant was found to be around unity.

C.2 Numerical model development

In this section, we utilize the finite volume method (FVM) to obtain the recovery concentration at various conditions. As was concluded in the paper, BF spots are manifestations of the recovery concentration concept. Therefore, impingement of humid air jet on an adiabatic surface is simulated. The geometrical domain as well as the boundary conditions are depicted in Fig.C.2a. The problem is reduced to an axisymmetric problem around an axis, at which no gradient in state variables is present in the radial direction. The jet originates from an inlet section of uniform velocity, temperature, and concentration profiles. The humid air flows through a tube of a length greater than the entry region to ensure fully developed conditions at the tube exit. The jet exits the tube into an ambient condition of given temperature, pressure and concentration preset to the outlet surfaces depicted in Figure C.2a. The impingement surface as well as the tube surface are characterized by zero heat and mass fluxes. The no-slip condition is applied to both surfaces as well. The flow of the humid air jet is assisted by gravitational force which acts normal to the impingement surface. The governing equations in the solution domain are given as

$$\nabla \cdot (\rho \overrightarrow{v}) = 0 \tag{C.7}$$

$$\nabla \cdot (\rho \overrightarrow{v}\,\overrightarrow{v}) = -\nabla P + \nabla \cdot \overline{\overline{\tau}} + \rho \overrightarrow{g} \tag{C.8}$$

$$\nabla \cdot (\overrightarrow{v}(\rho E + P)) = \nabla \cdot (k \nabla T - \sum_{j} h_j \overrightarrow{J_j}) \tag{C.9}$$

$$\nabla \cdot (\rho_j \overrightarrow{v}) = -\nabla \cdot \overrightarrow{J_j} \tag{C.10}$$

where $E \approx h$ neglecting pressure work and kinetic energy. The total enthalpy is a mass weighted average of each species enthalpy. The species enthalpy is given by equation (C.11).

$$h_j = \int_{T_{ref}}^{T} c_{p,j} dT \tag{C.11}$$

The term $\overrightarrow{J_j}$ in equation (C.9) and equation (C.10) refers to the diffusive mass flux of each species which is given by Fick's law.

$$\overrightarrow{J_j} = -D_{j,i} \nabla \rho_j \tag{C.12}$$

In order to take care of turbulence, standard $k - \omega$ model was implemented. Adding perturbed state variables to equations (C.7-C.10), yields the extra term of Reynolds stress ($\rho \overline{u_i' u_j'}$). The standard $k - \omega$ model solves for two additional equations representing the transport of turbulent kinetic energy (k) and specific rate of dissipation (ω). Enough documentation can be found in many references, therefore are not repeated here [156, 157]. The differential equations are solved using an FVM in which the domain is discretised into smaller cells as in Fig. C.2b. Finer meshing was concentrated where the change in state variables is expected to be greatest. It is worth noting that a separate simulation was performed on a free unbounded jet for comparison purposes.

Figure C.3 presents the contour plots of vapor mass fraction at varying standoff-to-diameter ratios while Fig. C.4 presents those of different Reynolds numbers. We observe that vapor concentration is maximum in

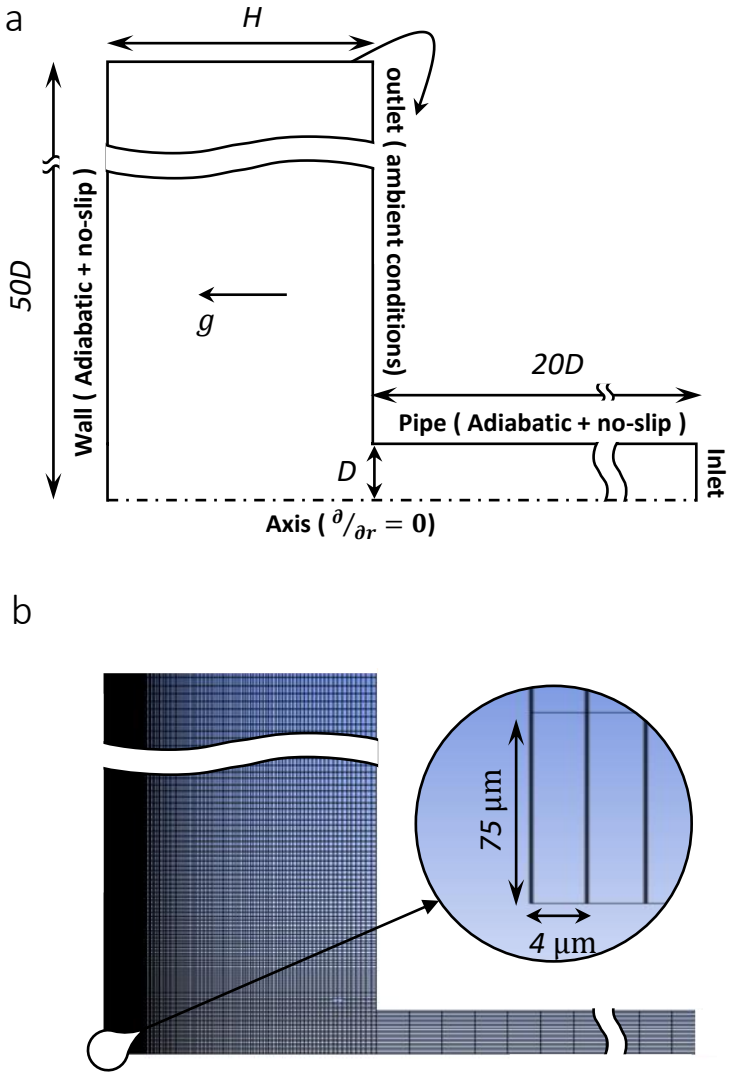

Figure C.2: Geometrical configuration of the numerical model. **a.** geometrical model of the axissymetric problem under simulation using FVM. **b.** Refined meshing of the solution domain.

the core of the jet. As the jet advances in the ambience, its vapor content diffuses and the uniform concentration tends to transition smoothly near the perimeter of the jet. Figure C.3 shows that for jets with heights that are 8.33 diameters or less, the maximum vapor concentration coincides with that of the inlet. The maximum vapor concentration then starts to drop due to the diffusion effect with ambience. From Fig. C.4, we notice that for Reynolds numbers of 1340 and higher, there is no significant difference of the vapor concentration profiles. The case of Reynolds of 500 shows slightly higher throw of vapor content. This could be attributed to the low mixing characteristic of laminar flows, therefore, maintaining its vapor content for a longer distance. For all the presented cases, the introduction of a wall normal to the jet flow direction does not seem to change the flow upstream. Therefore, further insights of the maximum vapor concentration at the wall could be obtained from a free jet case corresponding to similar geometric and flow conditions. This conclusion was the basis of the derivation of equation (6) in the main manuscript.

Figure C.5 depicts the vapor mass fraction normalized with the jet excess vapor mass fraction. We observe that within a radial location ($D_{BF}/D \leq 5$ (impingement region), the value corresponds to the maximum vapor mass fraction and is invariant with the radial location. Whereas for greater radial locations (wall jet region), there is almost a linear drop of the normalized vapor mass fraction. The effect of standoff-to-diameter ratio is negligible while the effect of Reynolds number is absent for the case of turbulent jets ($Re \geq 1340$). These conclusions are in line with our scaling analysis given in equation (6) and equation (13). Contrasted with Fig. 4, we observe a

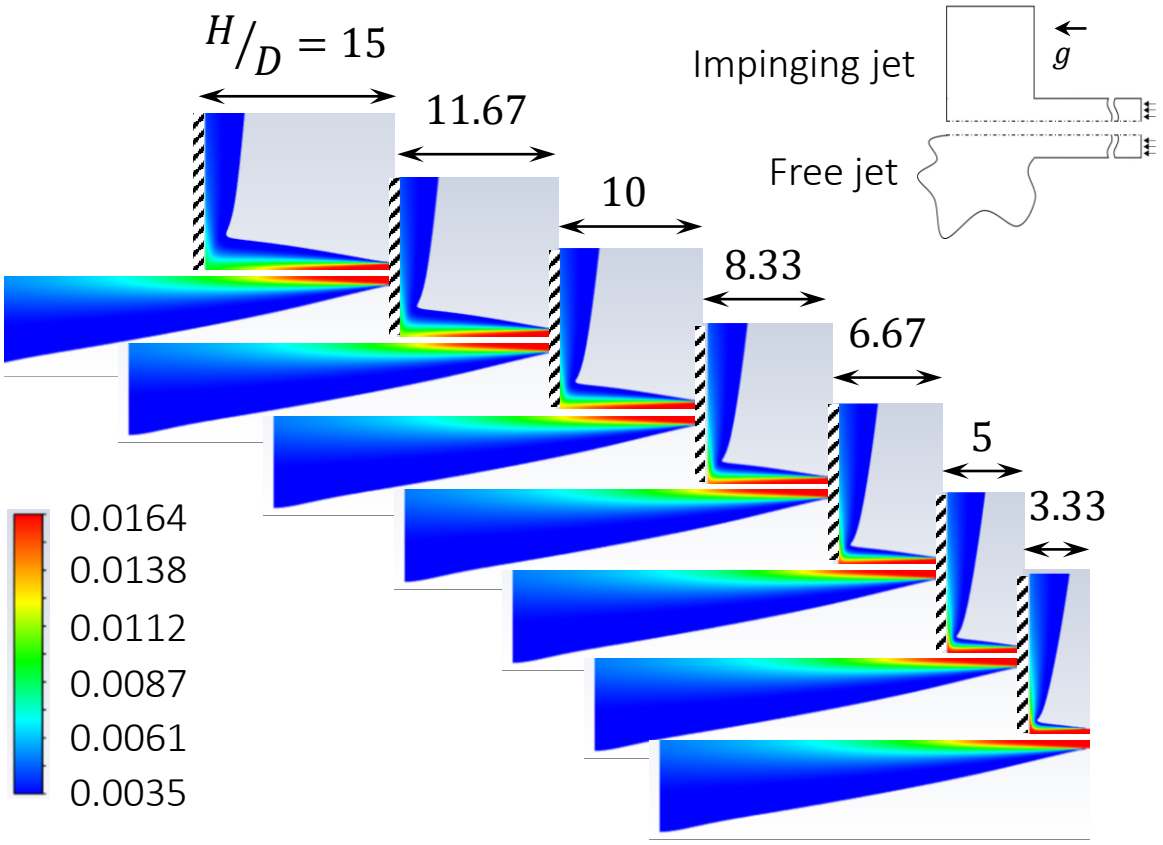

Figure C.3: Results of different standoff-to-diameter ratios. Contours of vapor mass fraction at H/D of 3.33, 5, 6.67, 8.33, 10, 11.67, and 15 (from right to left). Results are for a selected Reynolds number of 4130. At each standoff-to-diameter ratio two cases are presented; (top contour plot) represents the case were a jet impinges on a wall corresponding to a given H/D; (bottom contour plot) represents the case of a free unbounded jet at a similar flow and geometric conditions.

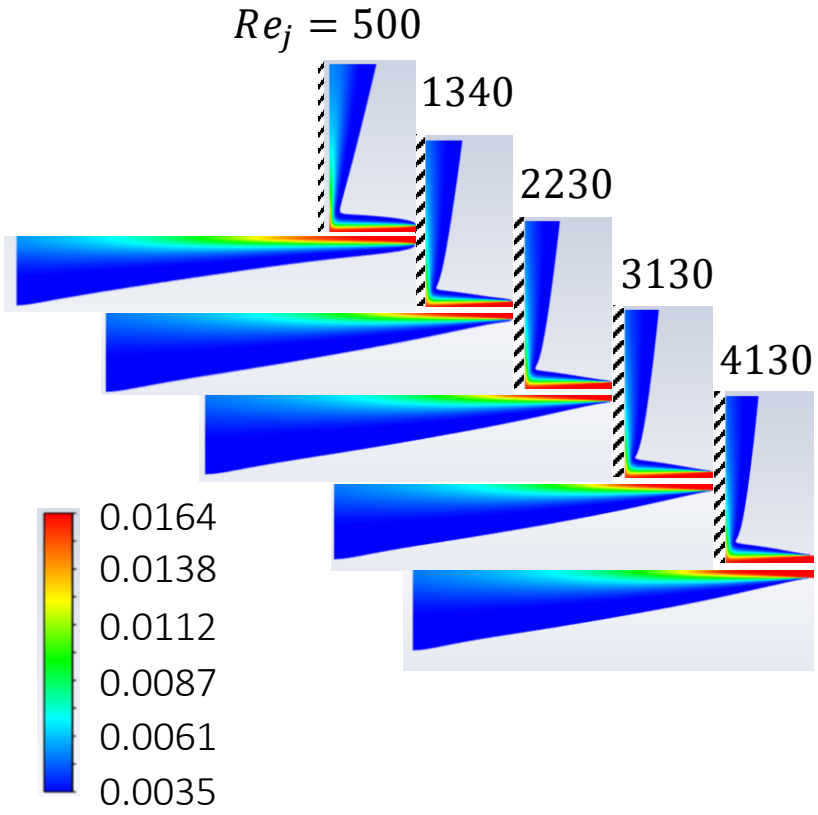

Figure C.4: Results of different Reynolds numbers. Contours of vapor mass fraction at Re_j of 500, 1340, 2230, 3120, and 4130. Results are for a selected standoff-to-diameter ratio of 6.67. At each value of Re_j, two cases are presented; (top contour plot) represents the case were a jet impinges on a wall corresponding to the given Re_j; (bottom contour plot) represents the case of a free unbounded jet at a similar flow and geometric conditions.

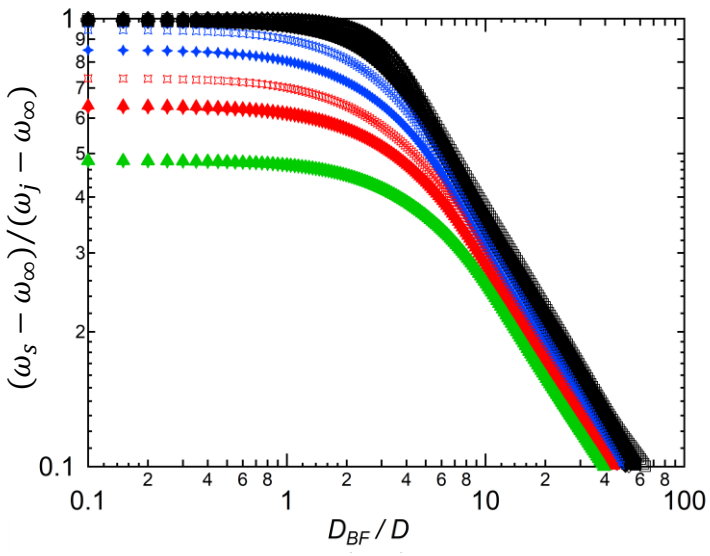

Figure C.5: Nondimensional recovery concentration. plot of nondimensional vapor mass fraction with respect to the extent of BF spot circle.

the obvious resemblance of the behaviour with a minor over-estimation by the numerical model.

C.3 Validity of constant mixture density assumption

It is seen that equation (2) of the main manuscript presents the momentum conservation in the free jet region. Because the jet issuing from the pipe is at the same temperature as the ambience, we do not expect the density to vary with temperature. It remains to be determined if the dilution of water vapor causes significant density variation along the radial location at a given standoff distance.

Here, we refer to a conventional thermodynamic relation governing the air-vapor mixture density (ρ) which is given as follow.

$$\rho = \frac{P_a M_a + P_v M_v}{RT} \tag{C.13}$$

where P_a, P_v are partial pressure of air and vapor, respectively, M_a, and M_v are molecular weights of air and vapor, respectively, R is the universal gas constant and T is the ambient temperature. The total pressure is that corresponding to ambience $P = P_a + P_v$. The vapor partial pressure can be related to the relative humidity (RH) by the following relation.

$$P_v = RH \times P_{sat} \tag{C.14}$$

The saturation pressure can be obtained from steam tables or approximated by the Antoine equation as follows.

$$log_{10}(133.322 P_{sat}) = (8.07131 - \frac{1730.63}{233.426 + T}) \tag{C.15}$$

In Fig.C.6, we illustrate the variation of air-vapor mixture density with state variables, namely ambient temperature, pressure and relative humidity. Because we ruled out any density variation due to temperature change, Fig.C.5a suggests that the ambient temperature should be below 60 ^{o}C so that vapor dilution in the radial direction does not introduce more than 10% density variation. Also, it should be below 50 ^{o}C to reduce the density variation below 5 %. Beyond 60 ^{o}C, the mixture becomes rich in water vapor resulting in a high variability with relative humidity (or water vapor concentration in other words). It is worth mentioning that Fig.C.5a is plotted for P=1 atm. The experiment done in this paper are shown as the circled cross point, where the assumption is clearly valid. In Fig.C.5b, we re-plot the mixture density at lower system pressure namely 0.5 atm. We notice that the density variability with vapor dilution becomes significant at a lower temperature compared to 1 atm pressure case. This is clearly because of the lower saturation temperature corresponding to the ambient pressure.

Based on the above discussion, we infer that the assumption of constant mixture density is valid as long as the temperature is much lower than the saturation temperature corresponding to the system pressure. Typical humid air experiments are done in atmospheric ambience, therefore, a temperature below 60 ^{o}C is acceptable for Eq.2 to be valid.

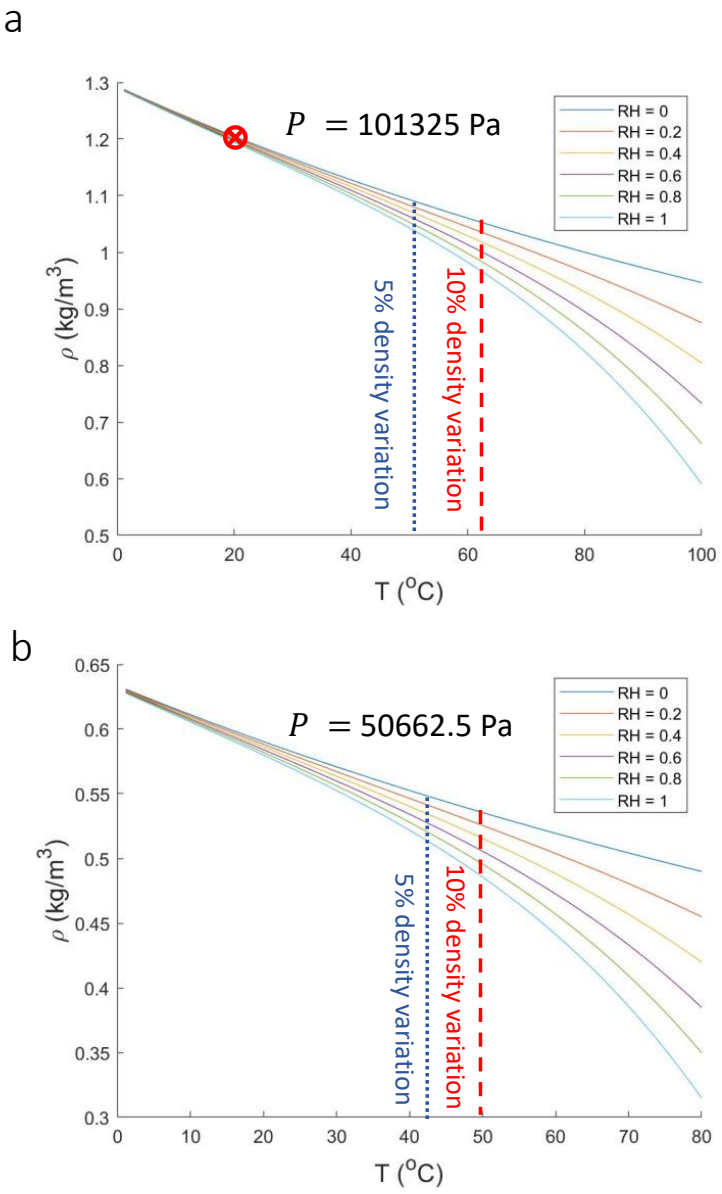

Figure C.6: Illustration of air-vapor mixture density as a function of ambient temperature at different relative humidities at (a) $P = 101325$ Pa and (b) $P = 50662.5$.

APPENDIX D

Supplementary Material for Chapter 5

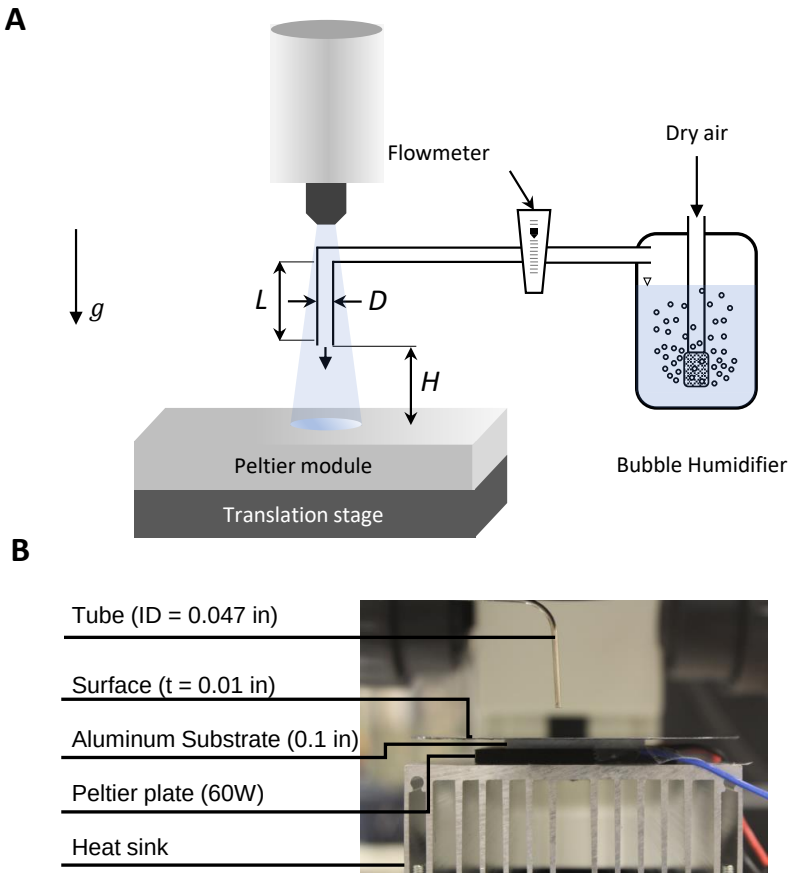

Figure D.1: Continuous Drop-wise Condensation experimental setup. **A.** A schematic of CDC illustrating the general setup for condensation experiments. Dry air is bubbled into a room-temperature pool of DI water through several spargers (one is shown for illustration). The different parameters are discussed in the method section. **B.** A side view of the condensation surface assembly.

D.1 Heat Transfer of water Vapor Condensation with Humid Air Jet Impingement

The previous section utilized a theoretical approach to understand and quantify the heat flux to a condensation surface in the case of pure vapor condensation, i.e. no air involved. Hence, this section is dedicated to model the problem of air existence. It has been shown that the existence of minute amounts of non-condensable gases (NCG), such as air reduces the condensation rate, and thus the heat flux, tremendously. This is due to the fact that at steady state conditions, a diffusion layer builds on top of the condensate formed on the surface. The condensation of vapor becomes mainly dominated by the mass diffusion through this layer. The thermal resistance of this layer dominates the heat transfer to the surface, therefore, Eq. D.15 is not valid to describe the system. The heat transfer from the surrounding through the droplet to the condensation surface can be estimated simply as.

$$q''(r) = \dot{m}'' h_{fg} + h(T_\infty - T_s) \tag{D.1}$$

where the mass flux to the surface can be written as

$$\dot{m}'' = \frac{\phi Sh \rho D_{ij}}{D} \left(\frac{\omega_{v,\infty} - \omega_{v,o}}{1 - \omega_{v,o}} \right) \tag{D.2}$$

where the suction effect factor is written as

$$\phi = \frac{1 - \omega_{v,o}}{\omega_{v,o} - \omega_{v,\infty}} ln \left(\frac{1 - \omega_{v,\infty}}{1 - \omega_{v,o}} \right) \tag{D.3}$$

The heat transfer coefficient can be written as

$$h = \frac{Nuk}{D} \tag{D.4}$$

Sherwood and Nusselt numbers for jet impingement can be obtained by utilizing heat/mass transfer analogy along with the correlation usually used for single round jets [13, 5].

$$\frac{Sh}{Sc^{0.42}} = \frac{Nu}{Pr^{0.42}} = G(A_r, \frac{H}{D})[2Re^{1/2}(1 + 0.005Re^{0.55})^{1/2}] \tag{D.5}$$

where

$$G = \frac{1 - 1.1D/r}{1 + 0.1(H/D - 6)D/r}\frac{D}{r} \tag{D.6}$$

In Fig.5.4B, we show the resulting heat and mass fluxes for the case of a saturated humid air jet impinging on a cold surface at varying jet parameters. The inputted parameters in the correlation are; saturated environment at $T_\infty = 22^o$C and T_s=15^{o}C at P=1 atm. The nozzle diameter is 1 mm located at varying distance. The impingement area is is confined withing 2.5 mm.

D.2 Calculation of compactness factor of different state-of-the-art condensers

For a condenser existing in humid air environment, one can write the heat transfer to the surface as follows

$$q = hA(T_\infty - T_s) \tag{D.7}$$

where h is the heat transfer coefficient, A is the exposed surface area, T_∞ and T_s are the ambient and surface temperatures, respectively. Similarly, the mass transfer (condensation rate) can be written as follows

$$\dot{m} = h_m A(\omega_\infty - \omega_s) \tag{D.8}$$

where h_m is the mass transfer coefficient, ω_∞ and ω_s are the ambient and surface vapor mass fraction, respectively. The relation between h and h_m can be inferred from heat/mass transfer analogy as

$$\frac{h}{h_m} = \frac{Nu}{Sh}\frac{k}{\rho D} = \frac{CRe^n Pr^m k}{CRe^n Sc^m \rho D} \approx \left(\frac{Pr}{Sc}\right)^{1-m} C_{pa} = Le^{1-m} C_{pa} \tag{D.9}$$

The value of the exponent (m) depends on the correlation being used. For instance, for a laminar boundary layer over a flat plate, a value of (1/3) is used[203]. In our case, the correlation given by Eq.D.5 is characterized by an exponent of (0.42).

For comparison of the current method of condensation with other condensers/dehumidifiers, we think CDC provides an extremely compact con-

denser. Therefore, we compare the different state-of-the-art condensers by a compactness factor which is given by the following relation

$$C_h = \frac{hA}{V} \tag{D.10}$$

$$C_m = \frac{h_m A}{V} \tag{D.11}$$

where C_h and C_m are the compactness factor of heat and mass transfer exchangers, respectively. The higher the value indicates a higher transfer rate per unit driving potential (temperature or vapor mass fraction) per unit volume. In Fig.5.4A, we show a comparison of the compactness factor for different dehumidifiers along with the current method. We reconstruct the results published by Sadeghpour et al. [150].

D.3 Heat Transfer of Pure Vapor with Jet Impingement

In this section, an estimate of the heat transfer of DWC of pure vapor is presented. We utilize the theoretical model developed originally by Rose and coworkers [9]. The process of DWC can be summarized by the following sequence of events; initial nucleation of vapor clusters, droplet growth by condensation on the interface, droplet growth by coalescence, droplet fall off, and finally re-nucleation of droplets.

The first process of DWC is heterogeneous condensation over active nucleation sites on the condensation substrate. The active nucleation site density (N_s) depends on surface topography, Fluid's thermophysical properties, and subcooling degree [215, 216]. The value of active nucleation site density is in the range of 10^9-10^{15} m^{-2} [217]. For the purpose of obtaining an approximate comparison between jet- and gravity-assisted shedding mechanisms, we choose a value for $N_s = 10^{12}$ m^{-2}. The smallest stable droplet formed by condensation in the nucleation site is given as [186, 217]

$$r_{min} = \frac{2T_{sat}\gamma}{\rho_l h_{fg}(T_{sat} - T_s)} \tag{D.12}$$

where T_{sat}, γ, ρ_l, h_{fg}, T_s as saturation temperature, surface tension, liquid density, latent heat of vaporization, and surface tension, respectively. It has been shown experimentally that droplets in the range $[r_{min}, r_e]$ grow by direct condensation only, where the effective radius results from geometrical argument as $r_e = 1/\sqrt{4N_s}$. Droplets with radii higher than the effective ra-

dius grow by direct condensation on their surfaces as well as by coalescence with neighboring droplets. DWC on vertical surface, i.e. typical configuration, are characterized by the existence of a maximum droplet radius of which droplets start sliding on the surface and consequently sweeping smaller droplets in their path. A balance between the weight of the droplet and the surface retention force results in the following relation of maximum radius for gravity-assisted shedding [175]

$$r_{max,g} = \sqrt{\frac{6\gamma \sin\theta(\cos\theta_r - \cos\theta_a)}{\pi\rho_l g(2 - 3\cos\theta + \cos^3\theta)}} \tag{D.13}$$

where θ, θ_r, θ_a are the static, receding and advancing contact angles respectively and g is the gravitational acceleration. To estimate the overall heat transfer rate to the condensation surface, several researchers have utilized the theory developed by Rose and co-workers [9]. The model is centered around correlating the heat transfer across a single droplet to the overall heat transfer across the entire droplets on a surface. The following formula is usually considered for the overall heat transfer rate

$$q'' = \int_{r_{min}}^{r_e} q_d(r,\theta) n(r,\theta) dr + \int_{r_e}^{r_{max}} q_d(r,\theta) N(r,\theta) dr \tag{D.14}$$

where $q_d(r,\theta)$, $n(r,\theta)$ and $N(r,\theta)$ are the heat transfer through a single droplet of radius (r), the *small* droplet size distribution in the range $[r_{min}, r_e]$, and *large* droplet size distribution in the range $[r_e, r_{max}]$, respectively. The detailed derivation of the individual parameters has been discussed in several papers beginning with the work of Rose [9].

The heat transfer across a single droplet of radius (r) can be represented as a combination of Laplace pressure effect due to curvature, liquid-vapor interfacial thermal resistance (Knudsen layer), conduction through the droplet body, and conduction through the condensation surface. heat transfer across a single droplet can be written as [8]

$$q_d(r,\theta) = \pi r^2 (T_{sat} - T_s - \frac{2T_{sat}\gamma}{\rho_l h_{fg} r})(\frac{1}{2h_i(1-\cos\theta)} + \frac{r\theta}{4k_l \sin\theta} + \frac{\delta_s}{k_s \sin^2\theta})^{-1} \tag{D.15}$$

where k_l and k_s are the thermal conductivity of the liquid and the condensation surface, respectively and δ_s is the thickness of the condensation surface. The liquid-vapor interfacial heat transfer coefficient is given as [218]

$$h_i = \frac{2\sigma_c}{2-\sigma_c}\sqrt{\frac{M}{2\pi R T_s}}\frac{h_{fg}^2 \rho_v}{T_s} \tag{D.16}$$

where $sigma_c$, M, R and ρ_v are the condensation coefficient, molecular weight of water, gas constant, and water vapor density, respectively. The size distribution of large droplets was derived experimentally and mathematically as [204, 219]

$$N(r,\theta) = \frac{1}{3\pi r_{max} r^2}\left(\frac{r}{r_{max}}\right)^{-2/3} \tag{D.17}$$

Lastly, the population balance theory was used to derive the small droplet size distribution [220]. The form is given as

$$n(r,\theta) = \frac{1}{3\pi r_{max} r_e^3}\left(\frac{r_e}{r_{max}}\right)^{-2/3}\frac{r(r_e - r_{min})}{r - r_{min}}\frac{A_2 r + A_3}{A_2 r_e + A_3}\exp\left(B_1 + B_2\right) \tag{D.18}$$

where the constants are given as

$$A_1 = \frac{(T_{sat} - T_s)}{2\rho_l h_{fg}}, \tag{D.19a}$$

$$A_2 = \frac{\theta(1 - \cos\theta)}{4k_l \sin\theta}, \tag{D.19b}$$

$$A_3 = \frac{1}{2h_i} + \frac{\delta_s(1 - \cos\theta)}{k_s \sin^2\theta} \tag{D.19c}$$

$$A_4 = \frac{A_2}{\tau A_1}\left[\frac{r_e^2 - r^2}{2} + r_{min}(r_e - r) + r_{min}^2 \ln\left(\frac{r_e - r_{min}}{r - r_{min}}\right)\right] \tag{D.19d}$$

$$A_5 = \frac{A_3}{\tau A_1}\left[r_e - r + r_{min} \ln\left(\frac{r_e - r_{min}}{r - r_{min}}\right)\right] \tag{D.19e}$$

$$\tau = \frac{3r_e^2(A_2 r_e + A_3)^2}{A_1[8A_3 r_e - 14A_2 r_e r_{min} + 11A_2 r_e^2 - 11A_3 r_{min}]} \tag{D.19f}$$

Equations D.12 through D.19 along with known thermophysical properties provide a complete set of equations to obtain the overall heat transfer rate to a surface. For instance, Fig.D.2 shows the heat flux variation on a surface with different wettability, i.e. contact angles, under gravity-assisted droplet shedding. In the figure, we also show the maximum radius of droplets being shed by the assistance of body weight. For a surface with static contact angle of 90^o, we notice that a heat flux of 30 kW/m^2 could be transferred to the surface with a maximum droplet radius of 390 microns. With higher contact angle surfaces, droplets of lower radius could be shed. However, due to the increased conduction resistance, heat flux drops beyond a contact angle of 145^o.

In Fig.D.3, we show for a constant static contact angle, the effect of varying the maximum droplet radius. The cross symbols in the figure represent the case of gravity-assisted droplet shedding as their respective static

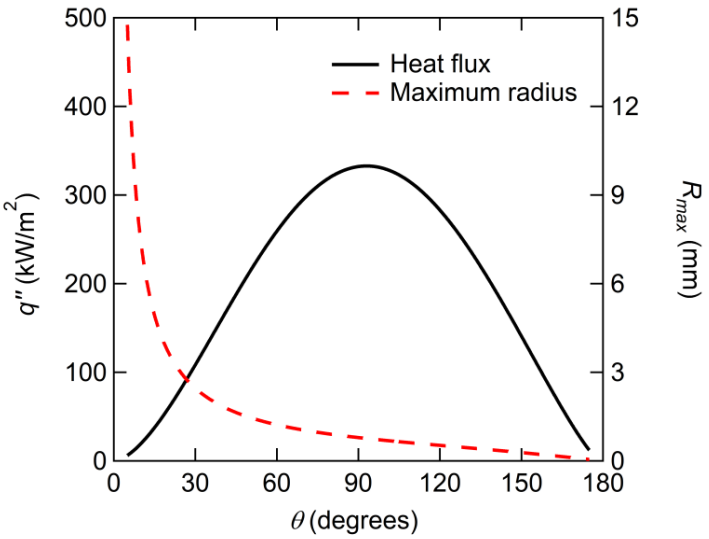

Figure D.2: Heat flux to a vertical surface exposed to pure vapor analytically evaluated at different static contact angles with gravity-assisted shedding. The parameters inputted into the model are; T_{sat}=22^{o}C, T_s=15^{o}C, δ_s = 254μm, k_s=100W/m^{2}K, N_s=10^{12} sites/m^2, σ_c=1, and $\theta_A - \theta_R$=5^o.

contact angles. For instance, the heat flux to a surface could be enhanced by 150% if a coating with static contact angle of 160^o is used with a maximum droplet radius of around 20 micron compared with the hydrophilic surface and gravity-assisted case.

We believe that with CDC, the mechanism of droplet growth would be similar to that of regular drop-wise condensation with the maximum droplet radius determined by the jet impingement shedding action. Therefore, in Fig.5.4D we normalize the heat flux and maximum droplet radius with with their respective values due to gravity-assisted drop-wise condensation.

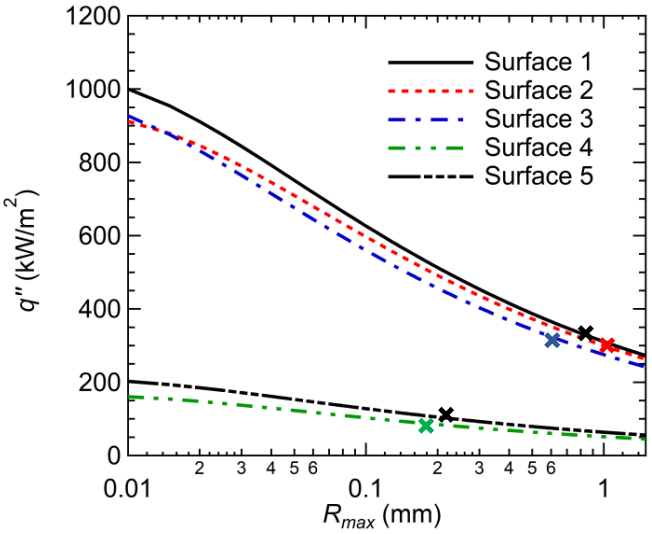

Figure D.3: Heat flux to a vertical surface exposed to pure vapor analytically evaluated at maximum droplet Radii for the different tested surfaces. The cross symbol represents the value obtained with gravity-assisted shedding. The parameters inputted into the model are similar to that in Fig.D.4 for meaningful comparison.

D.4 Discussion of drag force quantification

As observed in (Fig.5.1 and Fig.5.2 of main manuscript), the initial droplet shedding occurs withing the stagnation region, i.e. almost within a tube radius from the stagnation point. It is well established that for the case of laminar non-mixing gas jet impingement, the similarity solution of Navier-Stokes equations gives a constant momentum boundary layer thickness in the impingement region. The equation of the boundary layer thickness is usually written as $\delta_o \sim \sqrt{\nu D/u_j}$, where ν is the kinematic viscosity of the jet, D is the diameter of the tube exit, and u_j is the speed of the jet at the standoff distance [26, 221]. In this work, the jet Reynolds number was in the range of 1000-6000, therefore, the momentum boundary layer thickness should be below the range of 15 - 35 μm, respectively. Even though these estimations are for laminar jets ($Re < 1000$), turbulent mixing, like in our experiments, results in a lower boundary layer thickness. Our observations of droplets size show that the boundary layer thickness is smaller than the smallest droplet being shed. Therefore, we expect that the flow field withing the boundary layer is unimportant.

In general, the drag force on the droplet due to the jet flow can be given by equation 7. The projected area shape factor Γ_A can be obtained geometrically as

$$\Gamma_A = \theta - \frac{1}{2}\sin 2\theta \tag{D.20}$$

The drag coefficient based on the jet speed and droplet diameter is in the range of 1-0.6 for Reynolds numbers of 100-500, respectively. These values were obtained from spherical relations for the lack of better quantification in

the literature, however it is a common practice. The effective velocity term is taken to equal the jet mean velocity value multiplied by a proportionality constant, i.e. $u_o = av_j = Q/A_{tube}$.

D.5 Droplet equation of motion: simplistic approach

In this section, we present a simplistic equation of motion that represents a one-dimensional force balance on a single droplet. In Fig.D.4A, we show the simplified physical model of a droplet with diameter (D) and contact angle (θ) located at a distance (x_o) from the center of impingement region. The jet issues from a tube that is located at a standoff distance (H) with a mean velocity (v_j). The only forces responsible for droplet movement are drag force (F_d), surface tension force (F_s), and viscous friction force (F_v) (Fig.D.4B). Newtons seconds law is applied to the droplet as follows.

$$\rho_l \Gamma_v \frac{d(D^3 v)}{dt} = \frac{1}{8} C_d \rho_g \Gamma_A (u_o - v)^2 D^2 - \Gamma_L D\gamma(\cos\theta_R - \cos\theta_A) - \eta \Gamma_{base} R^2 \left.\frac{\partial v}{\partial y}\right|_{base} \tag{D.21}$$

where ρ_l is the density of condensate liquid, v is the local velocity of the droplet, Γ_v is the volumetric shape factor, η is the dynamic viscosity, Γ_{base} is the shape factor of the base area of the drop. At the onset of droplet motion, only the drag and surface tension forces are present. Equation 8 in the main manuscript is the resultant of the force balance. In the accelerating droplet region (Period II), the drag force becomes significantly higher than the retention forces. Hence, Eq.D.21 is reduced to the following.

$$\rho_l \Gamma_v \frac{d(D^3 v)}{dt} = \frac{1}{8} C_d \rho_g \Gamma_A (u_o)^2 D^2 \tag{D.22}$$

This equation suggests a negligible effect of surface wettability on droplet motion in regions corresponding to Period II. This is clear from the droplet apparent velocity shown in Fig.5.6D. In the decelerating period (Period

III), Eq.D.21 should be fully used. However, because of the complexity of determining the coefficients in the equation, presenting an outline of the equation is sufficient.

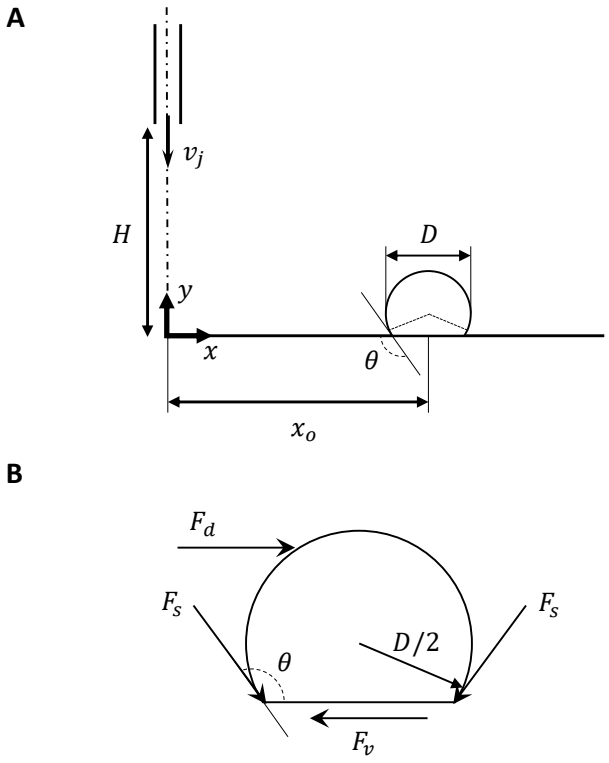

Figure D.4: Physical model for writing the equation of motion of a single droplet in contact with flow of an axisymmetric jet. **A.** one-dimensional schematics of the pertaining parameters. **B.** Forces acting on a single droplet under a generalized case of a moving droplet.

D.6 Videos

Video 5.1 10-second Condensation process on surface 1 (hydrophilic Silicon surface) at different jet Reynolds numbers. The experimental conditions are as indicated in the method section while surface characteristics are as in Table 1.

Video 5.2 10-second Condensation process on surface 2 (hydrophilic silicon surface with high contact angle hysteresis) at different jet Reynolds numbers. The experimental conditions are as indicated in the method section while surface characteristics are as in Table 1.

Video 5.3 10-second Condensation process on surface 3 (hydrophobic Silicon surface) at different jet Reynolds numbers. The experimental conditions are as indicated in the method section while surface characteristics are as in Table 1.

Video 5.4 10-second Condensation process on surface 4 (superhydrophobic silicon surface with high contact angle hysteresis) at different jet Reynolds numbers. The experimental conditions are as indicated in the method section while surface characteristics are as in Table 1.

Video 5.5 10-second Condensation process on surface 5 (superhydrophobic silicon surface with negligible contact angle hysteresis) at different jet Reynolds numbers. The experimental conditions are as indicated in the method section while surface characteristics are as in Table 1.

Video 5.6 Illustration of droplet jumping on surface 5 (superhydrophobic silicon surface with negligible contact angle hysteresis).

APPENDIX E

Calibration and Uncertainty Analysis

E.1 Calibration of Measurement Sensors

In this work, we utilized several measuring instruments. For temperature readings, we used k-type thermocouples, a resistance temperature detector (RTD) element, and Infrared (IR) camera. We also used a hygrometer to measure the relative humidity of ambience as well as the vapor jet exiting the tube prior to impingement. In the following paragraphs, we summarize our calibration experiments and results.

The calibration of the k-type thermocouples as well as the RTD element were performed simultaneously. Initially, all sensors were placed in a well mixed ice-liquid DI water mixture to set the 0^oC point. To ensure this reading, a liquid-in-glass (LIG) thermometer was used for cross checking. Following this step, the sensors and the LIG thermometer were place inside a water bath that was uniformly heated/cooled. The thermal bath was provided with an internal circulation to ensure well mixing and temperature uniformity. In table E.1, we summarize the result of the temperature calibration experiments. It was concluded that all the sensors report the temperature to an accuracy of 0.6^oC.

Table E.1: Calibration of temperature sensors.

Sensor	Pnt1	Pnt2	Pnt3	Pnt4	Pnt5	Pnt6	Pnt7
Liquid in glass	21	18	16	14.5	13	11	0
RTD element	20.95	18.05	16.15	14.4	13.0	11.00	0.15
Thermocouple 1	20.7	18.6	16.5	14.7	13.2	11.6	-0.2
Thermocouple 2	20.6	18.4	16.4	14.6	13.3	11.4	0.1
Thermocouple 3	20.7	18.1	16.1	14.3	13.1	11.1	0.1

The IR camera was calibrated by the manufacturer with an accuracy of 1 ^{o}C. The following procedure was followed prior to each experiment to determine the surface emissivity and environmental reflected temperature. To determine a good estimate of the environmental reflected temperature, a crumbled aluminum foil was placed and a focused image was captured. The mean temperature of the foil is taken as the required parameter. To determine the emissivity of any surface, a black thin tape ($\varepsilon \sim 1$) was placed on the required surface. The temperature reading was recorded as the actual surface temperature. Then, the tape was removed and the emissivity was manually decreased until the same temperature was reached. An emissivity of nearly unity was observed for the condensate droplets. The Si surfaces were observed to have an emissivity of 0.5-0.55, while the Aluminum surface (Aluminum oxide) have an emissivity of 0.25-0.3.

Two hygrometers were used to report the relative humidities of the environment and the humidified air exiting the tank. The former hygrometer was calibrated by the manufacturer. The reported relative accuracy of the calibrated hygrometer was $\pm$2%. The other hygrometer was a wet bulb thermometer that was made in-house. This hygrometer was placed inside the water tank above the water level. A wicking cloth was wrapped

Table E.2: Calibration of wet-bulb in-house hygrometer.

	Relative humidity value (%)					
Hygrometer description	Pnt1	Pnt2	Pnt3	Pnt4	Pnt5	Pnt6
Manufacturer-calibrated	5	13	33	45	70	100
In-house Wet-bulb	7.5	15	30	55	75	100

around a thermocouple tip and dipped in the water pool for continuous wetting. We use the former hygrometer to calibrate the latter. Because of the absence of an environmental chamber where relative humidity can be controlled precisely, we made use of ambient relative humidity at different days as calibration points. Initially, dry air was opened inside a fume hood to obtain around a zero relative humidity. Then, a slightly heated water pool ($\sim 30^oC$) inside a closed chamber was allowed to stay for 10 minutes to measure a saturated air point. For relative humidities in between the two extremes, we perform the calibration over several days for different relative humidity values. In Table E.2, we summarize our experimental values. The accuracy of measuring the relative humidity with the wet bulb thermometer was very low at lower relative humidity values. However, for high relative humidity values ($> 70\%$), the uncertainty was below 10%. It is worth mentioning that the relative humidity of the humidified air exiting the humidifier tank was estimated using a second method. The humidified air was directed through a tube and issued into the ambience. By bringing the cooling surface closer to the exit of the tube and cooling it down until a BF spot appears, the dew point of the humidified air was inferred. This method was considered a better estimate by comparing it with the hygrometer reading mentioned earlier.

E.2 Uncertainty Analysis

Bias (systematic) uncertainties are due to calibration of the used sensor. These uncertainties were adjusted by calibrating the sensors systematically. Precision (random) uncertainties are due to scatter in experimental data which are reported with each data shown. In this work, the accuracy of the environmental and surface temperatures was $\pm$ 1 ^{o}C. The relative uncertainty of the pressure gauge measurement was $\pm$ 2% as indicated by the manufacturer. The relative accuracy of the flow rate measurement was $\pm$ 1 % as indicated by the manufacturer. The dimensions of the condensation surface, the standoff distance between the jet exit and surface, and the tube outer diameter were measured with a caliper of an accuracy of $\pm$ 0.1 mm. The inner tube diameter was supplied by the manufacturer with a tolerance of 0.001 in. The temporal measurements were extracted out of the frame rate of the camera with an uncertainty of $\pm$ 1 ms at 1000 fps. The uncertainty of measuring the contact angle was around $\pm$ 0.1^o according to the manufacturer. For the current work, uncertainty propagation in experimental measurements was adopted from the work of Kline and McClintock [222], Moffat (1988) [223] and others. In the following section, we highlight the analysis followed in determining the uncertainty in each experimental chapters.

E.2.1 Uncertainty analysis of Chapter 4

The uncertainty in calculating the standoff-to-diameter ratio is given as follows.

$$\frac{\delta(H/D)}{H/D} = \sqrt{\left(\frac{\delta H}{H}\right)^2 + \left(\frac{\delta D}{D}\right)^2} \tag{E.1}$$

The uncertainty in determining the jet mean velocity at the exit of the tube is calculated as follows.

$$v_j = \frac{4\dot{V}}{\pi D^2} \rightarrow \frac{\delta v_j}{v_j} = \sqrt{\left(\frac{\delta \dot{V}}{\dot{V}}\right)^2 + 4\left(\frac{\delta D}{D}\right)^2} \tag{E.2}$$

where $\dot{V}$ is the volumetric flow rate, and D is the tube inner diameter. The uncertainty of the jet mean velocity at the tube exit is less than 3.2%. Similarly, the uncertainty in calculating the jet Reynolds number is founds as follows.

$$Re_j = \frac{4\dot{V}}{\pi \nu D} \rightarrow \frac{\delta Re_j}{Re_j} = \sqrt{\left(\frac{\delta \dot{V}}{\dot{V}}\right)^2 + \left(\frac{\delta D}{D}\right)^2 + \left(\frac{\delta \nu}{\nu}\right)^2} \tag{E.3}$$

where the uncertainty in calculating the kinematic viscosity comes from the temperature at which we evaluated the property. The highest uncertainty in calculating the jet Reynolds number is 11.2%.

The uncertainty in measuring the BF spot diameter was due to the images taken by the camera. Even though the images where taken from an inclined position, the extent of the BF spot in the direction normal to the incline does not depend on the angle of inclination. However, due to the focus and resolution of the images taken, the accuracy in the measurements

were around 0.1 mm.

The uncertainty in determining the surface, ambient and jet vapor mass fraction stems from the uncertainty in determining their corresponding temperature and relative humidities. The general equation for uncertainty propagation is used. However, due to the complex relation shown in Eq.4.1 along with the need to use steam tables to relate temperature to vapor pressure, we utilized EES to calculate the uncertainty value. In general the uncertainty is written as follow.

$$\delta\omega_s = \sqrt{\left(\frac{\partial\omega_s}{\partial P_\infty} \quad \delta P_\infty\right)^2 + \left(\frac{\partial\omega_s}{\partial P_{v,s}} \quad \delta P_{v,s}\right)^2} \tag{E.4}$$

Similar treatment can be shown for the vapor mass fraction at ambient and jet conditions. The dimensionless fractions derived in equations 4.6 and 4.12 has an uncertainties given by the following equation.

$$\delta\left(\frac{\omega_{max} - \omega_\infty}{\omega_j - \omega_\infty}\right) = \sqrt{\left(\frac{\delta\omega_{max} + \delta\omega_\infty}{\omega_{max} + \omega_\infty}\right)^2 + \sqrt{\left(\frac{\delta\omega_j + \delta\omega_\infty}{\omega_j - \omega_\infty}\right)^2}} \tag{E.5}$$

E.2.2 Uncertainty analysis of Chapter 5

The size of droplets was obtained, as outlined earlier, with the help of the microscopic images. The accuracy, given the set resolution and image focus was around 2 pixels which translates to around 8.4 μm.

The uncertainty in calculating the standoff-to-diameter ratio given as

follows.

$$\frac{\delta(H/D)}{H/D} = \sqrt{\left(\frac{\delta H}{H}\right)^2 + \left(\frac{\delta D}{D}\right)^2} \tag{E.6}$$

The uncertainty in determining the jet mean velocity at the exit of the tube is calculated as follows.

$$v_j = \frac{4\dot{V}}{\pi D^2} \rightarrow \frac{\delta v_j}{v_j} = \sqrt{\left(\frac{\delta \dot{V}}{\dot{V}}\right)^2 + 4\left(\frac{\delta D}{D}\right)^2} \tag{E.7}$$

where $\dot{V}$ is the volumetric flow rate, and D is the tube inner diameter. The uncertainty of the jet mean velocity at the tube exit is less than 3.2%. Similarly, the uncertainty in calculating the jet Reynolds number is founds as follows.

$$Re_j = \frac{4\dot{V}}{\pi \nu D} \rightarrow \frac{\delta Re_j}{Re_j} = \sqrt{\left(\frac{\delta \dot{V}}{\dot{V}}\right)^2 + \left(\frac{\delta D}{D}\right)^2 + \left(\frac{\delta \nu}{\nu}\right)^2} \tag{E.8}$$

where the uncertainty in calculating the kinematic viscosity comes from the temperature at which we evaluated the property. The highest uncertainty in calculating the jet Reynolds number is 11.2%.

The uncertainty in calculating the mass of a single droplet is given as follows.

$$\frac{\delta m_d}{m_d} = \sqrt{\left(\frac{3\sin^3\theta_A}{(2+\cos\theta_A)(1-\cos\theta_A)^2}\delta\theta_A\right)^2 + 9\left(\frac{\delta D}{D}\right)^2 + \left(\frac{\delta \rho_l}{\rho_l}\right)^2} \tag{E.9}$$

The uncertainty in calculating the mass transfer coefficient using Eq.5.3 is

given as follows.

$$\frac{\delta h_m}{h_m} = \sqrt{\left(\frac{\delta \omega_j}{\omega_j}\right)^2 + \left(\frac{\delta \omega_s}{\omega_s}\right)^2 + \left(\frac{\delta A}{A}\right)^2 + \left(\frac{\delta(\Delta t)}{\Delta t}\right)^2 + \left(\frac{\delta m_d}{m_d}\right)^2} \quad \text{(E.10)}$$

BIBLIOGRAPHY

[1] Van P Carey. *Liquid vapor phase change phenomena: an introduction to the thermophysics of vaporization and condensation processes in heat transfer equipment*. CRC Press, 2008.

[2] M J E H Muitjens. Homogeneous condensation in a vapour/gas mixture at high pressures in an expansion cloud chamber. *Technische Universiteit Eindhoven*, 1996.

[3] Wilhelm Nusselt. Die oberflachenkondensation des wasserdamphes. *VDI-Zs*, 60:541, 1916.

[4] Vijay Dhir and John Lienhard. Laminar film condensation on plane and axisymmetric bodies in nonuniform gravity. *Journal of Heat Transfer*, 93(1):97–100, 1971.

[5] Theodore L Bergman, Frank P Incropera, David P DeWitt, and Adrienne S Lavine. *Fundamentals of heat and mass transfer*. John Wiley & Sons, 2011.

[6] Nenad Miljkovic, Daniel J Preston, and Evelyn N Wang. Recent developments in altered wettability for enhancing condensation. In *Encyclopedia of Two-Phase Heat Transfer and Flow II: Special Topics and Applications*, pages 85–131. World Scientific, 2016.

[7] Elaheh Alizadeh-Birjandi, Ali Alshehri, and H Pirouz Kavehpour. Condensation on surfaces with biphilic topography: Experiment and modeling. *Frontiers in Mechanical Engineering*, 5:38, 2019.

[8] Sunwoo Kim and Kwang J Kim. Dropwise condensation modeling suitable for superhydrophobic surfaces. *Journal of heat transfer*, 133(8), 2011.

[9] John W Rose. Personal reflections on fifty years of condensation heat transfer research. *Journal of Enhanced Heat Transfer*, 22(2), 2015.

[10] Robert J Charlson, John H Seinfeld, Athanasios Nenes, Markku Kulmala, Ari Laaksonen, and M Cristina Facchini. Reshaping the theory of cloud formation. *Science*, 292(5524):2025–2026, 2001.

[11] Vivi Apriyanti, Willy Adriansyah, Abdurrachim, and Ari Darmawan Pasek. A review of direct contact condensation of steam on water droplets. In *AIP Conference Proceedings*, volume 1984, page 020035. AIP Publishing LLC, jul 2018.

[12] EJ Watson. The radial spread of a liquid jet over a horizontal plane. *Journal of Fluid Mechanics*, 20(3):481–499, 1964.

[13] Holger Martin. Heat and mass transfer between impinging gas jets and solid surfaces. In *Advances in heat transfer*, volume 13, pages 1–60. Elsevier, 1977.

[14] K Jambunathan, E Lai, MA Moss, and BL Button. A review of heat transfer data for single circular jet impingement. *International journal of heat and fluid flow*, 13(2):106–115, 1992.

[15] R Viskanta. Heat transfer to impinging isothermal gas and flame jets. *Experimental thermal and fluid science*, 6(2):111–134, 1993.

[16] John Lienhard. Liquid jet impingement. *Annual Review of Heat Transfer*, 6(6), 1995.

[17] John H Lienhard. Heat transfer by impingement of circular free-surface liquid jets. In *18th National and 7th ISHMT-ASME, Heat and Mass Transfer Conference, Guwahati, India*, 2006.

[18] BW Webb and C-F Ma. Single-phase liquid jet impingement heat transfer. In *Advances in heat transfer*, volume 26, pages 105–217. Elsevier, 1995.

[19] CO Popiel and L Boguslawski. Effect of flow structure on the heat or mass transfer on a flat plate in impinging round jet. In *2nd UK National Conf. on Heat Transfer*, volume 1, pages 663–685. University of Strathclyde UK, 1988.

[20] Jungho Lee and Sang-Joon Lee. The effect of nozzle aspect ratio on stagnation region heat transfer characteristics of elliptic impinging jet. *International journal of heat and mass transfer*, 43(4):555–575, 2000.

[21] Puneet Gulati, Vadiraj Katti, and SV Prabhu. Influence of the shape of the nozzle on local heat transfer distribution between smooth flat

surface and impinging air jet. *International Journal of Thermal Sciences*, 48(3):602–617, 2009.

[22] N Gao, H Sun, and D Ewing. Heat transfer to impinging round jets with triangular tabs. *International Journal of Heat and Mass Transfer*, 46(14):2557–2569, 2003.

[23] J Seyed-Yagoobi. Enhancement of heat and mass transfer with innovative impinging jets. *Drying technology*, 14(5):1173–1196, 1996.

[24] D Lytle and BW Webb. Air jet impingement heat transfer at low nozzle-plate spacings. *International Journal of Heat and Mass Transfer*, 37(12):1687–1697, 1994.

[25] Merwin Sibulkin. Heat transfer near the forward stagnation point of a body revolution. *Journal of the Aeronautical Sciences*, 9:570–571, 1952.

[26] H Schlichting. Boundary layer theory. hcgraw-hill book company. *New York, N. Y*, page 586, 1968.

[27] C Den Ouden and Charles J Hoogendoorn. Local cohvective-heat-transfer coefficients for jets impinging on a plate; experiments using a liquid-crystal technique. In *International Heat Transfer Conference Digital Library*. Begel House Inc., 1974.

[28] BR Hollworth and SI Wilson. Entrainment effects on impingement heat transfer. i measurements of heated jet velocity and temperature distributions, and recovery temperatures on target surface. In *ASME and American Institute of Chemical Engineers, Heat Transfer Conference*, 1983.

[29] BR Hollworth and LR Gero. Entrainment effects on impingement heat transfer: part ii—local heat transfer measurements. 1985.

[30] Richard J Goldstein, AI Behbahani, and K Kieger Heppelmann. Streamwise distribution of the recovery factor and the local heat transfer coefficient to an impinging circular air jet. *International journal of heat and mass transfer*, 29(8):1227–1235, 1986.

[31] Hong-Wei Xiao, Chang-Le Pang, Li-Hong Wang, Jun-Wen Bai, Wen-Xia Yang, and Zhen-Jiang Gao. Drying kinetics and quality of

monukka seedless grapes dried in an air-impingement jet dryer. *Biosystems Engineering*, 105(2):233–240, 2010.

[32] Nattriya Supmoon and Athapol Noomhorm. Influence of combined hot air impingement and infrared drying on drying kinetics and physical properties of potato chips. *Drying Technology*, 31(1):24–31, 2013.

[33] Arnab Sarkar, Nitin Nitin, MV Karwe, and R Paul Singh. Fluid flow and heat transfer in air jet impingement in food processing. *Journal of Food Science*, 69(4):CRH113–CRH122, 2004.

[34] Nicholas D Francis and William J Wepfer. Jet impingement drying of a moist porous solid. *International journal of heat and mass transfer*, 39(9):1911–1923, 1996.

[35] Rossane Mailde Santos, John Wilmer Parra Llanos, Marintho Bastos Quadri, and Ivan Carlos C da Rocha. Study of drying and consumption of natural gas in a textile stenter of direct heating. *Drying technology*, 33(1):37–54, 2015.

[36] Arun S Mujumdar. 15 impingement drying. *Handbook of Industrial Drying*, page 371, 2014.

[37] Suna Polat. Heat and mass transfer in impingement drying. *Drying Technology*, 11(6):1147–1176, 1993.

[38] Lu Qiu, Swapnil Dubey, Fook Hoong Choo, and Fei Duan. Recent developments of jet impingement nucleate boiling. *International Journal of Heat and Mass Transfer*, 89:42–58, 2015.

[39] DH Wolf, FP Incropera, and R Viskanta. Jet impingement boiling. In *Advances in heat transfer*, volume 23, pages 1–132. Elsevier, 1993.

[40] Zhenhua Liu and Yuhao Qiu. Nucleate boiling on the superhydrophilic surface with a small water impingement jet. In *International Heat Transfer Conference 13*. Begel House Inc., 2006.

[41] Yuan-Yang Li, Zhen-Hua Liu, Guo-Shan Wang, and Le Pang. Experimental study on critical heat flux of high-velocity circular jet impingement boiling on the nano-characteristic stagnation zone. *International Journal of Heat and Mass Transfer*, 67:560–568, 2013.

[42] Dong Guo, JJ Wei, and YH Zhang. Enhanced flow boiling heat transfer with jet impingement on micro-pin-finned surfaces. *Applied thermal engineering*, 31(11-12):2042–2051, 2011.

[43] Matthew J Rau and Suresh V Garimella. Local two-phase heat transfer from arrays of confined and submerged impinging jets. *International journal of heat and mass transfer*, 67:487–498, 2013.

[44] NM Dukle and DK Hollingsworth. Liquid crystal images of the transition from jet impingement convection to nucleate boiling part i: Monotonic distribution of the convection coefficient. *Experimental thermal and fluid science*, 12(3):274–287, 1996.

[45] NM Dukle and DK Hollingsworth. Liquid crystal images of the transition from jet impingement convection to nucleate boiling part ii: nonmonotonic distribution of the convection coefficient. *Experimental thermal and fluid science*, 12(3):288–297, 1996.

[46] D Wang, E Yu, and A Przekwas. A computational study of two phase jet impingement cooling of an electronic chip. In *Fifteenth Annual IEEE Semiconductor Thermal Measurement and Management Symposium (Cat. No. 99CH36306)*, pages 10–15. IEEE, 1999.

[47] Sreekant Narumanchi, Andrey Troshko, Desikan Bharathan, and Vahab Hassani. Numerical simulations of nucleate boiling in impinging jets: Applications in power electronics cooling. *International Journal of Heat and Mass Transfer*, 51(1-2):1–12, 2008.

[48] S Abishek, Ramesh Narayanaswamy, and Vinod Narayanan. Effect of heater size and reynolds number on the partitioning of surface heat flux in subcooled jet impingement boiling. *International Journal of Heat and Mass Transfer*, 59:247–261, 2013.

[49] Lu Qiu, Swapnil Dubey, Fook Hoong Choo, and Fei Duan. The jet impingement boiling heat transfer with ad hoc wall thermal boundary conditions. *Applied Thermal Engineering*, 108:456–465, 2016.

[50] W Timm, K Weinzierl, and A Leipertz. Heat transfer in subcooled jet impingement boiling at high wall temperatures. *International journal of heat and mass transfer*, 46(8):1385–1393, 2003.

[51] AMT Omar, MS Hamed, and M Shoukri. Modeling of nucleate boiling heat transfer under an impinging free jet. *International journal of heat and mass transfer*, 52(23-24):5557–5566, 2009.

[52] Chunkyraj Khangembam, Dushyant Singh, Jishnu Handique, and Kuldeep Singh. Experimental and numerical study of air-water mist jet impingement cooling on a cylinder. *International Journal of Heat and Mass Transfer*, 150:119368, 2020.

[53] Jinho Cha, Taejoon Kim, Seungho Lim, Haneol Lee, and Weon Gyu Shin. Experimental study on the condensation and heat transfer of impinging steam jet on the water surface. *Annals of Nuclear Energy*, 133:458–468, 2019.

[54] Seungho Lim, Jinho Cha, Haneol Lee, Taejoon Kim, and Weon Gyu Shin. Understanding the condensation process of turbulent steam jet using the pdpa system. *International Journal of Multiphase Flow*, 98:168–181, 2018.

[55] Jinho Cha, Seungho Lim, Taejoon Kim, and Weon Gyu Shin. The effect of the reynolds number on the velocity and temperature distributions of a turbulent condensing jet. *International Journal of Heat and Fluid Flow*, 67:125–132, 2017.

[56] Ting Wang, J Leo Gaddis, and Xianchang Li. Mist/steam heat transfer of multiple rows of impinging jets. *International Journal of Heat and Mass Transfer*, 48(25-26):5179–5191, 2005.

[57] Scott C Millsap and Bradley P Marks. Condensing-convective boundary conditions in moist air impingement ovens. *Journal of food engineering*, 70(1):101–108, 2005.

[58] X Li, JL Gaddis, and T Wang. Modeling of heat transfer in a mist/steam impinging jet. *J. Heat Transfer*, 123(6):1086–1092, 2001.

[59] X Li, JL Gaddis, and T Wang. Mist/steam heat transfer in confined slot jet impingement. *J. Turbomach.*, 123(1):161–167, 2001.

[60] F Masuda, T Nakatogawa, K Kawanishi, and M Isono. Experimental study on an impingement high-pressure steam jet. *Nuclear Engineering and Design*, 67(2):273–286, 1982.

[61] D Beysens, A Steyer, P Guenoun, D Fritter, and CM Knobler. How does dew form? *Phase Transitions*, 31(1-4):219–246, 1991.

[62] D Beysens and CM Knobler. Growth of breath figures. *Physical review letters*, 57(12):1433, 1986.

[63] Daniela Fritter, Charles M Knobler, and Daniel A Beysens. Experiments and simulation of the growth of droplets on a surface (breath figures). *Physical Review A*, 43(6):2858, 1991.

[64] Daniel Beysens, Daniela Fritter, Didier Roux, Charles M Knobler, and Jean-Louis Viovy. Growth of a droplet pattern (breath figures) on a surface. In *Dynamics of Ordering Processes in Condensed Matter*, pages 403–413. Springer, 1988.

[65] Dae-Yun Ji, Daeho Kim, and Kwon-Yeong Lee. Enhancement of condensation heat transfer in the presence of non-condensable gas using steam jet method. *International Journal of Heat and Mass Transfer*, 130:603–612, 2019.

[66] MK Seely. Irregular fog as a water source for desert dune beetles. *Oecologia*, 42(2):213–227, 1979.

[67] Kevin A Simonin, Louis S Santiago, and Todd E Dawson. Fog interception by sequoia sempervirens (d. don) crowns decouples physiology from soil water deficit. *Plant, Cell & Environment*, 32(7):882–892, 2009.

[68] Seema Jadhav, Pournima Morey, Manisha Karpe, and Vilasrao Kadam. Dip pen nanolithography. *American Journal of PharmTech Research*, 2:148–168, 2012.

[69] Yaping Chen, Shifan Yang, Jiafeng Wu, and Jiahao Zhou. Impact of helical baffle structure on heat transfer performance of vertical condensers. *Applied Thermal Engineering*, 115:9–16, 2017.

[70] Shulei Li, Yiqiang Jiang, Weihua Cai, Qian Li, Haochun Zhang, and Yan Ren. The influence of structural parameters on heat transfer and pressure drop for hydrocarbon mixture refrigerant during condensation in enhanced spiral pipes. *Applied Thermal Engineering*, 2018.

[71] Yajing Zhao, Daniel J Preston, Zhengmao Lu, Lenan Zhang, John Queeney, and Evelyn N Wang. Effects of millimetric geometric features on dropwise condensation under different vapor conditions. *International Journal of Heat and Mass Transfer*, 119:931–938, 2018.

[72] Iman Zeynali Famileh and Javad Abolfazli Esfahani. Experimental investigation of wet flue gas condensation using twisted tape insert. *International Journal of Heat and Mass Transfer*, 108:1466–1480, 2017.

[73] Ravi Datt, Mangal Singh Bhist, Alok Darshan Kotiyal, Rajesh Maithani, and Anil Kumar. Development of new correlations for heat transfer and friction loss of solid ring with combined square wing twisted tape inserts heat exchanger tube. *Experimental Heat Transfer*.

[74] Saman Rashidi, Omid Mahian, and Ehsan Mohseni Languri. Applications of nanofluids in condensing and evaporating systems. *Journal of Thermal Analysis and Calorimetry*, 131(3):2027–2039, 2018.

[75] Daniel Daniel, Max N Mankin, Rebecca A Belisle, Tak-Sing Wong, and Joanna Aizenberg. Lubricant-infused micro/nano-structured surfaces with tunable dynamic omniphobicity at high temperatures. *Applied Physics Letters*, 102(23):231603, 2013.

[76] H Jeremy Cho, Daniel J Preston, Yangying Zhu, and Evelyn N Wang. Nanoengineered materials for liquid–vapour phase-change heat transfer. *Nature Reviews Materials*, 2(2):16092, 2017.

[77] Marieke Ahlers, Alexander Buck-Emden, and Hans-Jörg Bart. Is dropwise condensation feasible? a review on surface modifications for continuous dropwise condensation and a profitability analysis. *Journal of advanced research*, 16:1–13, 2019.

[78] John Aitken. Breath figures. *Proceedings of the Royal Society of Edinburgh*, 20:94–97, 1895.

[79] John Aitken. Breath figures. *Nature*, 90(2258):619, 1913.

[80] Lord Rayleigh. Breath figures. *Nature*, 86(2169):416–417, 1911.

[81] Donald Frederick Othmer. The condensation of steam. *Industrial & Engineering Chemistry*, 21(6):576–583, 1929.

[82] J X Zhang and L Wang. Effect of air on condensation in a non-vacuum gravity heat pipe. *Applied Thermal Engineering*, 114:255–263, 2017.

[83] Efat Chafik. Design of plants for solar desalination using the multistag heating/humidifying technique. *Desalination*, 168:55–71, 2004.

[84] Efat Chafik. A new type of seawater desalination plants using solar energy. *Desalination*, 156(1-3):333–348, 2003.

[85] MM Farid, Sandeep Parekh, JR Selman, and Said Al-Hallaj. Solar desalination with a humidification-dehumidification cycle: mathematical modeling of the unit. *Desalination*, 151(2):153–164, 2003.

[86] James F Klausner, Yi Li, and Renwei Mei. Evaporative heat and mass transfer for the diffusion driven desalination process. *Heat and mass transfer*, 42(6):528, 2006.

[87] B Dawoud, YH Zurigat, B Klitzing, T Aldoss, and G Theodoridis. On the possible techniques to cool the condenser of seawater greenhouses. *Desalination*, 195(1-3):119–140, 2006.

[88] Tao Hu, Abdel Hakim Hassabou, Markus Spinnler, and Wolfgang Polifke. Performance analysis and optimization of direct contact condensation in a pcm fixed bed regenerator. *Desalination*, 280(1-3):232–243, 2011.

[89] O Phillips Agboola and F Egelioglu. An empirical evaluation of an integrated inclined solar water desalination system with spray jets variation. *Desalination and Water Treatment*, 53(11):2875–2881, 2015.

[90] Emily W Tow et al. Experiments and modeling of bubble column dehumidifier performance. *International Journal of Thermal Sciences*, 80:65–75, 2014.

[91] Huicheng Liu and Mostafa H Sharqawy. Experimental performance of bubble column humidifier and dehumidifier under varying pressure. *International Journal of Heat and Mass Transfer*, 93:934–944, 2016.

[92] G Prakash Narayan, Ronan H McGovern, John H Lienhard, and Syed M Zubair. Helium as a carrier gas in humidification dehumidification desalination systems. 2011.

[93] Mousa K Abu Arabi and Kandi Verlkat Reddy. Performance evaluation of desalination processes based on the humidification/dehumidification cycle with different carrier gases. *Desalination*, 156(1-3):281–293, 2003.

[94] EJ Le Fevre and JW Rose. An experimental study of heat transfer by dropwise condensation. *International journal of heat and mass transfer*, 8(8):1117–1133, 1965.

[95] Jian Huang, Junxia Zhang, and Li Wang. Review of vapor condensation heat and mass transfer in the presence of non-condensable gas, 2015.

[96] Mohammad Saraireh, Graham Thorpe, et al. Simulation of heat and mass transfer involving vapor condensation in the presence of non-condensable gases in plane channels. In *ASME/JSME 2011 8th Thermal Engineering Joint Conference*, pages T10026–T10026. American Society of Mechanical Engineers, 2011.

[97] LI Cheng and LI Junming. Laminar forced convection heat and mass transfer of humid air across a vertical plate with condensation. *Chinese Journal of Chemical Engineering*, 19(6):944–954, 2011.

[98] Jun-De Li. Cfd simulation of water vapour condensation in the presence of non-condensable gas in vertical cylindrical condensers. *International journal of heat and mass transfer*, 57(2):708–721, 2013.

[99] A Dehbi, F Janasz, and B Bell. Prediction of steam condensation in the presence of noncondensable gases using a cfd-based approach. *Nuclear Engineering and Design*, 258:199–210, 2013.

[100] A Dehbi. On the adequacy of wall functions to predict condensation rates from steam-noncondensable gas mixtures. *Nuclear Engineering and Design*, 265:25–34, 2013.

[101] Byong Guk Jeon, Do Yun Kim, Chang Wook Shin, and Hee Cheon No. Parametric experiments and cfd analysis on condensation heat transfer performance of externally condensing tubes. *Nuclear Engineering and Design*, 293:447–457, 2015.

[102] Haozhi Bian, Zhongning Sun, Ming Ding, and Nan Zhang. Local phenomena analysis of steam condensation in the presence of air. *Progress in Nuclear Energy*, 101:188–198, 2017.

[103] Maneesh Punetha and Sameer Khandekar. A cfd based modelling approach for predicting steam condensation in the presence of non-condensable gases. *Nuclear Engineering and Design*, 324:280–296, 2017.

[104] Haozhi Bian, Zhongning Sun, Xiang Cheng, Nan Zhang, Zhaoming Meng, and Ming Ding. Cfd evaluations on bundle effects for steam condensation in the presence of air under natural convection conditions. *International Communications in Heat and Mass Transfer*, 98:200–208, 2018.

[105] Wen Fu, Li Zhang, Xiaowei Li, and Xinxin Wu. Numerical investigation of natural convective condensation with noncondensable gases in the reactor containment after severe accidents. *Science and Technology of Nuclear Installations*, 2019, 2019.

[106] Wen Fu, Xiaowei Li, Xinxin Wu, and Michael L Corradini. Numerical investigation of convective condensation with the presence of non-condensable gases in a vertical tube. *Nuclear Engineering and Design*, 297:197–207, 2016.

[107] Dhongik S Yoon, HangJin Jo, and Michael L Corradini. Cfd modeling of filmwise steam condensation with noncondensable gas with modified boundary condition. *International Journal of Heat and Mass Transfer*, 125:485–493, 2018.

[108] Mingjie Li, Wenjing Zhou, Jinjia Wei, and Wenquan Tao. 3d numerical simulation of heat and mass transfer of fin-and-tube heat exchanger under dehumidifying conditions. *International Journal of Heat and Mass Transfer*, 127:597–610, 2018.

[109] Lili Zhang, Guanmin Zhang, Maocheng Tian, Jingzhi Zhang, and Yi Zhang. Modeling of laminar filmwise condensation of methane with nitrogen on an isothermal vertical plate. *International Communications in Heat and Mass Transfer*, 105:10–18, 2019.

[110] Zhan Yin, Yanling Guo, Bengt Sunden, Qiuwang Wang, and Min Zeng. Numerical simulation of laminar film condensation in a horizontal minitube with and without non-condensable gas by the vof method. *Numerical Heat Transfer, Part A: Applications*, 68(9):958–977, 2015.

[111] XM Wu, Tong Li, Qianyu Li, and Fuqiang Chu. Approximate equations for film condensation in the presence of non-condensable gases. *International Communications in Heat and Mass Transfer*, 85:124–130, 2017.

[112] J Niknejad and JW Rose. Interphase matter transfer: an experimental study of condensation of mercury. *Proceedings of the Royal Society of London. A. Mathematical and Physical Sciences*, 378(1774):305–327, 1981.

[113] RB Bird, WE E LIGHTFOOT STEWART, and Transport Phenomena EN. Jhon wiley & sons inc. *New York, USA*, 2002.

[114] Hi Uchida, A Oyama, and Y_ Togo. Evaluation of post-incident cooling systems of light water power reactors. Technical report, Tokyo Univ., 1964.

[115] T Tagami. Interim report on safety assessments and facilities establishment project for june 1965, no. 1. *Japanese Atomic Energy Research Agency*, 1965.

[116] JCY Koh, Ephraim M Sparrow, and JP Hartnett. The two phase boundary layer in laminar film condensation. *International Journal of Heat and Mass Transfer*, 2(1-2):69–82, 1961.

[117] EM Sparrow, WJ Minkowycz, and M Saddy. Forced convection condensation in the presence of noncondensables and interfacial resistance. *International Journal of Heat and Mass Transfer*, 10(12):1829–1845, 1967.

[118] Abdelouahab Dehbi. A generalized correlation for steam condensation rates in the presence of air under turbulent free convection. *International Journal of Heat and Mass Transfer*, 86:1–15, 2015.

[119] E. M. Sparrow and R. Siegel. Transient film condensation. *Journal of Applied Mechanics, TRANS. ASME, Series E*, 81(1):120–121, 1959.

[120] Paul M Chung. Unsteady laminar film condensation on vertical plate. *Journal of Heat Transfer*, 85(1):63–70, 1963.

[121] VK Dhir. Quasi-steady laminar film condensation of steam on copper spheres. *Journal of Heat Transfer*, 97(3):347–351, 1975.

[122] J Reed, F Gerner, and C Tien. Transient condensation of a laminar film onto a vertical plate. In *22nd Thermophysics Conference*, page 1534, 1987.

[123] SDR Wilson. Unsteady and two-dimensional flow of a condensate film. *Journal of Heat Transfer*, 98(2):313–315, 1976.

[124] P Cheng and DK Chui. Transient film condensation on a vertical surface in a porous medium. *International journal of heat and mass transfer*, 27(5):795–798, 1984.

[125] CD Ebinuma and A Nakayama. An exact solution for transient film condensation in a porous medium along a vertical surface with lateral mass flux. *International communications in heat and mass transfer*, 17(1):105–111, 1990.

[126] SA Masoud, MA Al-Nimr, and MK Alkam. Transient film condensation on a vertical plate imbedded in porous medium. *Transport in Porous Media*, 40(3):345–354, 2000.

[127] MI Flik and CL Tien. An approximate analysis for general film condensation transients. *Journal of Heat Transfer*, 111(2):511–517, 1989.

[128] Sheng-An Yang et al. Transient film condensation on a horizontal elliptical tube. *Journal of Physics D: Applied Physics*, 26(5):793, 1993.

[129] JC Mollendorf and T-Y Chu. Transient film condensation on upward-facing horizontal surfaces. *Chemical Engineering Communications*, 3(3):175–188, 1979.

[130] C Trevino and F Mendez. Transient conjugate condensation process on a vertical plate with finite thermal inertia. *International journal of heat and mass transfer*, 39(11):2221–2230, 1996.

[131] R Balasubramaniam and Mohammad M Hasan. Transient condensation of flowing vapor on a flat-plate: A scaling analysis. *International Journal of Heat and Mass Transfer*, 91:793–799, 2015.

[132] Suresh V Garimella and Richard N Christensen. Transient condensation in the presence of noncondensables at a vertical wall. *Nuclear Technology*, 89(3):388–398, 1990.

[133] Daniel Beysens. *Dew water*. River Publishers, 2018.

[134] D Beysens and CM Knobler. Growth of breath figures. *Physical review letters*, 57(12):1433, 1986.

[135] Jean Louis Viovy, Daniel Beysens, and Charles M Knobler. Scaling description for the growth of condensation patterns on surfaces. *Physical Review A*, 37(12):4965, 1988.

[136] TM Rogers, KR Elder, and Rashmi C Desai. Droplet growth and coarsening during heterogeneous vapor condensation. *Physical Review A*, 38(10):5303, 1988.

[137] Daniela Fritter, Charles M Knobler, and Daniel A Beysens. Experiments and simulation of the growth of droplets on a surface (breath figures). *Physical Review A*, 43(6):2858, 1991.

[138] D Beysens, A Steyer, P Guenoun, D Fritter, and CM Knobler. How does dew form? *Phase Transitions*, 31(1-4):219–246, 1991.

[139] A Steyer, P Guenoun, D Beysens, and CM Knobler. Growth of droplets on a substrate by diffusion and coalescence. *Physical Review A*, 44(12):8271, 1991.

[140] M Sokuler, Günter K Auernhammer, CJ Liu, Elmar Bonaccurso, and Hans-Jürgen Butt. Dynamics of condensation and evaporation: Effect of inter-drop spacing. *EPL (Europhysics Letters)*, 89(3):36004, 2010.

[141] Konrad Rykaczewski, John Henry J Scott, Sukumar Rajauria, Jeff Chinn, Amy M Chinn, and Wanda Jones. Three dimensional aspects of droplet coalescence during dropwise condensation on superhydrophobic surfaces. *Soft Matter*, 7(19):8749–8752, 2011.

[142] J Guadarrama-Cetina, RD Narhe, DA Beysens, and W Gonzalez-Vinas. Droplet pattern and condensation gradient around a humidity sink. *Physical Review E*, 89(1):012402, 2014.

[143] Julian E Castillo, Justin A Weibel, and Suresh V Garimella. The effect of relative humidity on dropwise condensation dynamics. *International Journal of Heat and Mass Transfer*, 80:759–766, 2015.

[144] Shreyas Chavan, Hyeongyun Cha, Daniel Orejon, Kashif Nawaz, Nitish Singla, Yip Fun Yeung, Deokgeun Park, Dong Hoon Kang, Yujin Chang, Yasuyuki Takata, et al. Heat transfer through a condensate droplet on hydrophobic and nanostructured superhydrophobic surfaces. *Langmuir*, 32(31):7774–7787, 2016.

[145] LY Shen, GH Tang, Qing Li, and Yu Shi. Hybrid wettability-induced heat transfer enhancement for condensation with noncondensable gas. *Langmuir*, 35(29):9430–9440, 2019.

[146] Lord Rayleigh. Breath figures. *Nature*, 90(2251):436–438, 1912.

[147] Hiroshi Yabu. Fabrication of honeycomb films by the breath figure technique and their applications. *Science and Technology of Advanced Materials*, 19(1):802–822, 2018.

[148] Ali Alshehri, Sahar Andalib, and H. Pirouz Kavehpour. Numerical modeling of vapor condensation over a wide range of non-condensable gas concentrations. *International Journal of Heat and Mass Transfer*, 151:119405, 2020.

[149] Zehui Chang, Hongfei Zheng, Yingjun Yang, Yuehong Su, and Zhanchun Duan. Experimental investigation of a novel multi-effect solar desalination system based on humidification–dehumidification process. *Renewable energy*, 69:253–259, 2014.

[150] A Sadeghpour, Z Zeng, H Ji, N Dehdari Ebrahimi, AL Bertozzi, and YS Ju. Water vapor capturing using an array of traveling liquid beads for desalination and water treatment. *Science advances*, 5(4):eaav7662, 2019.

[151] Dae-Yun Ji, Jeong-Won Lee, Daeho Kim, Woonbong Hwang, and Kwon-Yeong Lee. Effective reduction of non-condensable gas effects on condensation heat transfer: Surface modification and steam jet injection. *Applied Thermal Engineering*, page 115264, 2020.

[152] R Byron Bird, Warren E Stewart, and Edwin N Lightfoot. *Transport phenomena*. John Wiley & Sons, 2006.

[153] NT Obot, WJM Douglas, and Arun S Mujumdar. Effect of semi-confinement on impingement heat transfer. In *International Heat Transfer Conference Digital Library*. Begel House Inc., 1982.

[154] Abramovich GN. The theory of turbulent jets, 1963.

[155] Howard D Goodfellow. *Industrial ventilation design guidebook*. Elsevier, 2001.

[156] Devansh Singh and Jeffrey J Doom. Simulations of impinging jets with a range of configuration. In *55th AIAA Aerospace Sciences Meeting*, page 0751, 2017.

[157] FLUENT User's Guide. Fluent inc. *Lebanon, NH*, 3766, 2006.

[158] H Reichardt. Gesetzmäßigkeiten der freien turbulenz. vdi-forsch. *Heft414*, 2, 1942.

[159] H Reichardt. Impuls-und wärmeaustausch in freier turbulenz. *ZAMM-Journal of Applied Mathematics and Mechanics/Zeitschrift für Angewandte Mathematik und Mechanik*, 24(5-6):268–272, 1944.

[160] GN Abramovich, TA Girshovich, S Iu Krasheninnikov, AN Sekundov, and IP Smirnova. The theory of turbulent jets. *Moscow Izdatel Nauka*, 1984.

[161] ERG Eckert and RM Drake. Analysis of heat and mass transfer, mcgraw-hill, new york, 1972.

[162] William H Dorrance. *Viscous Hypersonic Flow: Theory of Reacting and Hypersonic Boundary Layers*. Courier Dover Publications, 2017.

[163] M. B. Glauert. The wall jet. *Journal of Fluid Mechanics*, 1(6):625–643, 1956.

[164] Michael Poreh, YG Tsuei, and Jack E Cermak. Investigation of a turbulent radial wall jet. 1967.

[165] Ildiko Horváth, John Hunt, Peter J Barnes, et al. Exhaled breath condensate: methodological recommendations and unresolved questions. *European Respiratory Journal*, 26(3):523–548, 2005.

[166] John Hunt. Exhaled breath condensate: an overview. *Immunology and allergy clinics of North America*, 27(4):587–596, 2007.

[167] Ryan Enright, Nenad Miljkovic, Jorge L Alvarado, Kwang Kim, and John W Rose. Dropwise condensation on micro-and nanostructured surfaces. *Nanoscale and Microscale Thermophysical Engineering*, 18(3):223–250, 2014.

[168] John Graham Wilson. *The principles of cloud-chamber technique*. Cambridge University Press, 2014.

[169] Aijuan Zhang, Hua Bai, and Lei Li. Breath figure: a nature-inspired preparation method for ordered porous films. *Chemical reviews*, 115(18):9801–9868, 2015.

[170] David M Warsinger, Karan H Mistry, Kishor G Nayar, Hyung Won Chung, and John H Lienhard. Entropy generation of desalination powered by variable temperature waste heat. *Entropy*, 17(11):7530–7566, 2015.

[171] Arjang Shahriari, Patrick Birbarah, Junho Oh, Nenad Miljkovic, and Vaibhav Bahadur. Electric Field–Based Control and Enhancement of Boiling and Condensation, 2017.

[172] Nenad Miljkovic, Daniel J Preston, Ryan Enright, and Evelyn N Wang. Electric-field-enhanced condensation on superhydrophobic nanostructured surfaces. *ACS Nano*, 7(12):11043–11054, 2013.

[173] Jingcheng Ma, Soumyadip Sett, Hyeongyun Cha, Xiao Yan, and Nenad Miljkovic. Recent developments, challenges, and pathways to stable dropwise condensation: A perspective. *Applied Physics Letters*, 116(26):260501, 2020.

[174] JW Rose. Dropwise condensation theory and experiment: a review. *Proceedings of the Institution of Mechanical Engineers, Part A: Journal of Power and Energy*, 216(2):115–128, 2002.

[175] P Dimitrakopoulos and JJL Higdon. On the gravitational displacement of three-dimensional fluid droplets from inclined solid surfaces. *Journal of Fluid Mechanics*, 395:181–209, 1999.

[176] Nenad Miljkovic, Ryan Enright, Youngsuk Nam, Ken Lopez, Nicholas Dou, Jean Sack, and Evelyn N Wang. Jumping-droplet-enhanced condensation on scalable superhydrophobic nanostructured surfaces. *Nano letters*, 13(1):179–187, 2012.

[177] Zhiping Yuan, Zhifeng Hu, Fuqiang Chu, and Xiaomin Wu. Enhanced and guided self-propelled jumping on the superhydrophobic surfaces with macrotexture. *Applied Physics Letters*, 115(16):163701, 2019.

[178] Qi Peng, Xiao Yan, Jiaqi Li, Longnan Li, Hyeongyun Cha, Yi Ding, Chao Dang, Li Jia, and Nenad Miljkovic. Breaking droplet jumping energy conversion limits with superhydrophobic microgrooves. *Langmuir*, 36(32):9510–9522, 2020.

[179] Haibao Hu, Suhe Huang, and Libin Chen. Displacement of liquid droplets on micro-grooved surfaces with air flow. *Experimental thermal and fluid science*, 49:86–93, 2013.

[180] Ilia V Roisman, Antonio Criscione, Cameron Tropea, Deepak Kumar Mandal, and Alidad Amirfazli. Dislodging a sessile drop by a high-reynolds-number shear flow at subfreezing temperatures. *Physical Review E*, 92(2):023007, 2015.

[181] GK Seevaratnam, H Ding, O Michel, JYY Heng, and OK Matar. Laminar flow deformation of a droplet adhering to a wall in a channel. *Chemical engineering science*, 65(16):4523–4534, 2010.

[182] AJB Milne and A Amirfazli. Drop shedding by shear flow for hydrophilic to superhydrophobic surfaces. *Langmuir*, 25(24):14155–14164, 2009.

[183] A Razzaghi, SA Banitabaei, and A Amirfazli. Shedding of multiple sessile droplets by an airflow. *Physics of Fluids*, 30(8):087104, 2018.

[184] Xiao Yan, Feipeng Chen, Chongyan Zhao, Yimeng Qin, Xiong Wang, Kazi Fazle Rabbi, Muhammad Jahidul Hoque, Hanyang Zhao, Jiaqi Li, Tarek Gebrael, et al. Near field condensation. 2020.

[185] Jian Li and Zhiguang Guo. Spontaneous directional transportations of water droplets on surfaces driven by gradient structures. *Nanoscale*, 10(29):13814–13831, 2018.

[186] Clark Graham and Peter Griffith. Drop size distributions and heat transfer in dropwise condensation. *International Journal of Heat and Mass Transfer*, 16(2):337–346, 1973.

[187] Rongfu Wen, Xingdong Zhou, Benli Peng, Zhong Lan, Ronggui Yang, and Xuehu Ma. Falling-droplet-enhanced filmwise condensation in the presence of non-condensable gas. *International Journal of Heat and Mass Transfer*, 140:173–186, 2019.

[188] G Prakash Narayan, Mostafa H Sharqawy, Edward K Summers, John H Lienhard, Syed M Zubair, and Mohamed A Antar. The potential of solar-driven humidification–dehumidification desalination for small-scale decentralized water production. *Renewable and sustainable energy reviews*, 14(4):1187–1201, 2010.

[189] Adewale Giwa, Nawshad Akther, Amna Al Housani, Sabeera Haris, and Shadi Wajih Hasan. Recent advances in humidification dehumidification (hdh) desalination processes: Improved designs and productivity. *Renewable and Sustainable Energy Reviews*, 57:929–944, 2016.

[190] K Srithar and T Rajaseenivasan. Recent fresh water augmentation techniques in solar still and hdh desalination–a review. *Renewable and Sustainable Energy Reviews*, 82:629–644, 2018.

[191] Robert Raben, IA and Commerford, George and Dietert. An investigation of the use of acoustic vibrations to improve heat transfer rates and reduce scaling in distillation units used for saline water conversion. *Available from the National Technical Information Service, Springfield VA 22161 as PB-171 911, Price codes: A 08 in paper copy, A 01 in microfiche. OSW Research and Development Progress Report*, 49, 1961.

[192] Xi Chen, Nicole Doughramaji, Amy Rachel Betz, and Melanie M Derby. Droplet ejection and sliding on a flapping film. *AIP Advances*, 7(3):035014, 2017.

[193] Christopher P Migliaccio. Resonance-induced condensate shedding for high-efficiency heat transfer. *International journal of heat and mass transfer*, 79:720–726, 2014.

[194] Mostafa Moradi, Seyed Farshid Chini, and Mohammad Hassan Rahimian. Vibration-enhanced condensation heat transfer on superhydrophobic surfaces: An experimental study. *AIP Advances*, 10(9):095123, 2020.

[195] HR Velkoff and JH Miller. Condensation of vapor on a vertical plate with a transverse electrostatic field. *Journal of Heat Transfer*, 87(2):197–201, 1965.

[196] Davood Baratian, Ranabir Dey, Harmen Hoek, Dirk Van Den Ende, and Frieder Mugele. Breath figures under electrowetting: electrically controlled evolution of drop condensation patterns. Technical report, 2018.

[197] Ranabir Dey, Jander Gilbers, Davood Baratian, Harmen Hoek, Dirk Van Den Ende, and Frieder Mugele. Controlling shedding characteristics of condensate drops using electrowetting. *Citation: Appl. Phys. Lett*, 113:243703, 2018.

[198] B. Traipattanakul, C.Y. Tso, and Christopher Y.H. Chao. Electrostatic-induced coalescing-jumping droplets on nanostructured superhydrophobic surfaces. *International Journal of Heat and Mass Transfer*, 128:550–561, jan 2019.

[199] Hany A Mohamed. Effect of rotation and surface roughness on heat transfer rate to flow through vertical cylinders in steam condensation process. 2006.

[200] SW Peng. Theoretical analysis of laminar film condensation in a rotating cylinder with a scraper. *Heat and mass transfer*, 34(4):279–285, 1998.

[201] S Yanniotis and D Kolokotsa. Experimental study of water vapour condensation on a rotating disc. *International communications in heat and mass transfer*, 23(5):721–729, 1996.

[202] Tommi Huhtamäki, Xuelin Tian, Juuso T Korhonen, and Robin HA Ras. Surface-wetting characterization using contact-angle measurements. *Nature protocols*, 13(7):1521–1538, 2018.

[203] Martin Sievers and John H Lienhard. Design of flat-plate dehumidifiers for humidification–dehumidification desalination systems. *Heat transfer engineering*, 34(7):543–561, 2013.

[204] EJ Le Fevre and John W Rose. A theory of heat transfer by dropwise condensation. In *International Heat Transfer Conference Digital Library*. Begel House Inc., 1966.

[205] CGL Furmidge. Studies at phase interfaces. i. the sliding of liquid drops on solid surfaces and a theory for spray retention. *Journal of colloid science*, 17(4):309–324, 1962.

[206] CW Extrand and AN Gent. Retention of liquid drops by solid surfaces. *Journal of Colloid and Interface Science*, 138(2):431–442, 1990.

[207] AI ElSherbini and AM Jacobi. Retention forces and contact angles for critical liquid drops on non-horizontal surfaces. *Journal of colloid and interface science*, 299(2):841–849, 2006.

[208] Nan Gao, Florian Geyer, Dominik W Pilat, Sanghyuk Wooh, Doris Vollmer, Hans-Jürgen Butt, and Rüdiger Berger. How drops start sliding over solid surfaces. *Nature Physics*, 14(2):191–196, 2018.

[209] Rafael Tadmor, Prashant Bahadur, Aisha Leh, Hartmann E N'guessan, Rajiv Jaini, and Lan Dang. Measurement of lateral adhesion forces at the interface between a liquid drop and a substrate. *Physical review letters*, 103(26):266101, 2009.

[210] Rafael Tadmor. Approaches in wetting phenomena. *Soft Matter*, 7(5):1577–1580, 2011.

[211] EB Dussan et al. On the ability of drops or bubbles to stick to non-horizontal surfaces of solids. part 2. small drops or bubbles having contact angles of arbitrary size. *J. Fluid Mech*, 151(1):20, 1985.

[212] EB DUSSAN V. On the ability of drops to stick to surfaces of solids. iii: The influences of the motion of the surrounding fluid on dislodging drops. *Journal of Fluid Mechanics*, 174:381–397, 1987.

[213] Nenad Miljkovic, Daniel J. Preston, Ryan Enright, and Evelyn N. Wang. Jumping-droplet electrostatic energy harvesting. *Applied Physics Letters*, 105(1):013111, jul 2014.

[214] William M Deen. *Analysis of transport phenomena*, volume 2. Oxford university press New York, 1998.

[215] JW Rose. Further aspects of dropwise condensation theory. *International Journal of Heat and Mass Transfer*, 19(12):1363–1370, 1976.

[216] Basant Singh Sikarwar, Sameer Khandekar, and K Muralidhar. Mathematical modelling of dropwise condensation on textured surfaces. *Sadhana*, 38(6):1135–1171, 2013.

[217] Xiuliang Liu and Ping Cheng. Dropwise condensation theory revisited part ii. droplet nucleation density and condensation heat flux. *International Journal of Heat and Mass Transfer*, 83:842–849, 2015.

[218] Hai Wu Wen and Ru Maa Jer. On the heat transfer in dropwise condensation. *The chemical engineering journal*, 12(3):225–231, 1976.

[219] JW Rose and LR Glicksman. Dropwise condensation—the distribution of drop sizes. *International Journal of Heat and Mass Transfer*, 16(2):411–425, 1973.

[220] Mousa Abu-Orabi. Modeling of heat transfer in dropwise condensation. *International journal of heat and mass transfer*, 41(1):81–87, 1998.

[221] John Lienhard. Liquid jet impingement. *Annual Review of Heat Transfer*, 6(6), 1995.

[222] SJ Kline and FA McClintock. Analysis of uncertainty in single-sample experiments. *Mechanical Engineering*, 75(3), 1953.

[223] Robert J Moffat. Describing the uncertainties in experimental results. *Experimental thermal and fluid science*, 1(1):3–17, 1988.